KAUNAS UNIVERSITY OF TECHNOLOGY

DAINIUS VIRGANAVIČIUS

FABRICATION AND EVALUATION OF TWO DIMENSIONAL REGULAR NANOSTRUCTURES

Doctoral dissertation
Technological Sciences, Materials Engineering (08T)

2017, Kaunas

This doctoral dissertation was prepared at Kaunas University of Technology, Institute of Materials Science during the period of 2012–2017. The studies were supported by the Research Council of Lithuania.

Scientific Supervisor:

Prof. dr. habil. Sigitas TAMULEVIČIUS (Kaunas University of Technology, Technological Sciences, Materials Engineering, 08T).

Doctoral dissertation has been published at:
http://ktu.edu

Editor:

Armandas Rumšas (Publishing House “Technologija”)

ISBN 978-609-02-1401-5

The bibliographical information of this issue is available at Martynas Mazvydas National Library of Lithuania National Bibliographic Database (NBD)

KAUNO TECHNOLOGIJOS UNIVERSITETAS

DAINIUS VIRGANAVIČIUS

TVARKIŲ DVIMAČIŲ NANOMETRINIŲ MATMENŲ STRUKTŪRŲ FORMAVIMAS IR TYRIMAI

Daktaro disertacija
Technologijos mokslai, medžiagų inžinerija (08T)

2017, Kaunas

Disertacija rengta 2012–2017 metais Kauno technologijos universiteto Medžiagų mokslo institute. Mokslinius tyrimus rėmė Lietuvos mokslo taryba.

Mokslinis vadovas:

Prof. habil. dr. Sigitas TAMULEVIVIČIUS (Kauno technologijos universitetas, technologijos mokslai, medžiagų inžinerija – 08T).

Interneto svetainės, kurioje skelbiama disertacija, adresas:
http://ktu.edu

Redagavo:

Armandas Rumšas (Leidykla “Technologija”)

ISBN 978-609-02-1401-5

Leidinio bibliografinė informacija pateikiama Lietuvos nacionalinės Martyno Mažvydo bibliotekos Nacionalinės bibliografijos duomenų banke (NBDB)

List of Abbreviations

AFM – Atomic Force Microscope
bcc – Body Centered Cubic
CAPA – Capillary-force Assisted Particle Assembly
CS – Colloidal Solution
CVD – Chemical Vapor Deposition
DLC – Diamond Like Carbon
DLC:Ag – Diamond Like Carbon Silver Nanocomposite
EBL – Electron Beam Lithography
EDS – Energy Dispersive X-ray Spectroscopy
fcc – Face Centered Cubic
FTIR – Furrier Transform Infrared Spectroscopy
FWHM – Full Width at Half Maximum
GMR – Guided Mode Resonance
hcp – Hexagonal Close Packing
IC – Integrated Circuit
ICP – Inductively Coupled Plasma
IPA – Isopropanol
LIL – Laser Interference Lithography
MBE – Molecular Beam Epitaxy
MEMS – Microelectromechanical Systems
NIL – Nanoimprint Lithography
NP – Nanoparticle
PDMS – Polydimethylsiloxane
PGMEA – propylene-glycol-methyl-ether acetate
PMMA – Poly-methyl-methacrylate
PTFE – polytetrafluorethylene
PVD – Physical Vapor Deposition
PS – Polystyrene
QD – Quantum Dot
RCWA – Rigorous Coupled Waves Analysis
RF – Radio Frequency
RIE – Reactive Ion Etching
RUI – Refractive Index Unit
SEM – Scanning Electron Microscopy
SERS – Surface-Enhanced Raman Scattering
SL – Soft Lithography
SPR – Surface Plasmon Resonance
T-NIL – Thermal Nanoimprint Lithography
TE – Transverse Electric
TM – Transverse Magnetic
UV – Ultra Violet
UV-NIL – Ultra Violet Light Assisted Nanoimprint Lithography
XPS – X-ray Photoelectron Spectroscopy

Table of Contents

1. INTRODUCTION

There's Plenty of Room at the Bottom was the title of the speech that renowned physicist Richard P. Feynman delivered to the American Physical Society back in 1959 [1]. In that speech, he shared his vision for design and engineering at the miniscule scale. The ideas he put forward at the time were truly remarkable and visionary. Among other things, he foresaw the use of focused electron beam for writing massive amounts of information in very small areas, the fabrication of large-scale integrated circuits, and the revolutionary effects that the use of such circuits would have on computing, machines for sequencing and repairing genes by reading DNA molecules as well as the use of mechanical machines for making other machines with increasing precision [2]. All of this took place years before the word 'chip' became part of the lexicon. Although pristine ideas regarding miniaturization of things had been around for a while, Feynman was among the first who realized the enormous potential which can be unleashed if the bizarre properties of matter and phenomena that are only manifested at the atomic and molecular scale would be harnessed and put to use. Therefore, he urged to take action.

The semiconductor industry was the first to follow this path towards miniaturization. Downscaling driven by technical advances allowed more and more transistors to be packed on chips of the same size thus allowing computer chips of 2017 to have several billion of them compared to the several thousand of the initial chips of the early 1970s [3]. This rapid increase in the computing power fuelled the information technology revolution which by some measures nowadays accounts for up to a third of the world's economic output [4]. The trend that was started by the semiconductor industry is now spreading into many other areas of science and technology. The ability to control structure of matter at the nano (10^{-9} m) scale provides possibilities to engineer materials with tailored behavior and properties. This achievement has profound implications in a wide array of areas ranging from medicine to textile and thus could potentially impact economy and society to an even greater extent than the information technology development has done.

The unique properties of nanomaterials for the most part appear only in well-ordered arrangements of submicron and nanodimensional objects, and are based upon their collective response (e.g. surface superhydrophobicity) or stem from coupling between regularly spaced entities (e.g. plasmon resonance). Therefore, the realization of functional devices that can take advantage of those features requires placement and integration of such objects on the surface with a precise control of the shape, size and position. Hence, all the developments making practical use of all that 'room at the bottom' rely on the feasible methods that allow different materials to be structured at the precision of submicron and nanodimensional features. This can be achieved either by sculpting macroscopic entities until the desired dimensions have been reached (the top-down approach), or by assembly of nanoobjects into orderly compositions due to their own interactions or the influence of an external force (the bottom-up approach).

The work presented in this dissertation aims to explore and advance such combined fabrication strategies in two distinct areas: structuring nanocomposite thin films and the formation of particle arrays. In particular, *diamond-like carbon* (DLC)

thin films are of interest in this work. DLC is an amorphous material composed of randomly ordered sp^3 and sp^2 hybridized carbon atoms with some properties that are similar to those of diamond. Although much less hyped than other carbon allotropies, e.g., graphene or carbon nanotubes, DLC possesses an amazing set of properties including: outstanding hardness, optical transparence, chemical inertness which, combined with deposition-ability at the room temperature, makes them extremely attractive as a structural material for a variety of applications. In particular, well-defined diamond-like micro- and nanostructures are of interest for such applications as: stamps in nanoimprint lithography [5], hard X-ray [6] or infrared optics [7] as well as label-free optical sensing [8]. In addition, DLC films can be doped with metals, e.g., silver, forming nanocomposites with metal nanoparticles embedded in the carbon matrix. Metal-doped DLC films possess interesting optical [9], electrical [10], magnetic [11], antimicrobial [12] and tribological [13] properties which are filler size and distribution dependent. Therefore, effective post-processing with the ability to tailor the filler content after film deposition is of high practical interest.

Despite the great potential of such materials, their patterning is challenging and usually depends on complex processing involving multilayer masks [14] and elaborate etching schemes [15–18]; it relies on costly low throughput patterning [19] or has very limited feasibility [20]. In this work, novel strategies based on nanoimprint lithography, imprintable hard masks and plasma techniques enabling straightforward, high throughput patterning of both DLC and DLC films doped with silver (DLC:Ag) are developed. The feasibility of developed patterning process is evaluated by the fabrication of DLC-based subwavelength diffraction gratings which exhibit *guided mode resonance* (GMR) and can be utilized as optical refractive index sensors. Plasma-based processing of DLC:Ag films is carried out with the intention to reveal embedded silver distribution in the carbon matrix and to impose control on the amount and the size distribution of silver particles on the surface.

Surface structuring pursued by top-down strategies alone is not always capable to produce structural quality, shape accuracy, position control and functionality which is required for highly sophisticated applications. In contrast, bottom-up production based on colloidal synthesis methods offers tremendous capabilities and enables to produce a variety of nanoparticles that are different in size, shape and composition [21]. A major advantage of using bottom-up strategies produced colloidal particles instead of top-down fabricated counterparts is their crystalline nature and smooth surface. This is very important for applications e.g., plasmonics. The near absence of crystal defects reduces electron scattering and minimizes the additional damping of the plasmon oscillation. This can result in higher field enhancements compared to lithographically fabricated structures which are typically polycrystalline or amorphous [22]. Moreover, colloidal particles can be easily functionalized by doping with, e.g., fluorescent dye or by the attachment of functional molecules on a surface. Therefore, it is rather tempting to use such particles as nanoscale building blocks. However, for all practical purposes, they have to be integrated on the surface in arbitrarily distributed arrangements with accurate spatial placement over large areas. Among various strategies, the assembly of colloids via dewetting on a topographically structured template mediated by capillary forces seems to be particularly suitable for

this task. Capillary assembly combines the advantages of both approaches and can provide precise topological definition together with tailored shape and functionalization control. One area in particular where such particle arrays could be employed is enchased security features for document protection. Fluorescent particles dyed with different colors can form unique and unclonable color patterns created by the local distribution of different particles within the orderly compositions. Controllable particle deposition requires dedicated equipment which can guide the assembly process. Therefore, this study aims to develop a custom particle deposition setup and evaluate its performance with the intent to explore the possibilities of applying such particle arrays as a security feature.

The Aim of the Doctoral Dissertation

The aim of the dissertation is the development of novel production methods of ordered regular nanostructures with tailored properties which can be utilized for optical sensing and security applications. The aim includes processing and patterning of diamond like carbon (DLC) and diamond like carbon nanocomposite films doped with silver nanoparticles (DLC:Ag), as well as the development of capillary force assisted particle deposition setup and the assessment of the assembly process.

In pursuit to achieve the set goal, the following tasks have been outlined:

The Tasks of the Doctoral Dissertation

1. To develop a DLC patterning process based on lithographic techniques and plasma processing capable of patterning DLC films in an effective and highly reproducible way with the feature resolution of several hundred nanometers and below.
2. To evaluate the feasibility of the developed process by fabricating DLC based refractive index sensor chips that could be fitted into the custom measurement setup where their performance in terms of sensitivity and usability could be assessed.
3. To examine the composition and properties of DLC:Ag nanocomposite films deposited at different conditions and to investigate the effects of plasma processing on their surface morphology and composition.
4. To design and construct a custom capillary force assisted particle deposition setup capable of assembling micro- and nanodimensional particles dispersed in colloidal solution into predefined positions on structured templates which could also be capable to provide a high degree of the assembly process control together with the ability to directly observe and record the course of the procedure.
5. To assess the capillary assisted particle assembly process in terms of template properties and process driving parameters (the temperature of colloidal solution as well as the deposition velocity).

Scientific Novelty and Practical Value of the Doctoral Dissertation

1. A novel and original patterning method for DLC coatings was developed. The method is based on the use of imprintable hard mask and on the shaping

imposed by the thermal nanoimprint lithography in combination with plasma etching which cumulatively enable efficient high quality pattern transfer into DLC with moderate aspect ratios.

2. Highly sensitive DLC-based refractive index sensor chips whose operation is based on the guided mode resonance effect were fabricated. Sensitivity improvement of up to 450% was observed compared to the recently reported results obtained by other authors/producers of sensors based on similar material(s) but fabricated by employing different means.
3. The effective use of plasma processing with the objective to selectively etch a carbon matrix of DLC:Ag nanocomposite films thus providing possibility to control the silver content and the particle size distribution on the film surface was demonstrated.
4. Custom laser interference lithography and capillary-force assisted particle deposition setups were designed, constructed and tested. These tools provide a necessary technical framework needed to pursue research in the field of colloidal particles manipulation, in which, the first steps were taken during the course of these doctoral studies thus laying down the foundation upon which future work will be based. As part of the instrumental base, these tools will support future developments in many different areas of scientific inquiry, such as optical sensors, plasmonics, enhanced optical security elements, Raman and pump-probe spectroscopy, etc.
5. The initial stage of the capillary-force assisted particle deposition process in the transition from low yield to high yield deposition regimes was investigated. The relationship between the spatial distribution of particles in the transition zone and the ambient conditions was evaluated and quantified.
6. Assembly of particles of different sizes (which may as well be attributed with different functionalities) in a non-mixing fashion, i.e., where particles of different sizes settle in separate locations on a template that has only one type of trapping sites was demonstrated by exploiting sequential deposition at different yield regimes.

Author's Contribution

The results presented in this thesis where obtained during the course of doctoral studies at Kaunas University of Technology, Institute of Materials Science, during the years 2012–2017. A part of the investigation, namely, the development of the DLC patterning process, the fabrication of the optical sensor chip and the master stamps for capillary-force assisted particle deposition experiments, was carried out at Paul Scherrer Institute (PSI) in Switzerland. These results were obtained as a part of the author's 12-month fellowship taking place from September 2014 to October 2015. The fellowship was realized in the framework of the project "Nanotop – Sensor with Surface Topography in DLC" (project No. 13,193) and funded by the Scientific Exchange Programme between Switzerland and new member states of the European Union (Sciex-NMS^{ch}).

The author planned the experiments, evaluated them and prepared for their

implementation under the guidance of scientific supervisor, Prof. Sigitas Tamulevičius. During the fellowship at PSI, the guidance was provided by dr. Helmut Schift. Mostly, the execution of technological processes, analytical measurements, analysis and interpretation of the obtained data was independently performed by the author. However, many sophisticated processing and analytical techniques were required to produce the results of this work, and, naturally, one man cannot execute them all in a proficient manner. The technical and scientific staff from KTU and PSI greatly contributed to the execution of the research. Vitoldas Kopustinskas and dr. Andrius Vasiliauskas assisted in the deposition of DLC and DLC:Ag films on the grounds of the strategy developed by the author. Vitoldas Kopustinskas also assisted with *plasma chemical etching* (PCE) of DLC:Ag films. Dr. Asta Tamulevičienė performed *Fourier transform infrared spectroscopy* (FTIR) and *atomic force microscopy* (AFM) measurements. Dr. Robert Kirchner from PSI fabricated silicon masters by e-beam lithography which were used for pattern transfer by thermal NIL and casting. Konrad Vogelsang from PSI helped with his substantial technical knowledge and hands-on experience. Lukas Stankevičius contributed to the optical response simulations of the DLC gratings. Mindaugas Juodėnas helped to conduct particle deposition experiments. Dr. Tomas Tamulevičius and dr. Victor J. Cadarso helped with their insights and advice. Therefore, the author would like to express sincere gratitude to all the people who contributed to and guided in the search of the correct path throughout this endeavor.

Some custom and highly sophisticated pieces of equipment, namely, the interference lithography setup based on Lloyd's mirror geometry and the capillary-force assisted particle assembly setup ware constructed during the course of the doctoral studies. The author was highly involved in these developments. He helped to prepare the technical specifications and the design, and also did the assembly and construction of the custom pieces of this equipment.

The publications which have the author of this thesis listed as the first (main) author to a large extent were prepared by the author himself. Other publications featured significant input in the form of the implemented technological processes, measurements or calculations, and assistance in writing specific chapters.

Statements of the Doctoral Thesis

1. Silicon containing thermoplastic resist SiPol can be used as an effective imprintable hard mask to pattern DLC films by the thermal NIL process in combination with plasma etching. SiPol can serve as an efficient hard mask for etching DLC coatings ensuring 1:4 selectivity for non-doped and 1:2.5 for silver-doped DLC coatings.
2. Adhesion issues arising during pattern transfer when SiPol is directly applied on DLC can be successfully addressed by using incomplete filling of stamp cavities in combination with low imprint temperature. This approach not only allows a virtually zero residual layer imprint but also facilitates the original SiPol process involving organic transfer layer by removing intermediate etchings and resulting in the minimal number of processing steps.

3. The fabricated GMR optical sensors based on DLC gratings show optical response which is in high agreement with simulations of ideally rectangular gratings and has high sensitivity of 319 nm/RIU to refractive index changes in the analyte.
4. The processing of DLC:Ag nanocomposite films by selective plasma etching of carbon matrix reveals embedded silver filer size distribution and allows to modify surface morphology. Films with the higher silver content (>5%) processed under plasma demonstrate pronounced coarsening of the silver filler induced by Ostwald ripening and coalescence.
5. Capillary-force assisted deposition of particles of different sizes in the non-mixing fashion on a template having only one type of traps can be realized by sequential deposition at different yield regimes.

Approbation of the Research Results

The original scientific findings of this thesis were published in 4 papers, mainly in high impact factor scientific journals, and presented in 14 international conferences including 2 oral presentations and 12 poster presentations.

The Structure and Extent of the Dissertation

The dissertation text consists of five major chapters: Introduction, Literature Review, Methods and Experimental Procedures, Results, and Conclusions. The Introduction provides information regarding the motivation, the aim and the goals of this work. The Literature review gives general understanding about the underlying principles, materials and techniques involved in the thesis research and also outlines the progress and challenges in the field of interest. The Methodology part lists and contains a brief description of the processing and analytical techniques that were used in this work. Detailed information about the originally designed and constructed custom tools is also provided in this chapter. The results summarize information about all the experiments and achievements of the thesis research. The Conclusions chapter states the main findings of this investigation. Beside the main chapters, the complementary content such as the list of abbreviations, the list of contents, the list of references, the list of publications and the résumé of the author are also part of this thesis.

The full extent of dissertation is 120 pages of text including 47 figures, 7 tables and 204 entries in the list of references.

2. LITERATURE REVIEW

2.1 Size Effects on the Properties of Materials

Many of the most exciting developments across a number of different fields of the contemporary science and technology over the last several decades have been driven by the exploration and exploitation of materials at the nanometer (10^{-9}m) length scale. Accordingly, a wide range of such activities is encapsulated in the name 'nanotechnology'. Nanotechnology attracts a significant amount of ever-growing interest from the scientific community as well as the general public and continues to develop at an astounding rate in many different directions thus promising dazzling multitude of real-life applications. Apparently, small things can make a big difference. So, we may wonder what actually is different about the nanoscale and why it is gaining such a wide importance.

The term itself was coined by Norio Taniguchi back in 1974 and was used in the context of describing the dimensional accuracy of the *integrated circuit* (IC) fabrication processes approaching the 100 nm mark [23]. Nowadays, according to the broadly accepted standard (ISO/TS 80004-2:2015) set by the community involved, nanotechnology refers to the manipulation and exploitation of matter on an atomic and molecular scale and deals with materials having structural features between 1 and 100 nanometers in at least in one dimension [24]. Often, however, the coarser objects of submicron dimensions (100–1000 nm) are also considered under the same domain. Dimensionality plays an important role and, therefore, nanomaterials are often classified according to the number of dimensions in which they are constrained. Zero-dimensional (0-D) nanomaterials have nanometer-scale dimensions in every direction (e.g. nanoparticles, fullerenes); one-dimensional (1-D) nanomaterials have nanometer-scale dimensions in two directions (e.g., nanowires, nanotubes); two-dimensional (2-D) nanomaterials have nanometer-scale size only in the thickness direction (e.g., thin films), while nanoporous or nanostructured materials belong to three-dimensional (3-D) nanomaterials [25].

The interest in structuring and engineering materials at the given size threshold has more than pure logistic advantage of denser packing, e.g., more transistors per given area. The main reason why nanomaterials attract so much attention is because they exhibit uniquely different physical, chemical and mechanical properties compared to their bulk counterparts. Moreover, these properties are size-dependent, making it possible to engineer the material properties not only by defining the chemical composition but also by tailoring the size, the shape and the way in which individual building blocks are assembled. The origin of the unique size-dependent properties of nanomaterials can be attributed to the two fundamental effects that become significantly important at the nanoscale: *scaling* and *spatial confinement* [26]. Scaling refers to the increase of the fraction of surface atoms with the decreasing size of the enclosed object. In the case of a sphere, the surface area scales with the square of its radius, while the volume scales with the cube of the radius. As such, the surface/volume ratio is inversely proportional to the radius and becomes significantly large in nanoscale dimensions. Consequently, the fraction of atoms located at the surface of a spherical nanoparticle (NP) gets larger as its size decreases. Such scaling

is demonstrated in Fig.2.1 for spherical gold NPs.

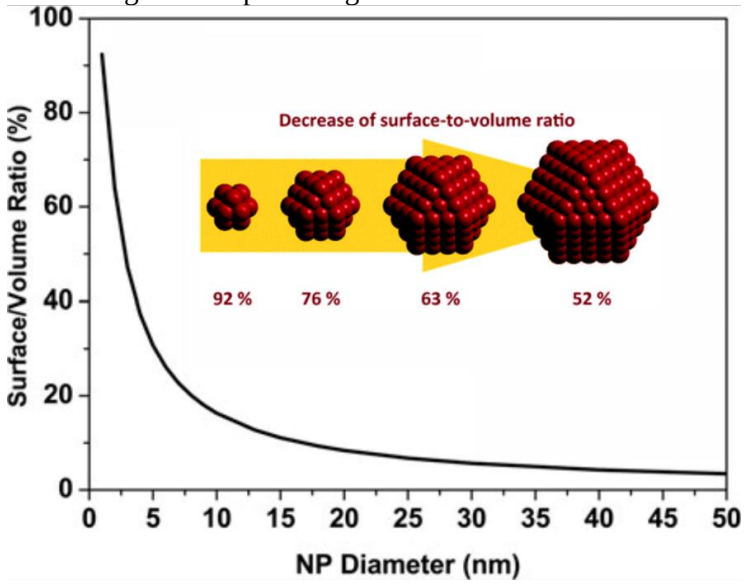

Figure 2.1. Size dependence of the surface to volume ratio for spherical gold nanoparticles. The graphical inset depicts three-dimensional representations of NPs with different surface/volume ratios. Adapted from [22].

The increase in the surface/volume ratio has a dramatic impact on several properties since surface atoms differ from those residing in the interior of the particle. Surface atoms have fewer neighbors and thus possess unsatisfied chemical bonds. As a result, they have a higher free energy, higher reactivity and increased mobility. As the size of NPs gradually decreases, the contribution of the surface atoms to the total free energy and the properties of the NP progressively increases. The larger surface contribution also causes changes in the length and the angle of interatomic bonds, which not only affects the mechanical, chemical, and thermal properties but may also lead to the structural rearrangement [22].

If we take gold as an example, it, from being chemically inert in the bulk state, becomes a highly efficient catalyst and can easily disperse in solvents at nanoscale dimensions [27]. The melting point of gold also decreases as the particle size gets smaller. Below 50 nm, the decrease becomes noticeable, even reaching values as low as 600 K for NPs smaller than 3 nm [28]. That is significantly lower when compared to the melting point of 1337 K in the bulk state.

When considering nanocrystalline or nanocomposite materials, their properties can significantly differ from the materials composed of coarser (>1μm) grains due to the same reasons. As grains get reduced to nanoscale dimensions, the number of atoms residing at the grain boundaries becomes comparable with the number of atoms residing in the grains. Such a significant increase in the volume fraction of grain boundaries, interfaces and defect density alters many mechanical and chemical properties of nanomaterials. For instance, the grain boundaries act as barriers to the dislocation motion and therefore result in the increased hardness as well as the tensile

and compressive strength of the material. The nanocrystalline copper (d = 6 nm) has five times greater hardness than that of copper in the bulk state. The thermal conductivity in nanostructured materials is significantly reduced due to the strong interactions and enhanced scattering of thermal energy transporting phonons at grain boundaries. Grain boundaries also provide much easier diffusion paths compared to bulk lattice thus resulting in a higher diffusion coefficient. This enhances the kinetics of certain reactions and can be beneficial for well-adherent and dense oxide layer formation or hydrogen sorption in metal hydrides [29].

The limited dimensions of nanoscale objects also lead to spatial confinement effects. Spatial confinement effects derive from the quantum mechanical nature of matter which is not noticeable in macroscopic objects. However, as the size of material dimensions decreases below a certain critical limit, the wave function of the charge enclosed in the nanodimensional object gets confined to a limited number of states. The larger the number of confined dimensions is, the higher the number of the discrete states is as well. This results in significant changes of several electrical and optical properties. The critical length scale is not the same for different physical properties and different materials as it depends both on the property under consideration and on the exact nature of the chemical bonds in the material. For example, the confinement effects on the magnetic properties (e.g., superparamagnetic behavior) will only occur if the NP dimensions are comparable to or smaller than the size of a single magnetic domain (20–100 nm, depending on the material) [30]. The spatial confinement effects on the optical properties are prominently evident in the case of NPs made of semiconducting materials e.g., CdSe. The relevant length scale in this case is the *exciton Bohr radius*. The exciton Bohr radius is the average distance between the electron in the conduction band and the hole it leaves behind in the valence band which ranges from ~2 to ~50 nm depending on the material [22]. When the size of the semiconductor NPs becomes smaller than the exciton Bohr radius, confinement begins to affect the exciton wave function leading to the quantization of the energy levels according to the *Pauli exclusion principle* (see Fig. 2.2). Generally, as the size of the NPs decreases, the difference in energy between the highest valence band and the lowest conduction band increases. More energy is then needed to excite a particle, and more energy is also released when the particle returns to its ground state. As a result, the optoelectronic properties of semiconductor NPs become strongly size- and shape-dependent, making it possible to tune the photoluminescence within a wide spectral window. The discrete, quantized energy levels of such NPs relate them more closely to atoms than to bulk materials and therefore are often referred as *quantum dots* (QD). Quantum dots are particularly significant for optical applications owing to their bright, pure colors along with their high efficiencies, longer lifetimes and a high extinction coefficient [31]. Their application examples include optical amplifiers [32], single photon sources [32], light emitting devices [33], biomedical imaging [34] and photovoltaics [35].

Optical excitations in metals do not create excitons but, instead, induce collective oscillation of the free conduction band electrons (see Fig. 2.3). Such charge density oscillation is referred as *surface plasmon resonance* (SPR). The tight confinement of resonances in the metallic NPs enables them to support very strong

electromagnetic fields. The relevant length scale to observe the spatial confinement effects on the optical properties of metallic NPs is the electron mean free path which is ~50 nm in gold [28]. Plasmon resonance appears as very strong absorption and scattering for a particular wavelength; in fact, metallic NPs are among the most strongly scattering solid state objects when the scattering strength is normalized to the object's geometric cross section.

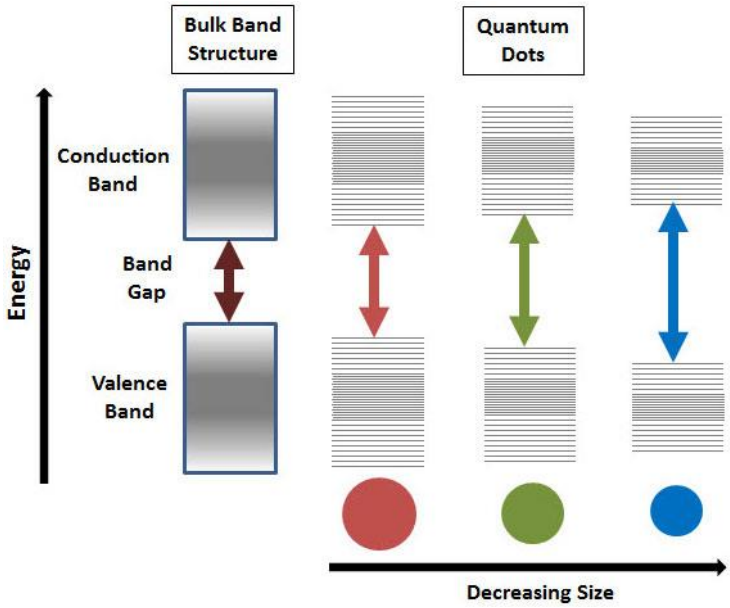

Figure 2.2. Splitting of energy levels in quantum dots due to the quantum confinement effect; semiconductor band gap increases with the decrease in the size of the nanocrystal. Adapted from [31].

The wavelength of resonance in metal nanostructures is primarily determined by the plasma frequency of the metal and the dielectric constant which in metals is strongly negative. It is also highly dependent on both the size and the shape of the NP. When dimensional symmetry is broken, a particle gains additional modes of plasmon resonance. For resonance to occur in visible or near infrared wavelengths, the plasma frequency of the metal has to be in the blue/UV part of the spectrum, and the damping has to be low. The first condition is met by most metals, whereas the second condition is only met by a few e.g., gold, silver, copper and aluminum. The frequency of the plasmon resonance is not only sensitive to the morphology and the composition of the particle but also to the refractive index of its local environment. This is because the evanescent electric field of the plasmon extends beyond the surface of the particle and penetrates the medium in its immediate vicinity. When plasmonic NPs are brought together within distances of well below the resonance wavelength, the plasmon resonances of the individual building blocks couple to form collective plasmon modes. Therefore, combining them into clusters or lattices in a controlled manner provides further benefits such as the possibility to control the wavelength, the linewidth and the field strength of collective plasmon resonances by modifying the

morphology [22]. All these features make plasmonic NPs extremely useful for a variety of applications ranging from sensing [36] and microscopy [37] to the enhancement of photophysical processes such as fluorescence [38] and Raman scattering [39].

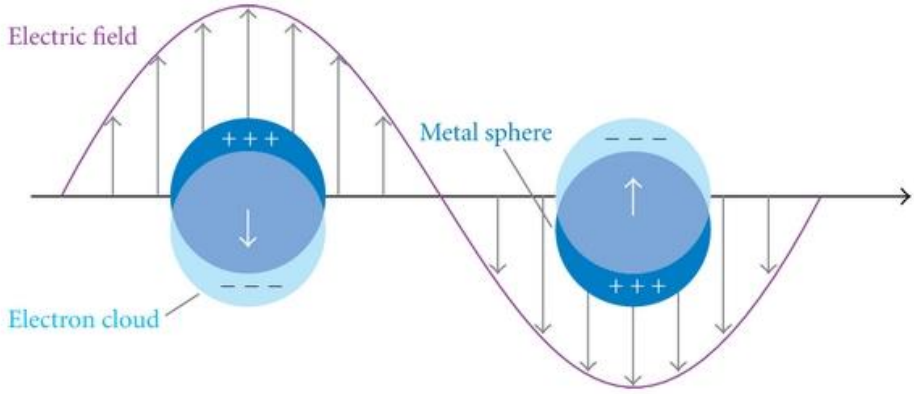

Figure 2.3. Graphical illustration of localized surface plasmon resonance resulting from the collective oscillations of delocalized electrons in response to an external electric field [40].

2.2 Top-Down Fabrication

Fabrication of submicron and nanoscale objects is a challenging and often costly procedure. In most cases, the goal is to manufacture them at low cost, with a good yield, by using the simplest and most efficient technology possible. Therefore, a wide variety of methods can be used to make nanomaterials. All of them can be classified into two broad categories: *top-down* methods and *bottom-up* methods [41]. The top-down fabrication approach starts with macroscopic materials (e.g., silicon wafer) which are then carved and modified in a specific way to produce nanoscale-sized entities.

Mechanical high energy ball milling is one of the simplest ways of making NPs of metals (e.g., Co, Cr, W) and alloys (e.g., Al-Fe, Ag-Fe) in the form of powder. During this process, hardened steel or tungsten carbide balls are put into a container along with bulky grains or flakes of the material of interest. The closed container is rotated at high speed (a few hundred of rpm) around its axis. Collisions of heavy milling balls pulverize the initial material. The larger balls tend to produce smaller-sized grains but result in larger defects in the particles. By controlling the speed of rotation of the container as well as the duration of milling, it is possible to ground the material to a fine powder of particles (ranging from a few nm to a few tens of nm in diameter) whose size can be fairly uniform [42]. The method is efficient and can deliver a large amount of material in a short period of time. However, ball milling can only be used to produce basic nano-size objects in the form of powder. More complex structures require much more sophisticated methods. Lithography in combination with etching is a process of choice when it comes to micro- or nanofabrication. It enables to selectively remove parts of a thin film or a substrate in a controllable and

highly reproducible manner. There is a great variety of lithographic techniques which utilize different shaping approaches, each possessing its own advantages and drawbacks. Therefore, the method to be used is highly dependent on the specific situation requirements.

Photolithography is by far the most established process employed to generate patterns of submicron and nanoscale features. It uses light (typically in the UV range) to transfer a geometric pattern from a photomask to a light-sensitive polymeric material (photoresist) covering the substrate. The process starts by spin-coating the thin layer of photoresist on the substrate surface. The thickness of the spin-coated film depends upon the spinning speed and the viscosity of the resist and may vary anywhere from less than one hundred nanometers to several microns. Afterwards, the resist is soft-baked in order to remove solvents. Lastly, after the mask and the substrate have been aligned, the photoresist is exposed to the light projected through the mask. The exposure leads to chemical changes, which alters solubility of the photoresist. The exposed/unexposed area of the photoresist film then can be removed via development in a suitable solvent thus leaving a positive/negative-tone resist pattern on the substrate. The patterns engraved in the photoresist can then be used as an etch protecting layer in the subsequent fabrication process. Resolution is one of the most important parameters used to describe the performance of a lithography system. It is defined as the line-width of the smallest feature that can be produced. In the optical exposure system, it is limited by the light diffraction. The formula for resolution (R) is as follows [43]:

$$R = k\lambda/NA \tag{2.1}$$

where k is the coefficient that encapsulates process-related factors, with a typical range between 0.3 and 0.6, λ represents the wavelength of the exposure radiation, and *NA* stands for the numerical aperture of the lens.

From the above equation, it is obvious that a decrease in λ will improve the resolution capability of the lithography system as well as increasing NA of the projection lens. Improvements of such nature have driven advancements of the IC manufacturing process for the last 50 years. Such adaptations as high numerical aperture optics and immersion lenses, deep UV excimer laser sources, phase shifting masks, optical proximity correction and double patterning approaches have pushed the conventional optical lithography well into the nanoscale [44]. However, it gets increasingly hard to follow the fast phase of development in line with Moore's law, which, based upon historical observations, claims that the number of transistors per given area doubles approximately every 18 months [3]. Due to the exposure wavelength diffraction limit and the technical complexity, the manufacturing costs have been increasing dramatically for the nanoscale line-width manufacturing. Currently, the most advanced form of photolithography employed at the industrial scale is 193-nm immersion lithography, in which, water is used as the immersion medium. When the lens–wafer space is immersed in water, the NA effectively increases 1.44 times according to the refractive index of water at 193-nm wavelength. That, in addition to restricted design rules, enabled to achieve higher resolutions. This

technology is currently being used for 22- and 14-nm nodes [45].

Due to the expensive lithography tools and the continuous feature size miniaturization to the deep submicron length scales, the current lithography tools are barely able to meet the industrial and academic needs. Additionally, for non-microelectronic applications that cannot tolerate the high cost or do not find the need for the high volume and high planarity production, other lithography techniques are required. Several alternative technologies are currently being developed to complement or replace the conventional photolithography. These include *extreme ultraviolet* (EUV) lithography, X-ray lithography, *electron beam lithography* (EBL), focused ion beam lithography, nanoimprint lithography, and interference lithography. Extreme ultraviolet lithography uses an extreme ultraviolet wavelength (13.5 nm). It is a promising technology capable to extend to lower dimensions, but faced with many challenges. The difficultly of manufacturing masks and radiation sources, or the lack of reliable photoresists due to the inherently ionizing energy of EUV radiation are only a few noteworthy examples. Even if these issues get solved, the prohibitively high implementation costs of EUV and X-ray lithography will most likely preclude their use in applications other than microelectronics.

Electron beam lithography instead of light uses a focused electron beam which scans the surface covered with electron radiation sensitive resist directly imposing the arbitrary patterning. This technique is capable of achieving high resolutions, yet it is limited by the low throughput which restricts the output and confines to the certain areas of usage. The same is true for the focused ion beam lithography. Interference lithography, although it does not require the mask and can impose simultaneous patterning over large areas, is limited due to its ability to produce only periodic patterns. *Nanoimprint lithography* (NIL) is very promising alternative for low cost and high flexibility nanoscale patterning, however, the contact nature of the process renders alignment and contamination issues which have to be resolved for its broad acceptance [43]. Electron beam and nanoimprint lithography were extensively used in this work and are covered in more detail in sections 3.2 and 3.3.

The pattern generated by lithographic techniques is then transferred to the underlying functional layer or substrate through the etching or lift-off process. Etching can be performed with chemical etchants (e.g., acids, alkalis) or by using dry plasma-based processing. Wet etching is simpler to implement, and can typically offer a higher etch rate; however, since chemical attack is isotropic, or, in case of crystalline materials (e.g., silicon) facet-specific, there is little control over directionality. That may lead to mask undercuts and deviation from the desired profile. As feature dimensions get smaller, mask undercutting becomes intolerable, and the plasma-based etching capable of anisotropic pattern transfer gets to be a more suitable choice. Nowadays, plasma-based pattern transfer has replaced wet chemistry for most applications. The modern plasma etching equipment has evolved along two paths which eventually merged into the current configuration, where the substrate to be etched is placed onto a radio frequency (RF) powered electrode, with or without an additional plasma-generation source [46]. The physical sputtering by energetic ions, chemical attach by reactive species, or the combination of both is employed to achieve a highly directional removal of the exposed material.

2.3 Bottom-Up Fabrication

Bottom-up processes utilize fundamental building blocks (e.g., ions, atoms, molecules) which are assembled into entities of the nanoscale dimensions. Bottom-up assembly can be carried out in numerous ways, yielding a wide variety of different nanomaterials. Different techniques can be put into two broad categories according to the phase through which the process is carried out. These include the vapor phase and the liquid-phase methods. The vapor phase deposition methods include *physical vapor deposition* (PVD) or *chemical vapor deposition* (CVD) which are widely used to fabricate thin films, multilayers or nanoparticles, either freestanding as powders, or embedded into films of another material [47]. PVD methods, which are used to deposit thin layers of material, employ physical causes, such as evaporation, sputtering or ionization, to vaporize solid materials in the vacuum environment. The resulting vapor phase is subsequently deposited onto the substrate through a condensation mechanism. In case there is a stencil employed (e.g., a structured layer of polymeric material), arbitrary patterns can be produced via lift-off process.

CVD methods employ chemical reactions to decompose and deposit gas phase precursors directly on a substrate. The energy needed for decomposition is usually supplied by maintaining the substrate at an elevated temperature. There are many variations of this technique; however, one with significant importance is *Molecular Beam Epitaxy* (MBE). It allows single atomic layers to be grown on top of each other thus yielding thin films whose thickness can be controlled with atomic precision.

Liquid-phase methods make use of chemical precipitation reactions in the solution and can be divided into *Sol-gel* methods and *colloidal* methods.

In the Sol-gel methods, the metal precursors undergo hydrolysis and condensation reactions thus forming colloidal sols which subsequently aggregate into a wet porous network (gel). Upon aging, the gel undergoes a process of densification through which the pores contract and expel the solvent. The gels can then be dried yielding a nanoporous structure (a xerogel or an aerogel) [22].

When it comes to NP production, colloidal methods are by far the most versatile and the most widely used. Typical colloidal synthesis routes that are frequently used to prepare NPs involve the reduction of precursor compounds (e.g., metal salts) in aqueous or organic solvents via chemical, biochemical, photochemical and electrochemical pathways or by thermal decomposition. These techniques depend upon chemical reactions that induce phase transition via nucleation and growth of nanometer-sized particles within a solvent.

Colloidal synthesis methods are cost-efficient, scalable and technologically simple to implement. They can yield a spectacular variety of NP morphologies with a small size disparity, which can be further improved by centrifugation [48] and fractional precipitation [49]. The NPs of various shapes including nanocubes [50], nanorods [51], decahedra [52], icosahedra [52, 53], tetrahedral [53], octahedral [54], pyramids [55], stars [56], etc. can be produced. A variety of different compositions ranging from single compounds (metals, e.g. Au; semiconductors, e.g. CdSe; insulators, e.g. SiO_2) to alloys (e.g., FePt, $Cd_{1-x}Zn_xS$) [31], doped materials (e.g., ZnSe:Mn, NaYF4:Yb,Er) [57, 58] or combinations of two or more different materials joined by one or more interfaces in the same nanoparticle (e.g. a CdSe core

surrounded by a ZnS shell) [31,22] can be produced as well.

The morphology of a particle starts to develop early in the nucleation stage and can be tailored during the growth. Many factors ranging from precursors to reaction conditions can affect its final shape. During nucleation, new phase entities are created from a metastable (supersaturated or supercooled) solution as the growth units (e.g., ions/atoms or molecules) formed by the reduction of precursors randomly assemble into small transitory clusters. These clusters shift their size and shape or may disassemble all together due to the ongoing attachment and separation of additional units. This continues until critical dimensions have been reached, and a stable seed is subsequently formed. The seed can form either in a solution (homogeneous nucleation) or on the surface of solid bodies (heterogeneous nucleation). Since such phase transition requires energy, there is an important distinction between the two. The energy barrier for nucleation is higher in the homogeneous case and requires higher levels of metastability than in the heterogeneous case, where the presence of interfaces facilitates nucleation by reducing the energy barrier through pre-existent nucleation sites.

Under thermodynamic equilibrium conditions, the seed tends to obtain the shape having the smallest surface free-energy for the enclosed volume. In an isotropic surface energy case, such a shape would be the sphere since it features the smallest surface area for a given volume. However, crystalline solids have anisotropic surface energy and, as such, the total surface energy is not only determined by the surface area but also by the nature of the surface facets. Facet-specific surface energies originate from the reduced coordination of the atoms at the surface as compared with those in the bulk [59]. In the *face centered cubic* (fcc) crystal, the atoms in the interior have 12 nearest neighbors, whereas atoms at the surface have eight nearest neighbors on (100), seven on (110), and nine on (111) facets (see Figure 2.4a). Proportionally to the number of the broken bonds, the surface energy of these facets increases as $E111 < E100 < E110$ [60]. Due to the energy disparity between the facets, a polyhedron enclosed with the truncated facets of the lowest possible surface energy happens to be the most efficient equilibrium shape. Although truncation exposes higher energy facets, it also reduces the surface area, which, overall, is beneficial.

During the seed formation via heterogeneous nucleation, the mismatch between lattice parameters of the support and the growing seed may cause a deviation from the equilibrium shape. Usually, if the growing crystalline seed is strained at the interface, it prefers to decrease the interface area, by growing faster in the vertical direction than laterally. The larger aspect ratios are obtained with the larger mismatch. Structural defects (e.g. twining) are also a common cause of shape deviations.

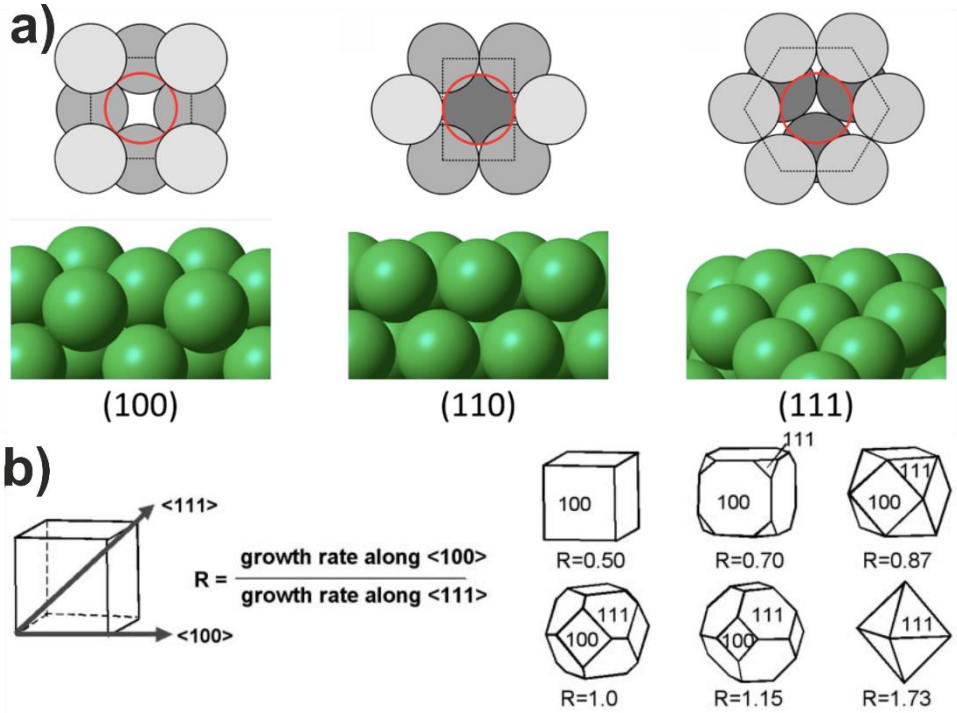

Figure 2.4. a) Graphical illustration depicting the arrangement of surface atoms in the fcc lattice. On (100) facet, each surface atom has 8 closest neighbors, while there are 7 on (110) and 9 on (111). The three-dimensional structure is shown underneath each case. Adapted from [60]. b) A variety of morphologies that can be realized by tuning the ratio of growth between (100) and (111) planes of a cubic crystal. Adapted from [61].

After nucleation, the seeds are added into the growth solution containing the same or different growth units. The growth proceeds via heterogeneous reduction of growth units on the seed's surface. If the growth is executed near the equilibrium conditions, the facets with the lowest surface energies will determine the morphology of the growing particle. Otherwise, the final shape of NPs can be modified by many factors affecting the kinetics of growth. Besides the unique equilibrium shape, several polyhedral growth shapes, including highly anisotropic ones, can be obtained by altering the relative growth rates of the different facets. Additives, such as surfactants, ligands, foreign ions, etc., mixed in the growth solution are capable and are often used to induce shape modifications. For example, the growth of Ag [62] and Au [63] seeds in the presence of a cationic surfactant (e.g., cetyltrimethylammonium bromide) delivers elongated nanorod shapes. Additives, while interacting with the particle's surface, can preferentially adsorb on certain facets and inhibit the incorporation rate of growth units on those facets thus changing the relative growth rates [64]. In such a case, the facets that are growing faster in the perpendicular direction will gradually disappear, while the other facets with the lower perpendicular growth rate will gradually appear as the growth proceeds [21]. Various shapes of a cubic NP obtainable by fine-tuning the ratio (R) between {100} and {111} facet growth rates

are depicted in Figure 2.4b. Alternatively, growth can be carried out inside templating or confining structures which yield supported NPs. This is a common practice to produce nanotubes and vires [65]. After the synthesis, particles are often caped with surface-bound molecules (e.g. ligands, block copolymer or DNA fragments) to stop aggregation and keep them dispersed in the solution.

Colloidal particles of various shapes can self-assemble into superlattices without any external guidance. Superlattices are a long-range ordered composition of individual nanoparticles which are separated by the layers of surface ligands and bonded together through weak forces (e.g., van der Waals) or hard-particle (e.g., excluded volume) interactions. The well-established methods that are used to produce NP superlattices include various evaporation techniques which produce thin film superlattices and destabilization or sedimentation techniques which lead to the formation of three-dimensional superlattices (see Fig. 2.5a–d). The most straightforward way to prepare thin film superlattices is to simply cast a small droplet of dilute NP solution on a solid support and let it dry. As the solvent evaporates, particles precipitate on the interface. When such a procedure is carried out in a tilted vial, the direction of meniscus movement can be controlled. Another approach is to use immiscible liquids. NPs are usually dispersed in nonpolar solvents and can be spread on top of polar liquids thus forming thin monolayer films. Through evaporation or imposed lateral surface pressure (by using the Langmuir−Blodgett setup), ordered NP monolayers can be controllably condensed on a surface.

Destabilization-based assembly is triggered by the quality reduction of the solvent, which provokes coronas of surface ligands capping individual NPs to overlap. Such overlapping between neighboring NPs promotes gradual clustering and precipitation of faceted NP superlattices in the solution. Solvent destabilization can be accomplished either by a controlled diffusion of nonsolvent into the NP solution or by heating a premixed solvent/nonsolvent mixture with the objective to enrich the higher-boiling nonsolvent component [66]. Rapid evaporation or destabilization leads to barrierless aggregation which typically produces disordered, dendritic, or branch-type formations. Therefore, the process has to be carried out gradually in order to achieve ordered NP superlattices.

Another possible approach that can be used to produce superlattices is the crowding-induced self-assembly via gravitational sedimentation of NPs at the bottom of the solvent. The effectiveness of this approach directly depends upon the ratio between the size of the gravitational potential energy and the thermal energy of the particle. The ratio scales favorably with the size and reaches parity at 100−1000 nm levels. As such, the method is only suitable for the assembly of the larger particles [67].

Arrangements in which NPs are ordered inside the superlattice largely depend upon the nature of their intermediate interaction. Two approximations, namely, the hard particle model assuming perfect particle rigidity, and the soft particle model assuming perfect particle elasticity, provide a useful framework in a pursuit to rationalize the most probable configuration.

Hard particles interact solely through excluded volumes and strive to maximize the total entropy of the system. In a supersaturated solution, the dense packing yields

the maximum entropy and, therefore, when forming superlattices, hard particles tend to arrange into the densest possible configuration for a given shape. For spheres, the densest packing is either fcc or *hexagonal close packing* (hcp), both yielding a 74% filling rate of the space [68]. For that reason, the assembly of spherical or nearly spherical (e.g., cuboctahedral, rhombicuboctahedral) NPs mediated by solvent evaporation primarily leads to the formation of fcc or hcp superlattice thin films. Nonspherical polyhedrons, which are often encountered as energy-minimizing equilibrium shapes, settle into different lattice arrangements. For a tetrahedron, the densest known packing is a double dimer (with the filling factor of 86%) making it the most likely arrangement to be assembled [69].

Instead of maximizing the packing density, soft particles seek to minimize the contact area in between them in order to achieve the maximal entropy state [70]. Block copolymer micelles are a typical example of soft particle systems. If hard spheres frequently assemble into fcc and hcp arrangements, block copolymer micelles prefer to adopt the *body-centered cubic* (bcc) ordering which is a poor choice for efficient packing with a density of 68%, but has a smaller internal surface area than almost any other arrangement.

Colloidal NPs composed of a rigid inorganic core and a soft organic corona of surface bond molecules sit in between those two extremes (the idealized hard and soft particles). The ratio between the length of the capping ligand (L) and the radius of the core (R) quantifies NP 'softness' and plays a crucial role in selecting the arrangement habit [60]. For example, 2.2 nm diameter spherical Au NPs caped with octadecanethiol ligands (L/R≈1) yields bcc superlattices (Fig. 2.5b), whereas the same ligands on 4.5 nm diameter spherical Au NPs (L/R≈0.5) yield hcp structures (Fig. 2.5c) [71].

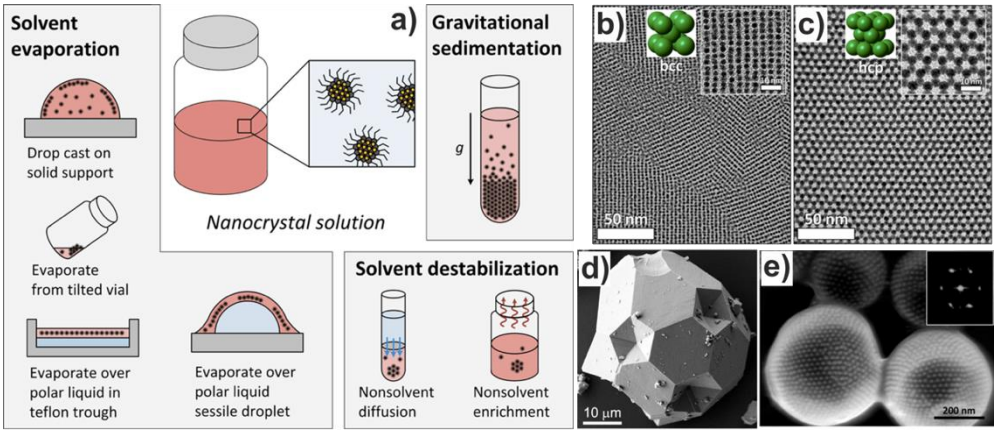

Figure 2.5. a) Established approaches used to prepare ordered NP arrays. Adapted from [60]. b) Au NP (L/R≈1) monolayer adapting bcc ordering. c) Au NP (L/R≈0.5) monolayer adapting hcp ordering. Adapted from [71]. d) three-dimensional superlattice of PbS nanocrystals formed by solvent destabilization. Adapted from [60]. e) Spherical vesicles with walls comprised of close-packed Au NPs with block copolymer ligands. Adapted from [72].

More exotic self-assemblies can be created by capping NPs with block copolymers or DNA fragments. NPs end-grafted with copolymers consisting of hydrophobic−hydrophilic segments can assemble into close-packed arrays which, when exposed to water, tend to bend, forming spherical vesicles with walls comprised of close-packed NPs glued together by hydrophobic segments (see Fig. 2.5e) [72].

Self-assembly is one of the most efficient methods to order a large number of particles on a surface. However, these methods are limited to certain dense packings, and the placement of individual NPs into sparse arrays remains difficult to achieve. Pick-and-place techniques, e.g., optical tweezers or AFM, can offer manipulation at a single particle level; however, they are inefficient.

2.4 Diamond Like Carbon Films

Carbon is the most versatile of all the chemical elements. Owing to its unique electron configuration of four valence band electrons and four vacancies in the outer shell together with three possible hybridization states, namely, sp^3, sp^2 and sp^1, carbon atoms can settle into several arrangements and form a vast number of different compounds. Different hybridizations lead to the formation of certain carbon allotropes ranging from crystalline, e.g., diamond, graphite or fullerenes to several amorphous substances. Amorphous carbon materials can have any mixture of sp^2 (typical for graphite), sp^3 (typical for diamond), and even sp^1 bonds arranged in a random network with no long-range order with some of the dangling bonds being terminated by hydrogen or other dopants (e.g., N, F), which help to stabilize the structure. *Diamond-like carbon* (DLC) is the name attributed to amorphous carbon materials containing a significant fraction of sp^3 type bonds which give the material attractive physical and mechanical properties that are to a certain extent similar to those of natural diamond [73]. Unlike diamond, which forms at high pressure high temperature conditions and is hard to synthesize, DLC films can be deposited at room temperature. That is an important practical advantage enabling to coat almost any vacuum compactible material and providing a much broader spectrum of possible applications. Also, diamond has a faceted structure, whereas DLC films are isotropic with no grain boundaries. The internal structure of DLC (according to the model first proposed by Robertson) consists of a disordered network of small (up to a few nm in size) sp^2 bonded carbon clusters which are randomly dispersed in the sp^3 bonded carbon matrix. The clusters are comprised of mostly six-fold planar ‘aromatic’ rings which are fused together into larger groups [74]. As the sp^3 fraction in the films increases, the sp^2 clusters get smaller and more disordered until they finally change from ring to chain configurations.

DLC is a sort of an umbrella term which is often vaguely used in an attempt to describe a variety of amorphous carbons. This may lead to a confusion since, frequently, films with vastly different properties are called by the same name and vice versa [75]. For example, the hardness of such films can vary in the range of <10–80 GPa. The performance of DLC-like materials depends upon the ratio between sp^3 and sp^2 bonding and on the amount of hydrogen more than on anything else. Based on

that, they can be further subdivided into smaller categories which better reflect on their properties. Those categories are as follows:

1. Hydrogenated amorphous carbon (a-C:H) is the common form of DLC. These films contain a moderate content of sp^3 bonds and an intermediate amount (20–40%) of hydrogen. a-C:H films come in two different forms, the hard a-C:H, and the soft one. The hard a-C:H features a hardness of >10GPa and consists of a lower fraction of sp^3 bonds and a low hydrogen amount, whereas the soft a-C:H is denoted by a higher sp^3/sp^2 fraction but contains a higher hydrogen amount as well. Because of that, most of the sp^3 bonds are H-terminated, and the material is rather soft (<10GPa) and has a low density.
2. Hydrogenated tetrahedral amorphous carbon (ta-C:H) films have a high (70%) sp^3 content and a relatively low (30%) hydrogen content. The hardness of this type of films can reach up to 50 GPa.
3. Hydrogen-free or low H-content form of amorphous carbon (a-C/a-C:H) films exhibit a very low hydrogen content (less than 20%) and a significantly high fraction (>90%) of sp^2 bonds together with sp^2 clustering. Their hardness is as low as ~3 GPa. These films are often referred to as *glassy carbon*.
4. Tetrahedral amorphous carbon (ta-C) contains up to 90% sp^3-hybridized bonds and no hydrogen at all. These films are denoted by the highest hardness reaching up to 80 GPa [75–77].

Figure 2.6 represents various forms of DLC in a ternary phase diagram. The three corners of this diagram are related to diamond, graphite, and hydrocarbons. The only type of DLC coatings that is under consideration in this thesis is of the first type.

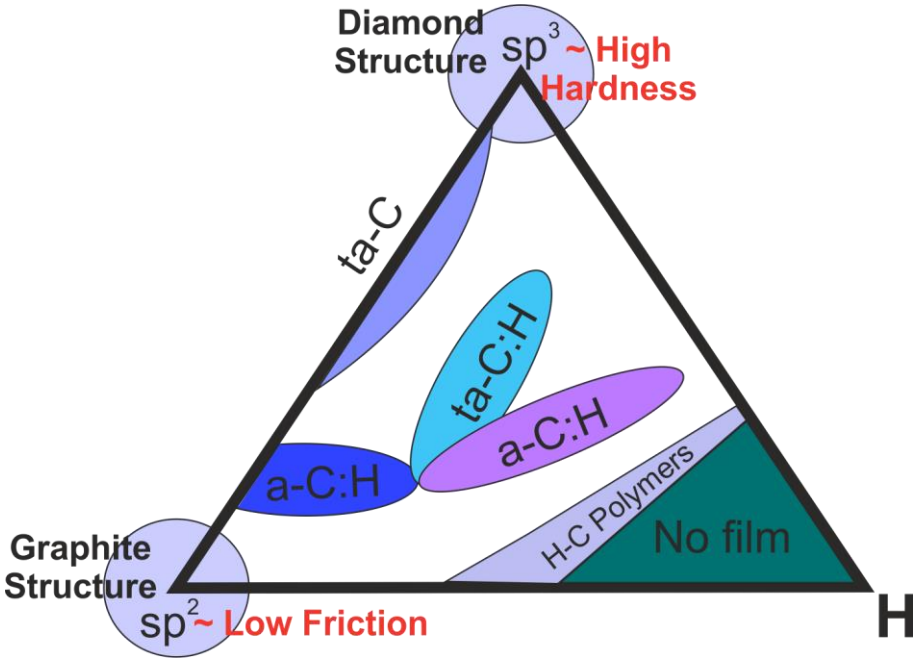

Figure 2.6. Ternary diagram representing various forms of DLC. Adapted from [75].

Aisenberg and Chabot were the first to produce amorphous carbon coatings which showcased diamond-like properties back in the early 1970s sparking the interest in the field [78]. Since then, there has been a considerable amount of interest from both academic and industrial communities as the attractive set of properties associated with DLC films makes them useful for a variety of technological applications ranging from 'data to beer storage' [75].

First and foremost, due to the high hardness (which can reach up to 80GPa), low friction and chemical inertness (resistant to most acids, alkalis and solvents), they are utilized as protective, nonabrasive, and corrosion-resistant coatings. Very thin <5 nm atomically smooth (RMS roughness equaling to 0.2 nm) layers of DLC have been used to protect the magnetic layer of hard disks against corrosion and wear [79]. Other uses include coating razor blades, tools, machinery parts, etc. By being translucent in the IR range and showing only modest absorption in the VIS-NIR part of the spectrum, DLC films can be used for such optical applications as antireflective and scratch-resistant coatings for optical elements [80]. As a biocompatible material, DLC found its use in biomedical applications. DLC coatings deposited on metallic and polymeric biological implants have been used to increase the compatibility with human tissues and ensure the longevity of such components as artificial heart valves, arterial stents or joint implants [81, 82].

DLC films can be fabricated by using many different PVD or CVD techniques from a vast number of carbonaceous precursors enabling efficient production in small-scale laboratory as well as large industrial settings. The key is to ensure intense surface bombardment with medium energy (~100eV) carbon or hydrocarbon ions during the growth of the film. This promotes sp^3 fraction formation and leads to denser

and harder films [76]. Therefore, the optimal techniques would be the ones which can ensure such conditions.

Besides their high hardness, DLC films are also characterized by high internal stress. This is the main drawback which often causes cracking and delamination of the films from the substrate leading to the production of low-quality DLC films with no practical applications. A lot of research has been dedicated in pursuit of coping with this issue. Fruitful strategies include the application of an interlayer between the film and the substrate [83] or the incorporation of additives (e.g., metals) during the growth of the films [84]. Additives help to relax the stress – yet, they also compromise the hardness of the coating. On the other hand, the incorporation of nanometer scale clusters of metals into DLC films is an additional advantage since it further extends their application spectrum. DLC films doped with metal nanoparticles show interesting electrical and optical characteristics due to the localized surface plasmon resonance phenomenon [85]. Silver, gold and copper doped films are particularly interesting because their contrasting matrix and metal dielectric functions and nanoparticle size dependent pronounced plasmonic absorption peak in the visible region of the spectrum. This feature can be exploited in the realization of novel optical sensors, etc.

The high potential of using DLC not only as a surface coating but as a structural material as well is evident. The unique set of properties makes this material an extremely attractive for an increasing number of applications, such as MEMS [86], optical sensors [8, 87], etc. However, there is lack of feasible, high throughput, high resolution patterning strategies capable of structuring such films with patterns approaching the nanoscale resolution. Due to these reasons, the usability of the material is restricted.

2.5 Guided Mode Resonance Based Sensing

Subwavelength gratings showcase anomalous diffraction effects which manifest as sharp, narrow linewidth peaks in a transmitted or reflected light spectrum under certain conditions. Barnabas Wood was the first to observe such behavior; therefore, this phenomenon became known as Wood's anomalies because it could not be explained by the ordinary theory of diffraction. In our times, it is already known that such behavior is caused by the coupling/decoupling of the externally propagating incident light into the modes of the waveguide supported by the waveguide grating structure [88]. Since this phenomenon occurs only at certain resonance conditions, it is referred to as *guided mode resonance* (GMR).

Guided mode resonance gratings are essentially dielectric slab waveguide structures, in which, the waveguide core is in some way periodically modulated by periodic variations in the refractive index, position of the waveguide core, or waveguide core thickness. Guided mode resonance gratings under study in this thesis are of the third type, in which, a high refractive index waveguide core layer (n_2) with periodic surface height modulation of amplitude d, thickness h and period λ is supported by a low-index substrate (n_3) as illustrated in Figure 2.7. The surface of the grating is further exposed to a superstrate medium of refractive index n_1.

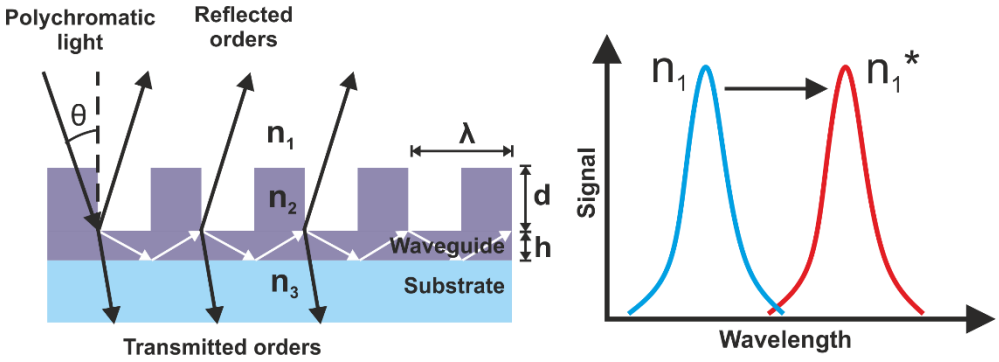

Figure 2.7. Schematic representation of the GMR grating. The change of the refractive index in the vicinity of the grating leads to a change in the resonance wavelength.

Periodic variations of the waveguide structure make them exhibit behavior typical for both diffraction gratings and slab waveguides. As the incident light beam hits the GMR structure surface, it gets reflected into several diffraction orders by the grating. When the wave vector of one diffracted order beam matches that of one guided mode, coupling occurs, and the guided modes get to be excited within the waveguide. The waveguide structure can support only a discrete number of such modes. The coupling condition can be derived from the grating and the propagation in the waveguide equations [89].

$$n_{eff} = n_1 \sin\theta + m\frac{\lambda}{\Lambda} \tag{2.2}$$

where n_{eff} is the effective refractive index of the guided mode, n_1 is the refractive index of the superstrate, θ is the coupling angle, m is the diffraction order, λ is the wavelength, and Λ is the grating period.

However, due to the periodic modulation, as these guided modes propagate, they continually leak out energy into the far-field, and attenuate over distance. For this reason, in the literature, they are often referred to as leaky modes, and GMR gratings are named as leaky waveguides. The light that is decoupled out of the structure interferes with both the transmitted and the reflected light. At a certain resonance wavelength, the decoupled light interferes destructively with the transmitted light and constructively with the reflected light, resulting in highly efficient resonant reflection for a particular wavelength interval.

When the periodicity of the waveguide modulation becomes smaller than the wavelength of the incident light, only the zero-th diffracted orders can propagate with all higher orders being cut off. At such conditions, according to theoretical modeling, the resonance reflection/transmission efficiency could reach up to 100% at resonance; however, in practice, it is limited due to the scattering by structural imperfections and absorption losses.

The wavelength at which guided mode resonance occurs depends on the refractive indices of the materials, of which the GMR grating is composed, as well as on the geometrical configuration, such as period, duty cycle, waveguide layer

thickness, etc. It is also polarization-dependent, which leads to the different resonant conditions for *transverse-electric* (TE) and *transverse-magnetic* (TM) polarized light. This is due to the birefringence in the grating structure which alters the effective refractive indexes for different polarizations. Crossed gratings with the rotational symmetry (e.g., square or hexagonal arrays) are capable of producing a polarization-independent resonance response at a normal incidence. The resonance wavelength of GMR gratings may also be tuned by the angle of incidence of the illumination source. However, when the angle of incidence deviates from zero, the resonance peak becomes split, and the structure exhibits resonant reflection at two separate wavelengths [90]. The width of the resonance peak depends on the rate of de-coupling of the guided mode (i.e. on the photon lifetime), which is mostly determined by the refractive index contrast between the waveguide core and the cladding. The lower refractive index contrast leads to a narrower linewidth of the resonance and vice versa. However, it cannot be broadened extensively as there is a certain limit. The symmetric shape of the resonant peak is attained only if the refractive indexes of the substrate and the superstrate are equal ($n_3=n_1$). Otherwise, asymmetric spectral response is observed [88].

The ability of GMR gratings to support narrow high efficiency and polarization dependent resonant reflection/transmission (which is highly tunable by material selection, geometry definition or the angle of illumination incidence) makes them immensely applicable for a wide range of optical filtering [91] and switching applications [92]. For example, high efficiency angle-tunable color filter capable of producing colors from blue to red by varying angles of incidence ranging from 8º to 35º has been demonstrated. Such a response is achieved by careful engineering of the geometry of the grating so that only one of the split reflected peaks would be able to appear inside the visible wavelength spectrum [92].

Beside filtering, GMR gratings can be employed as label-free sensors since their resonance spectra are highly sensitive to the refractive index changes in the vicinity of the waveguide. GMR grating sensors have been realized by using a variety of different materials ranging from polymers [93] to diamond [94], and in different configurations, such as external cavity laser sensors [65], or broadband illumination setups [93]. The detection is realized by affecting the evanescent tail of the waveguide mode near the interface. When analyte molecules bind to the surface, the effective refractive index of the media surrounding the waveguide is changed. This perturbates the original waveguide mode inducing a shift of the resonance wavelength [89]. Selective detection can be achieved by functionalizing grating surface with appropriate receptors.

GMR based grating sensors have been successfully applied to monitor thin film growth [96, 97], changes in pressure [98], biochemical reactions [8, 87], etc. The sensing distance is determined by the penetration depth of the evanescent field, which, usually, can reach up to several hundred nanometers [99]. The evanescent field corresponds only to a tiny fraction of the total optical power since, typically, >80% of it is contained within the waveguide and does not contribute to the surface attachment sensing. This may impose limitations on the detection sensitivity in some

scenarios. Attempts to increase useful area by employing a porous waveguide have been reported [89].

The ideal sensor would have a high sensitivity defined by the rate, at which the resonance signal shifts with respect to the change in the refractive index and the narrow resonant peak thus enabling a high detection limit by allowing to accurately track the smallest resonance shifts. However, there exists a trade-off relationship between the two, and enhancing one leads to a reduction of the other. Therefore, a different design has to be adapted depending on whether one wants precision or broad range detection. One more area where GMR gratings can be applied is *surface enhanced Raman scattering* (SERS). When the resonant wavelength of the grating is reconciled with the probing wavelength (typically, 532nm), it can serve as a field enhancement substrate. Additionally, if plasmonic particles are closely arranged on such grating, the surface scattering effect can be multiplied thus providing an enhancement of up to ~14 times across the entire grating surface in addition to the SERS effect of Ag NPs alone as reported in [100].

GMR based grating sensors possess many advantages over other competing techniques, e.g., SPR. They can be manufactured cheaply and quickly by using nanoreplication methods, and the structures can be used repeatedly if properly cleaned. They possess high sensitivity, tuneability, versatility and require only very modest equipment. Additionally, they can be fabricated from a variety of different materials to fit the application at hand [90]. DLC is in particular a well-suited material for the fabrication of GMR sensors which operate in the VIS-NIR range. High refractive index, optical translucence, high hardness, and chemical inertness – the properties associated with DLC, enable the development of robust wear and corrosion resistant GMR sensors [101,102].

2.6 Capillary Assisted Particle Deposition

Tremendous advances in colloidal chemistry have enabled the production of a variety of nanoparticles which are different in size, shape and composition [21]. It is rather tempting to use such particles as nanoscale building blocks in order to create functional devices. Their unique properties offer great potential for the development of novel optical [103], electronic [104], MEMS [105] and sensing [106] devices. The manufacturing of such devices often requires placement and integration of nanoparticles on the surface with a precise control of position. It was demonstrated that such control can be achieved by applying an external driving force, e.g., electrostatic [107], optical [108] or capillary [109–111], which impels the localization of particles into predefined arrangements.

Capillary force assisted particle assembly (CAPA) stands out among others as a method offering unmatched efficiency, versatility and scalability. This technique exploits long ranging capillary interactions which are used to overcome the random-in-nature Brownian motion of particles suspended in a colloidal solution and to immobilize them on the template surface via dewetting.

Capillary forces act at the phase boundary between a colloidal suspension, the template, and the surrounding air (a three-phase contact line) across the length of the

droplet meniscus. These forces can be exploited for the assembly of particles. The process outcome is first and foremost defined by the surface tension between the template surface and the colloidal suspension. This can be tailored both through the variation of surfactant concentration in the solution or the surface chemical conditioning (e.g., the application of a fluorinated material monolayer). Assembly mechanism is based on particle confinement at the contact line of a sliding droplet. Such sliding can be induced by solvent loss due to evaporation or by other means. As the contact line of the droplet meniscus slides over a wetting (hydrophilic) surface, it gets pinned due to strong interactions with the surface and the particles suspended at the boundary get trapped. Evaporation induces convective flow of the solvent which carries particles from the bulk towards the contact line thus forcing their aggregation. When the solvent layer gets thin enough, that it becomes comparable to the diameter of the particle, the profile deformation of the droplet meniscus caused by particle protrusion gives rise to the downward-facing capillary forces which, coupled with attractive forces appearing between the particles during drying, lead to the formation of a continuous 2D superlattice (see Fig 2.8a). During such phase transition, the arrangement of particles in the lattice is entropy-driven; therefore, the particles accommodate the dense packing.

As shown by Malaquin *et al*., the assembly rate is determined by the rate of solvent evaporation. The key parameter here is the *dew point* (T_{dew}) which defines the equilibrium state of water vapor saturation in the air and depends upon the ambient temperature and the relative humidity. The assembly temperature (T_a) can be controlled by substrate heating/cooling. At $T_a > T_{dew}$ conditions, the surrounding air is not saturated; therefore, as a droplet evaporates, the convective flow drags particles to the contact line and leads to assembly. The greater disparity between T_a and T_{dew} leads to a higher rate of assembly. At $T_a \sim T_{dew}$, the evaporation of solvent in the drying region is nearly zero; therefore, no particle flux is created, the assembly process is stopped, and only the Brownian motion of particles is observable. At $T_a < T_{dew}$, condensation takes place, creating a reverse flow of solvent which disassembles the already assembled monolayer of particles [109].

When deposition is carried out on a flat nonwetting (hydrophobic) surface, no particles are assembled because the high surface tension prohibits droplet pinning. Although convection still brings particles to a contact line thus forming an enriched layer (the accumulation zone), the small deformations of the meniscus exerted due to crowding are simply not up to scale to provide confinement (see Fig 2.8b). Therefore, the particles are being dragged together with the droplet while it slides over the surface. Particle concentration increases as the solvent evaporates, which, eventually, leads to a rapid assembly into disordered aggregates. However, if there are some topological features, such as pits or raised structures, on the otherwise smooth and nonwetting substrate, they act as traps that can constrain the particles tightly confined in the accumulation zone while they are being dragged by the receding motion of the contact line. Moreover, the contact line of the droplet meniscus gets pinned and deforms as it slides over those obstacles. If, at the moment of pinning, a particle is in the trap, the meniscus deformation will create a capillary-force which will act upon the protruding particle and thus impose the permanent immobilization at those

trapping sites while the contact line recedes (see Fig 2.8c). In such a way, highly ordered particle arrays defined by the template geometry can be assembled.

The capillary-force relates to the amount of protrusion which depends upon the ratio between the trap depth and the particle size as well as upon the surface tension of the droplet meniscus. The strength of the capillary force (F_c) based on the model proposed by Ni *et al*. can be expressed as [112]:

$$F_c = 4\pi\gamma r\left\{1 - \sin\left(\theta + \sin^{-1}\frac{d-r}{r}\right)\right\} \tag{2.3}$$

where γ is the surface tension, d denotes the depth of the trap, r represents the radius of the particle, and θ stands for the contact angle of the droplet. The force is not parallel to the template surface; therefore, it has vertical and horizontal components. The act of the horizontal component can cause the removal of the trapped particle at the recession if the barrier against the removal provided by the trap sides is not sufficient. The trap effectiveness depends upon the ratio between its depth and the cross-section of the particle. Flauraud *et al*. in a recent study demonstrated that the trap's shape and profile can be used to increase trapping efficiency and the accuracy of particle placement. In the receded areas of the template, the trapped particles may be displaced by the evaporation of the residual solvent. The drying of the solvent evokes capillary immersion forces which affect the final relative pose of the particle within the trap. In this case, funneled or v-grove trap geometries can provide an enhanced level of the positioning accuracy [113].

There are several different capillary assembly implementations. In the simplest possible experiment, a drop of a colloidal suspension is left to dry on a topographically patterned template (which is an analogous process to the evaporation induced 2D superlattice formation). As a solvent evaporates, the meniscus of the drop sweeps over and deposits particles into geometric features on the template. In this case, there is only minimal control of the yield and evolution of the deposition process. Therefore, differential evaporation rates across the drop often lead to the formation of coffee ring-like patterns [114]. With a tool that controls colloid temperature and speed of meniscus movement, much more precise assemblies are possible [115]. In particular, particle assembly employing a motorized stage with controllable assembly speed and temperature has several advantages compared to other implementations [116–118] allowing stricter control over deposition parameters, especially when a microfluidic chip providing a flow of controllable concentration of particles is in use [119, 120].

The CAPA technique combines top-down and bottom-up approaches allowing precise placement defined by lithographic techniques with the shape and functionality control of colloidal NPs. Such synergy provides a superior level of control over the particle position, orientation and interparticle distance with a precision down to several nanometers [113].

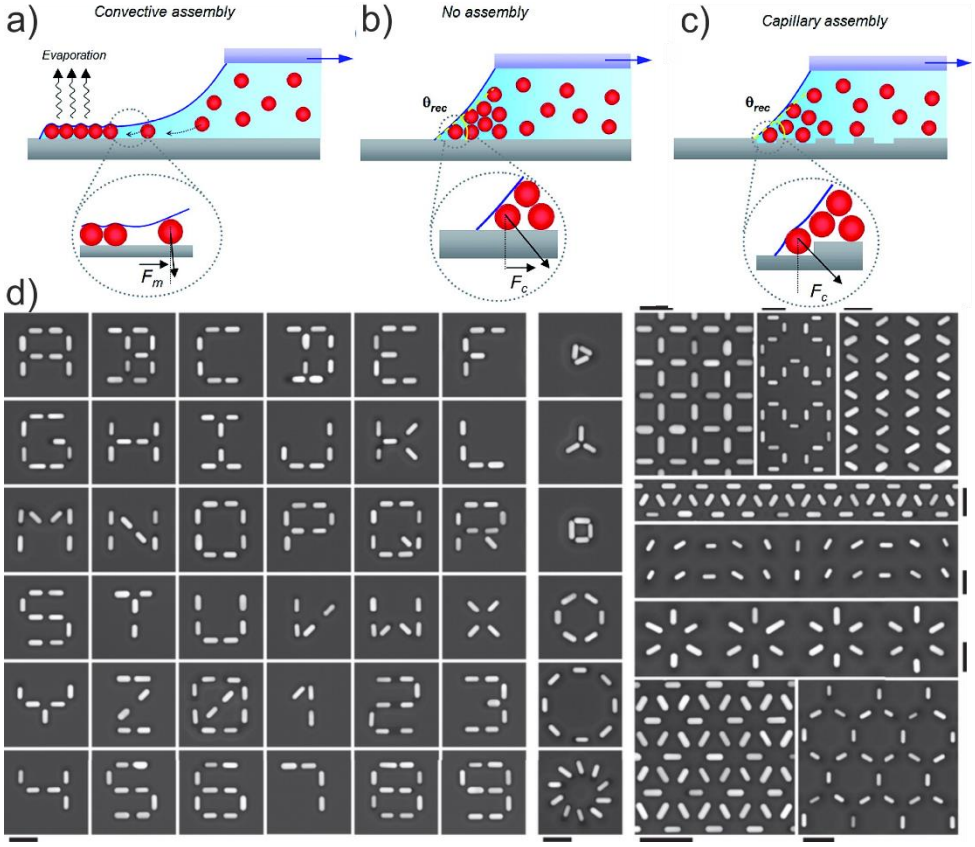

Figure 2.8. Different assembly regimes: a) Convective assembly on a smooth hydrophilic template leading to the formation of particle monolayers. b) Assembly on a smooth hydrophobic template leading to no particles being deposited. c) Assembly on a structured hydrophobic template leading to location specific particle deposition defined by the template topography. Adapted from [109]. d) Au nanorods arranged into a variety of patterns on a topographic template by capillary-assisted assembly. The scale bars in all cases are 250nm. Adapted from [113].

The capillary force does not depend upon the nature of particles and, as such, there is no limitation on materials. A large variety of particles in terms of size and material can be manipulated with a single particle resolution [121]. Not only particles but also a wide array of objects ranging from large molecules [122] to single cell organisms [123] can be manipulated and arranged into a variety of structures as well. Various aspects, e.g., the origins of the driving force [124, 125], the template geometry [112, 113, 118], and the ambient conditions influencing the assembly process [109] have been extensively studied. However, CAPA is still a very recent technique which is rarely used for mainstream fabrication of ordered micro- or nanostructures. In spite of numerous contributions by several authors, the complete description of the assembly dynamics during different process stages and the parametric dependence of its performance is still elusive and needs more profound investigation.

3. METHODS AND EXPERIMENTAL PROCEDURES

3.1 Deposition of Diamond Like Carbon Films

Variety of deposition techniques including filtered cathodic arc, chemical vapor deposition, direct ion beam, electron cyclotron resonance plasma chemical vapor deposition and DC/RF sputtering can be used to deposit DLC films. Direct ion beam deposition in particular has some prominent advantages over the other methods. This technique provides the high degree of control over critical process parameters such as gas flow rate, ion beam energy, ion beam current, substrate temperature and system pressure. This enables to precisely control the properties of the growing film with a flexibility one needs in order to develop multifunctional films. DLC films can be deposited at room temperature onto electrically conductive and insulating materials.

Direct ion beam deposition uses a broad beam ion source to direct an energetic, chemically active vapor/gas flux towards a substrate. Gridded and gridless ion-beam source configurations are used for the deposition. The latter is comprised of two main types – the end-Hall and the closed drift ion sources.

The closed drift ion source operation is based on the principles of electron magnetization. In such configuration, strong magnetic fields created by magnetic coils are used to induce circular motion of electrons in the ion source channel during a discharge. This prolongs the lifetime of the electrons, allowing them to interact with neutral particles and ionize them more efficiently thus creating much stronger electrostatic field in plasma [126]. The ions, on the other hand, are not influenced by the magnetic field because the time span between collisions for them is much shorter than for electrons. Therefore, they tend to move rather straight along the electric field lines from their places of origin (usually near the anode) towards the cathode. The strength of magnetic field in the closed drift ion beam source discharge channel increases from the anode to the ion source exit. This allows the flow of ions to capture the necessary number of electrons thus producing a charge-neutralized beam capable of coating both electrically conducting and insulating substrates [127]. Charge neutralization also enables to maintain high beam currents and allows to achieve very high deposition rates. Since such ion sources run at finite pressure, the ion beam also contains a large flux of unionized species. Due to which the flux ratio of ions to neutrals can be reduced to as low as 10%. Therefore, ion beam sources tend to run best at higher ion energies, typically in the range of 100–1000 eV [76].

The ion beam deposition system URM 3.279.053 equipped with a Hall-type closed drift ion beam source was employed for the production of DLC films. The films were deposited at room temperature using the C_2H_2 (99.6% purity) gas as a precursor. The deposition process was carried out in a vacuum chamber at work pressure of $1\text{-}2\times10^{-2}$ Pa (the base pressure was 2×10^{-4} Pa) with the constant ion beam energy of 800±20 eV and the applied current density of 0.1±0.01 mA/cm^2.

Magnetron sputtering was used to produce silver-doped nanocomposite DLC films. The advantages of magnetron sputtering are the proper chemical composition control, high deposition rate and low substrate heating during the growth of the film [128]. The magnetron sputtering process is conducted in a vacuum chamber where

glow discharge plasma between a target (cathode) and a substrate (anode) is created. The target is being bombarded by the energetic ions generated in the plasma. The ballistic collisions of accelerated ions with the target cause the removal (sputtering) of the target material atoms which then condense on the substrate forming a thin film. Secondary electrons are also emitted during the process; they play an important role in maintaining plasma. In magnetron configuration, the magnetic fields created by the arrangement of magnets trap electrons parallel to the target surface and increase the probability of ionizing electron–atom collisions. This leads to the formation of dense plasma near the target which facilitates the sputtering process [129]. The sputtering gas is often an inert gas, such as argon. In case reactive gasses are being used, it is possible to produce composite films. Magnetron sputtering can be performed in the *direct current* (DC) or in the *radio frequency* (RF) modes. DC magnetron sputtering is mostly used for the deposition of conducting materials, while RF is used to sputter non-conducting materials in order to avoid positive charge build-up on a target which would dampen the sputtering rate.

The modified VY-1A (Smorgon) system equipped with a DC magnetron was used for the deposition of DLC:Ag thin films. A mixture of C_2H_2 (99.6% purity) and Ar (99.9% purity) gases was used as a precursor, and a ∅ 3″ Ag (99.99% purity, Kurt J. Lesker Co.) target was used as the silver source. Coatings with a different Ag content were fabricated and investigated. The deposition conditions for each film are provided in the results section (4.2.1).

3.2 Pattern Generation by Electron Beam Lithography

Electron beam lithography (EBL) uses a focused high energy beam of electrons to expose the radiation sensitive resist. It is the standard method of micro-nanofabrication allowing direct writing of structures down to sub-10 nm dimensions. Even though several other methodologies have been developed offering the same performance, EBL remains the method of choice for prototyping applications and for the formation of masks and templates for high volume patterning technologies such as EUV lithography and NIL. EBL was originally developed by using scanning electron microscopes to which a pattern generator and a beam blanker were added in order to control which areas of the viewing field are exposed [130]. Modern EBL tools are fully dedicated patterning systems that in order to achieve faster throughput employ high brightness electron sources and high resolution mechanical stages that allow step-by-step expose of the large substrates under the relatively narrow field of focus of the electron beam.

According to the exposure method, EBL is mainly divided into two types: the scanning EBL system and the projection EBL system. The scanning EBL system is classified into the raster scan and the vector scan. The raster scan is a method of scanning the whole field depending on the beam blanker thus seeking to achieve patterning exposure. The raster scan method scans the entire field and blanks the beam where exposure is not needed, whereas the vector scan method scans only over the places where exposure is needed and is blanked as it moves between the scanning locations [43].

These direct write systems have the advantage of an extremely high resolution and the capacity to create arbitrary patterns without a mask. Their disadvantages are the expensive and rather complicated equipment as well as the long writing time. EBL is a serial process, where only one point is exposed at a time. The exposure time is therefore directly proportional to the area. Different raster and vector scan modes are used in order to reduce the writing time. Efforts to overcome this challenge include projection EBL [131] and the use of massively parallel beams [132]. Due to the limited scanning width – typically that of a few 100s of μm – the pattern design is divided into writing fields. These writing fields are 'stitched' together by moving the stage. The alignment accuracy of high-end machines is typically around 30 nm, which results in low stitching errors. The key factors to consider in order to achieve high quality, resolution and reliability of pattern production are the quality of the electron optics (e.g., the ability to create a finely focused spot), the choice of resist, the substrate and the developer, and the process conditions: the electron beam energy and dose as well as the development time and temperature. These characteristics are interrelated in a complex fashion. The factors complicating the writing are the delocalization of electrons due to forward and back scattering (proximity effects), the collapse of the pattern due to swelling and capillarity forces, and the fluctuations in the sizes of features (line edge roughness) [44]. Apart from binary structures, EBL also has 3-D patterning capabilities. By using dose modulation, the etching rate in wet developing solutions can be varied. Because high-energy electrons (e.g., 100 keV) penetrate thick resist layers, they dissipate their energy homogeneously over the depth. This means that, at a specific development time, the areas exposed to different doses will etch with different depths. This method (called *grayscale lithography*) allows achieving different steps in resists. It may be further advanced to continuous profiles if thermal reflow techniques are used [133].

In this work, the Vistec EBPG5000Plus direct writing EBL tool (100 keV) was used to fabricate stamps with different geometry patterns for nanoimprint lithography and for CAPA template replication. ZEP520 (Zeon) and *poly-methyl-metha-crylate* (PMMA) positive tone resists spincoated on silicon substrates of a thickness of 500 μm were used as the writing mediums. ZEP520 was used for grating patterns due to its higher edge fidelity, and PMMA was used for CAPA template fabrication. A thin layer of PMMA positive EBL resist (950 kg/mol) spin-coated on silicon substrates was exposed to a dose of about ~400 $\mu C/cm^2$, which is sufficient for the complete removal of the resist. PMMA was used due to the well-established processing parameters even though the exposure is longer than it would be when using a negative resist [134].

3.3 Pattern Replication by Nanoimprint Lithography

Nanoimprint lithography (NIL) is emerging as a high throughput, cost-efficient, high resolution patterning method. This technique is based on replication concept where a substrate coated with a resist layer is put into direct contact with a stamp having a predefined pattern. The shaping process is imposed by deforming the

imprinting material by the means of mechanical displacement. This can be done either by shaping a liquid followed by a curing process for hardening, by variation of the thermomechanical properties of a film by heating and cooling, or by any other kind of shaping process while using the difference in hardness of the mold and the moldable material [135]. After separation, the resist layer is left with a pressed in reverse pattern of the stamp and can be further processed by using standard pattern transfer methods, e.g., plasma etching in order to transfer resist pattern into underneath substrate.

This technique was first put forward by Stephan Chou in 1995 [136] and, since then, it has been a subject of active research and development from not only the academic society but also the industry. Shortly after the first demonstration, the roller NIL which can deliver continuous imprint has been proposed [137]. Essential improvements, such as a combination of nanoimprint and photolithography enabling the fabrication of 3D structures [138], reverse NIL [139] enabling multilayered patterning by coating the stamp surface with a resist and then printing on a substrate with the resist pattern being left on, as well as roll-to-roll implementation further improving efficiency [140] have been demonstrated. Furthermore, the direct imprint of a hard substrate has also been demonstrated by melting a thin layer with high-energy laser radiation [141]. Nowadays, many researchers consider NIL to be one of the most promising patterning techniques due to its capabilities and versatility. As one of the most promising next generation lithography candidates, NIL has been included in the International Technology Roadmap for Semiconductors (ITRS) for industrial manufacturing at 22, 16 and 11nm nodes [44].

In NIL, high resolution patterns can be achieved due to the fact that shaping is not imposed by any kind of radiation; therefore, it's not limited by the diffraction, scattering effects or secondary electrons like e.g., EBL. Resolutions below 5 nm have already been demonstrated [142]. Another unique advantage of molding compared to exposure is that complex patterns, e.g., staircases, pyramids, v-groves, both convex and concave, can be easily replicated. Although nanoimprint lithography has lots of advantages, it is still in its infancy and not without flaws. The contact nature of NIL replication is very different from the noncontact process of the conventional optical lithography, and by itself poses many challenges. The control of pattern defects is among the key issues. Due to the pattern transfer at 1:1 scale, the defects of the stamp must be decreased to zero; otherwise, they will be transferred to imprinting resists. The need for a zero-defect mold, as well as frequent in-fab inspections, add a substantial amount to the total cost of fabrication at the industrial scale. Air bubbles, mold deformation, uneven coating, unparalleled placement between the substrate and the stamp, etc., can also produce a variety of defects. Another important issue is the alignment. The current generation nanoimprint machines lack the expensive precise positioning stages. The necessity of direct contact also increases the difficulty of alignment, which affects the use of the technique in the fabrication of highly overlaid precision devices, e.g., ICs. These issues bottlenecking the use of NIL in the industry have to be eliminated in order to fulfill the requirement of the current semiconductor manufacturing process. Before then, it is at least well suited to be used for the fabrication of less demanding products, such as high-brightness light-emitting diodes,

nonvolatile memory, and solar cells [43].

During the years, three distinct types of NIL have evolved, including *thermal nanoimprint lithography* (T-NIL, sometimes referred to as *hot embossing*), *UV assisted nanoimprint lithography* (UV-NIL), and *soft lithography* (SL). These imprinting methods differ in terms of implementation although the underlying principles remain the same. In UV-NIL, instead of heating to change viscoelastic properties of a resist (like in T-NIL), a liquid photo-curable resist is used which is cured and hardened by an external light source before demolding. For that, a transparent stamp is needed, and the low pressure at room temperature is used during imprint. In soft lithography, a patterned soft elastomer stamp is used. Instead of generating a surface profile in a resist by mechanical hard contact through hard inorganic materials, the pattern is transferred to the substrate by soft, conformal contact using flexible materials [133].

T-NIL uses a rigid template to shape the relief of a thermoplastic polymer which is heated above its glass transition temperature (T_g) via direct mechanical contact. When heated above T_g, the polymeric resist becomes rubberlike – the viscosity decreases and the flowability increases – therefore, it is made more easily displaceable by a squeeze flow induced by applied pressure. In order to fully fill the cavities of the stamp, the pressure as high as 10–100 bar is used in the process. For that matter, the stamps are usually made from a material denoted by high mechanical strength, such as Si, SiO_2, diamond, or metal. The imprint temperature is usually around 50–90ºC above T_g. Within such a process window, the polymer viscosity is low enough for an efficient squeeze flow yet high enough so that high pressure could be applied in order to compensate for the surface unevenness of the substrate and the stamp by conformal bending over large areas.

When the imprint temperature has been reached, the stamp is pressed onto the polymer surface. The stamp is kept in contact with the resist for a certain period of time. This allows the resist to flow into the cavities of the stamp. The stamp filling time is determined by the complex interplay among different parameters. It depends on the size and density of the structure and the polymer flow which is governed by the viscoelastic properties of the material and the induced strain. For a purely viscous material, Stefan's equation can be used to predict the squeezed polymer flow underneath the stamp protrusions. For the line-type stamp topography, it is expressed as:

$$\frac{1}{h^2(t)} = \frac{1}{h_0^2(t)} + \frac{2p}{\eta_0 s^2} t \tag{3.1}$$

where t stands for time, p denotes the applied pressure, $h(t)$ is the height of the polymer in the cavity, h_0 represents the initial thickness of the polymer layer at zero shear viscosity, and s stands for the protrusion width.

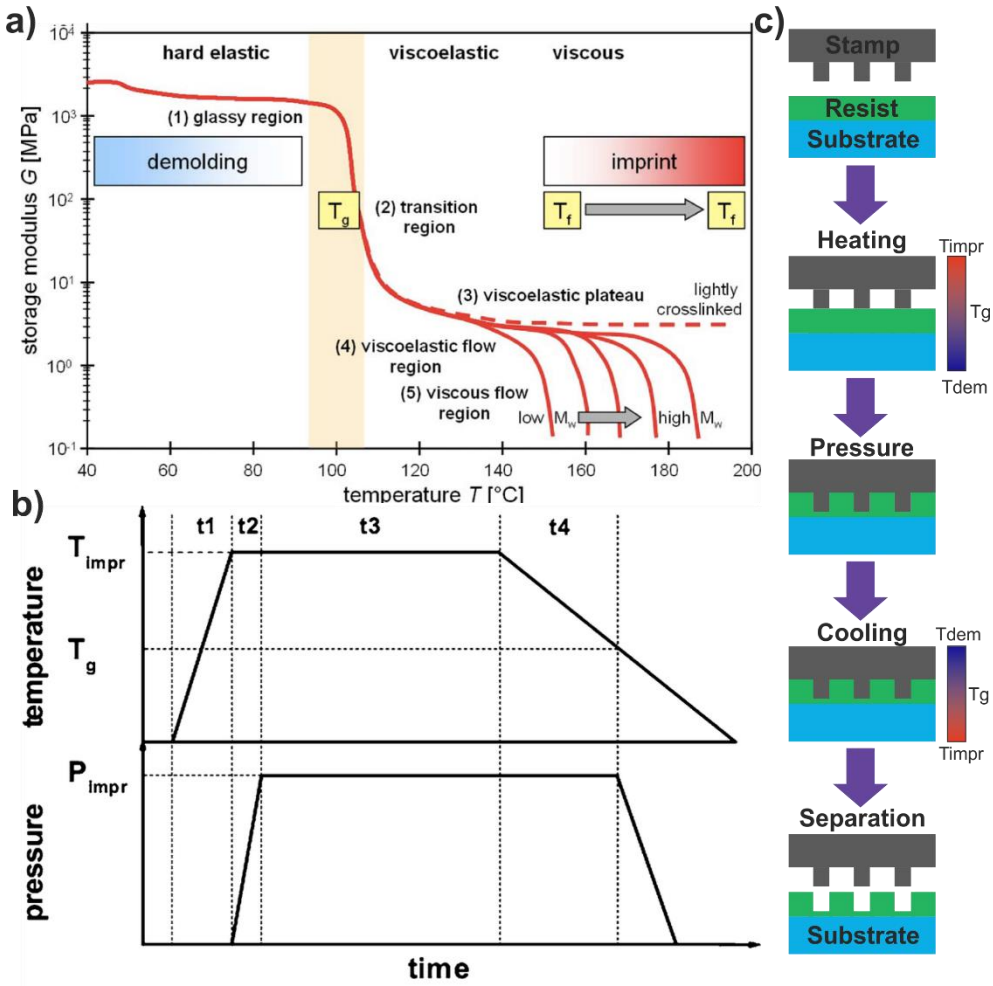

Figure 3.1. Outline of the T-NIL process: a) Dependence of the mechanical properties of a polymer with a T_g around 100ºC on temperature and molecular weight [135]; b) Temperature-pressure temporal relation during the typical T-NIL process [43]; c) Schematic representation of a typical process sequence during T-NIL.

As a direct consequence of Stefan's equation, small cavities will fill faster than the larger ones; hereby, small regular structures in the submicrometer range can be filled within a fraction of a second, whereas large unstructured areas can take up to several minutes to fill. Since pressure and time determine the stamp filling time in an equal way, and as viscosity is a function of both the molecular weight (M_w) of the polymer and T_{impr} (see Fig. 3.1a), the process parameters can be varied to a large extent, and trade-offs are possible, e.g., lower pressure can be compensated by a longer imprint time, etc. Besides that, there is a wide range of polymeric materials with different M_w currently available on the market. Therefore, it is possible to tailor process parameters depending on the needs on molding temperature, dimensional stability in pattern transfer, and application [135].

After the filling, the stamp is kept under pressure during the cooling cycle until demolding temperature (T_{dem}) which is usually 10–40 ºC below the T_g of the resist is reached. Then, the stamp and the substrate can be separated. In order to minimize the adhesion between the imprinted resist and the stamp, a fluorinated material is deposited onto the stamp surface to act as an antiadhesive agent [44]. The general scheme of a typical T-NIL process sequence showing the applied pressure, and the heating/cooling lines versus time is depicted in Fig. 3.1b and c.

The HEX03 nanoimprint machine from Jenoptik was used to pattern SiPol (Microresist GmbH) thermoplastic resist which contains approx. 10% of covalently bonded silicon and has a fairly low T_g of 63 ºC. The formed relief contrast was later used as a hard mask for pattern transfer into DLC films. The key parameters of the tool are presented in Table 3.1.

Table 3.1. The key features of the Jenoptik HEX03 nanoimprint tool.

Parameter	**Value**
Substrate diameter	up to ø150 mm
Resolution	below <10nm
Pressing force	up to 200 kN
Temperature	up to 320 °C
Temperature increment rate	>10 °C/min
Embossing under vacuum	<1 mBar to atmospheric
Alignment accuracy	3 μm

3.4 Pattern Generation by Laser Interference Lithography

Laser interference lithography (LIL) is emerging as a very handy and cost-effective tool for surface patterning. LIL is based on selective laser irradiation of materials by two or more coherent laser beams which superimpose on the sample surface and form an interference pattern [143]. This results in the periodic structuring of the target material either directly (by direct ablation) or through a complete lithographic process when a photosensitive material is used on top [144]. LIL possesses two advantages over other lithography methods; it does not require a photomask – hence patterns of various sizes and shapes can be fabricated easily by changing the configuration of the system, and resolution is only limited by the wavelength of radiation [145]. The biggest limitation of LIL is that only simple periodic patterns can be produced. Mainly because of this reason, this tool has been ignored by the IC industry and has never found its use in large scale industrial applications [146]. However, nowadays, it is an attractive alternative to the conventional methods for applications in which periodic patterns are desirable. LIL has been shown to be applicable for structuring photonic crystals [147], gratins [8], porous membranes [148], magnetic dots [149], etc. There are many possible LIL implementation schemes by using beam splitters [150], diffractive optical elements [151] or Lloyd's mirror interferometer [145]. Lloyd's mirror is particularly attractive due to its simple design and versatility. In the setups where beam splitters are used, phase errors can accumulate when both beams travel long separate paths and

encounter different optical elements. Vibrations, mirror imperfections, spurious scattering and a variety of other deleterious effects may greatly affect the quality [152]. On the other hand, in Lloyd's mirror interferometers, these effects are minimized or even removed completely because there are far fewer optical elements in the setup. Due to these reasons Lloyd's mirror interferometery is the most effective method for imposing patterns over large areas.

In this research, a custom design fully automated holographic lithography setup based on Lloyd's mirror interferometer geometry was constructed and employed to produce sub-wavelength 1D and 2D regular structures. As a coherent radiation source, a 15 mW power and 371 nm wavelength diode pumped solid-state laser (produced by Crystal Laser) with a coherence length extending over 10 meters is used. The substantial coherence length is required in order to fabricate structures over a large sample area. With the help of two dielectric mirrors, the laser beam is directed to a precision spatial filter, where it is cleaned from random fluctuations in the intensity profile. This greatly improves the resolution, which is of critical importance for such applications as holography [153]. A special filter is made of the microscope objective with 99% transmission at the laser wavelength, which is mounted on the translation stage and 20 μm diameter pinhole. The cleaned and expanded beam is directed further to the stage, on which, the sample holder and the mirror which is fixed perpendicularly to the sample plane are mounted (see Fig. 3.2). In the Lloyd's mirror LIL system, a part of the beams travels directly to the sample whereas the other part is reflected by the mirror and subsequently hits the sample. These two beams interfere with each other thus creating an interference pattern of regularly spaced lines, which are recorded into a photosensitive material, such as a photoresist. The period of the structures fabricated by this method depends on the wavelength of the laser and the angle between interfering beams [154]. The period of the interference fringes (P) can be obtained from the following formula:

$$P = \frac{\lambda}{2n\sin(\theta)} \tag{3.2}$$

where λ is the laser wavelength, n is the refractive index of the surrounding medium, and θ is the angle of incidence of the light rays striking the sample plane (see Fig. 3.3).

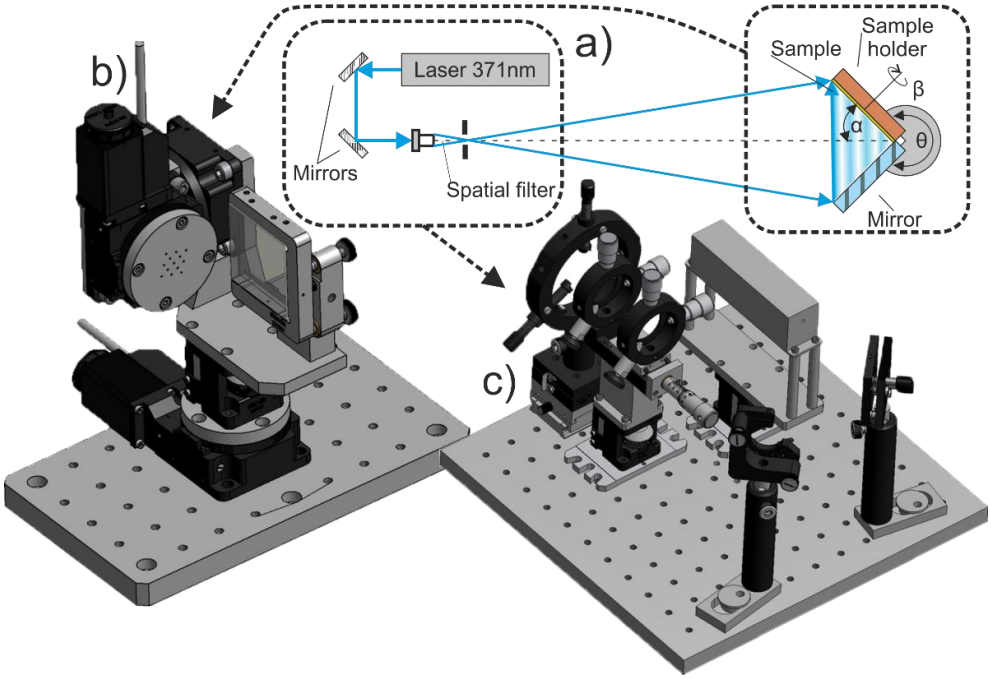

Figure 3.2. Custom laser interference lithography setup: a) Schematic representation of setup *c*; b) Realistic 3D technical drawing of the sample holder stage; c) Realistic 3D technical drawing of the laser stage.

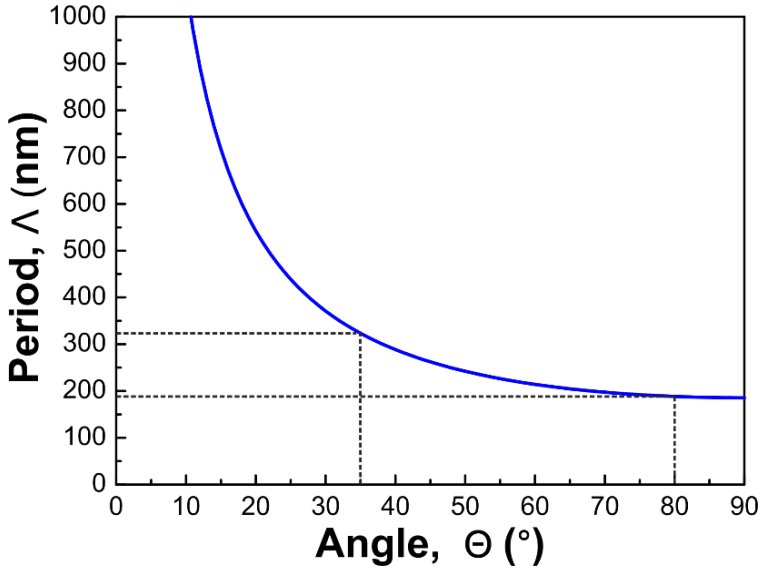

Figure 3.3. The dependence of the period of fabricated structures upon the angle of interfering beams. Dashed lines represent the working range of the setup.

Two motorized rotation stages M8R151 (Standa) were used to control the pattern of fringes. The stages possess a high angular precision of 0.01º. The first stage controls the angle at which direct and reflected from the mirror beams interfere on the sample's surface. The setup allows to vary periodicity of the patterns within the range from ~200 nm to ~300 nm. The second stage is used to change orientation of the sample with respect to the interference field. This allows to create various patterns with different symmetries by performing several consecutive exposures at varying angles. The sample is chunked on the sample holder by using a vacuum pump. In this setup, the sample can also be manually tilted with respect to the plane of optical field thus allowing to record periodic patterns in the third dimension [155]. Both rotation stages as well as the beam shutter are controlled with a computer via custom LabView (National Instruments) interface enabling automated exposure. The whole setup is mounted on an antivibrational optical table in order to minimize mechanical vibrations which can negatively affect the quality of the produced structures.

3.5 Pattern Transfer by Plasma Etching

Etching of solid surfaces can be done by wet processes (wet-chemical etching or electrochemical etching), or by dry processes (physical, chemical, or a combination of both). The areas not supposed to be attacked by the etchant are masked by a protective layer mostly made of photoresist. For the enchased resistance, inorganic materials, e.g., Cr, SiO_2 are used. The mask is removed after the etch process has been completed [156]. Most of the dry etching techniques are plasma-based. They have several advantages when compared with wet etching. These include smaller undercut allowing smaller lines to be patterned, and higher anisotropy permitting high-aspect-ratio vertical structures. However, the selectivity of dry etching techniques is usually lower than that of wet etchants.

Plasma-based etching comes in many varieties depending on how the plasma is generated and how the ions and reactive neutrals are delivered to the substrate to be etched. The three basic dry etching techniques, namely, *high-pressure plasma chemical etching* (PCE), *reactive-ion etching* (RIE), and *ion milling*, utilize different mechanisms. Ion milling is a purely physical process which utilizes accelerated inert ions (e.g., Ar^+) striking the substrate surface [115]. Upon impact, the momentum transfer from a gas ion to the substrate matrix causes a collision cascade triggering the removal of the material. The ions originate from a remote ion source which can be broad-beam, e.g., Kaufman or Hall-type, or focused by electrostatic optics similar to those used in e-beam lithography or SEM thus enabling localized precision etching. The typical operation pressure is $p \approx 10^{-4}$–10^{-3} Torr. The main characteristics of this technique are very low etch rates (in the order of a few nm/min) and poor selectivity (close to 1:1 for most materials). Therefore, it is generally used to etch very thin layers or applied for materials that cannot be etched by chemical means.

In high-pressure (10^{-1}–5 Torr) plasma etchers, highly reactive species are created during collisions when gaseous etchants encounter charged particles. These highly reactive species diffuse to the substrate surface and subject the surface to a chemical attack. For each material, a variety of different chemistries is used. The

products of the reaction are volatile so they diffuse away, and the new material is exposed to the reactive species. Despite the presence of charged particles, there's no intentional physical attack of the substrate surface. This type of chemical etching is much faster when compared to ion milling (in the order of a few hundred nm/min); however, it lacks directionality due to the isotropic nature of the processes.

RIE etching, also called *ion-assisted etching*, is a combination of physical and chemical processes. In this technique, the reactive species created in plasma diffuses to the substrate and preferably breaks the bonds of the surface material, while the physical etching by incident ions removes the surface material by sputtering. Due to the greatly reduced bond strength, this occurs at a substantially greater rate than a physical attack alone could accomplish. The directionality of the ion's velocity produces far more collisions on the horizontal surfaces than on the walls thus generating faster etching rates in the vertical direction. Such a combination of a physical and chemical attack on the bonds of atoms and molecules enables highly anisotropic and fast etching processes. In order to increase the etch anisotropy further, in some cases, side-wall passivation methods are used [115].

The most common tool configuration for RIE is a parallel plate reactor which was introduced back in 1973 [157]. Plasma is generated inside the vacuum chamber by a glow discharge between parallel plate electrodes with the substrate being directly positioned on one of them. The substrate is clamped to the powered electrode which may be covered with a quartz or graphite cover plate to avoid etching of the electrode, and it may also be cooled. The system arrangement is similar to that used for sputtering; however, instead of DC, RF electromagnetic fields are often used to generate dense and stable plasmas. The frequency is typically 13.56 MHz, which is in the center of the frequency band set aside globally for industrial, scientific and medical uses. The RF plasma source determines both ion density and energy [158]. The process pressure is typically between 1.33–27 Pa (0.01–0.2 Torr) [156]. The same type configuration is used in plasma etchers as well (see Fig. 3.4a, b). The difference is that plasma reactors operate at relatively high pressures with the two electrodes roughly equal in area, whereas reactive ion etchers operate at lower pressures with the power electrode being smaller than a grounded one. The asymmetry of the two electrodes, coupled with the use of a blocking capacitor, yielded a negative DC self-bias voltage on the smaller electrode (usually, the powered one). This causes more directional and energetic ion bombardment of substrates placed on the smaller electrode thus enabling anisotropic etching.

A typical RIE tool does not allow to control density and energy of ions independently. However, such a control is useful since the high density of radicals is desirable whereas the high energy of ions is not. A low level of ionic bombardment is necessary for the process, but excessive levels cause poor profiles and a reduction in selectivity against mask material. Such issues can be overcome by a RIE tool equipped with *inductively coupled plasma* (ICP) source as depicted in Figure 3.4c.

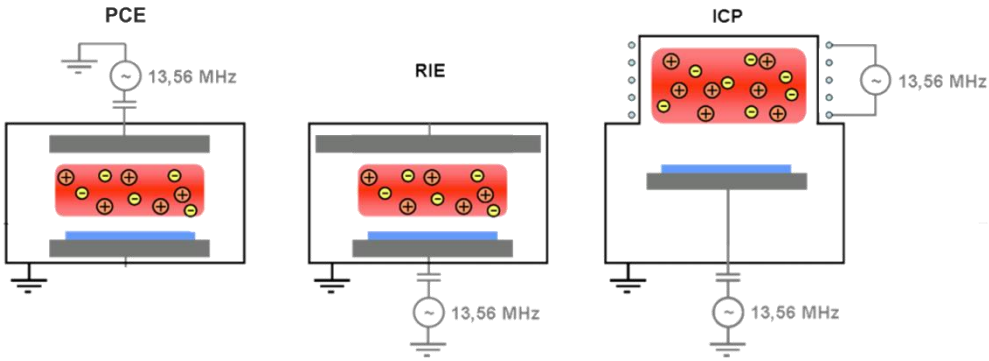

Figure 3.4. A schematic representation of different types of plasma etching equipment: a) Plasma chemical etcher; b) reactive ion etcher (RIE); c) inductively coupled plasma (ICP) RIE etcher. Adapted from [159].

Such system has two individual power supplies which are tuned together and typically operate at 13.56 MHz frequency. One of the supplies drives an external induction coil surrounding the upper part of the vacuum chamber and induces plasma whose strength depends on the coil energy. The second supply powers the table at the bottom part of the chamber and controls the ion energy by creating potential difference between the plasma and the substrate. The substrate is typically either mechanically or electrostatically clamped on the stage [156]. During the etching, the substrate may become very hot and has to be cooled. In advanced etchers, rather than depending on solely mechanical contact for optimal heat transfer, the small gap between the table and the substrate is filled with helium (at a typical pressure of 10 Torr). The resulting heat transfer is molecular; since the gap is orders of magnitude smaller than the gas mean free path, the helium atoms bounce back and forth between the two surfaces, each time transferring heat. Excellent heat transfer is particularly important for the cryogenic RIE process, for which the table is cryogenically cooled [156, 160].

The main parameters to be controlled in ICP etching are gas mixture and gas flow, plasma density (controlled through the ICP power), substrate bias (controlled through the capacitive power), pressure, and substrate temperature. The gas mixture determines which reactive species are possible to achieve in the plasma. The gas flow also plays an important role in generation of radicals as it defines the circulation between precursors and reaction products in and out of the plasma chamber. Plasma density directly correlates with the quantity of ions and reactive species and, therefore, has a large influence on the etch rate. The bias pulls ions toward the surface and, together with the pressure, determines how energetic the ion-substrate impacts are. Stronger ion bombardment can typically yield a faster and more anisotropic etching but can also result in various problems, like material redisposition or trenching which may lead to structural errors in the etching profile. Pressure contributes to the plasma density but also affects the mean free path and, therefore, directionality of the ions. The substrate temperature affects the etch rate, too, since the attack of reactive species is chemical in nature and therefore is sensitive to the temperature. The ability to change all these parameters provides plasma etching with great versatility, yet it also

results in great complexity. Optimizing the etch recipe for a particular purpose is time consuming, and the optimal parameters may vary between machines [161].

In the work presented in this thesis, several aforementioned plasma processing techniques were employed to execute different tasks. Plasma etching was used to etch out carbon matrix of DLC:Ag films in order to reveal and investigate silver content distribution in the films. A Plasma-Therm PK-2430PD unit served to achieve this objective. The etching conditions were as follows: CF_4/O_2 (90%/10%) feedstock gas mixture, RF plasma (13.56 MHz) at 66 Pa (0.5 Torr) pressure, the total flux of gases at 295 sccm (CF_4 at 270 sccm, and O_2 at 25 sccm), with the RF power density of 0.75 W/cm^2 and the substrate temperature equaling 20°C. The etching time of 2, 4 and 6 minutes was set for each coating.

RIE with oxygen plasma was used to clean organic contamination and activate the substrate (silicon, Borofloat glass) surface before resist spincoating and film (DLC) deposition in order to improve adhesion. An Oxford Instruments RIE 80 unit was employed for this task.

An ICP etcher (Oxford Instruments RIE 100) was employed to transfer patterns from resist into silicon during the fabrication of stamps used for both NIL and CAPA templates. More information on this aspect of the thesis is provided in Chapter 3.6.2. The ICP etcher was also used to pattern DLC and DLC:Ag films with nanometer scale structures. More details about the developed of DLC etching process is provided in the results section (Chapter 4.2).

3.6 Capillary Assisted Particle Deposition Equipment

3.6.1 Capillary Assisted Particle Deposition Setup

During capillary force assisted particle deposition, long ranging capillary interactions manifesting on the edge of the droplet meniscus are exploited to deposit particles dispersed in a *colloidal solution* (CS) into predefined positions on a template surface. In this process, it is very important to bring patterned surface and particles in a controlled way where convection and other disturbing influences are minimized. Particle deposition is triggered by appropriate (directed towards phase-boundary) hydrodynamic flow created by dragging a droplet of CS over a patterned template surface at certain ambient conditions. The ability to control and monitor locality, temperature and movement of the droplet is needed in order to prevent nonspecific deposition and agglomeration of particles during the course of procedure, and it is of crucial importance for a high-yield assembly.

The custom-built setup fulfilling the above-mentioned criteria based on H. Wolf's (IBM) design was assembled and employed to execute all capillary force assisted particle deposition experiments presented in this thesis. The setup consists of an advanced optical microscope system, a motorized high precision linear translator, a coverslip positioner and a vacuum chunked sample holder of controllable temperature (see Fig. 3.5). This setup allows to control the temperature and the velocity of the CS droplet with an exceptional precision. An optical microscope provides possibility to directly observe the assembly process enabling immediate response to changing conditions.

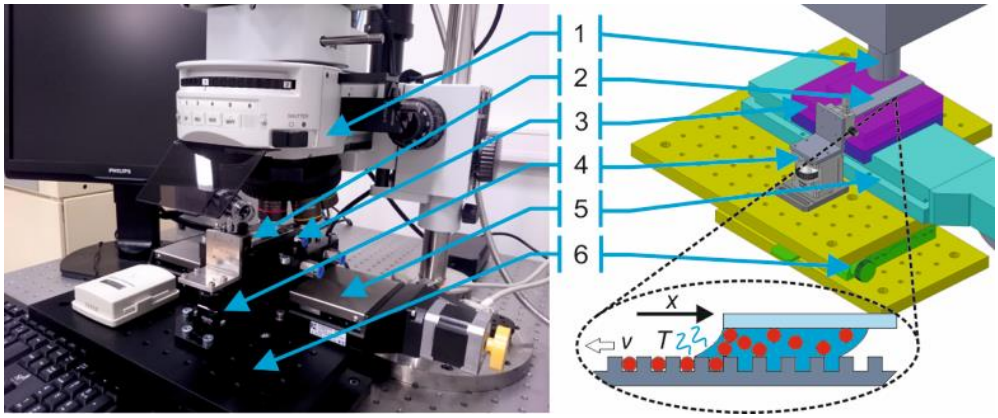

Figure 3.5. A photograph and a schematic depiction of the capillary force assisted particle deposition setup: 1) Optical microscope; 2) Glass coverslip; 3) Controlled temperature sample holder; 4) Height positioner of the glass slide; 5) Motorized precision translator; 6) *XY* positioning stage. The inset depicts the process of particle deposition where *v* denotes the velocity of the translator and *T* stands for the temperature of the colloidal solution. The *x* axis represents the direction of deposition.

During deposition, the template is placed on top of the sample holder and held in place by using a vacuum chuck. The temperature of the sample holder (as well as the template) is monitored and controlled by using a Peltier element and a Pt100 thermoresistance sensor which are driven by the TEC-1090 (Meerstetter Engineering GmbH) thermoelectric cooling controller. The back side of the Peltier element is water cooled and, by tubing, it is conected to a fanless high thermal design power heatsink. Such configuration can maintain the stable temperature over the whole template area with an accuracy of 0.01°C. The sample holder is mounted on top of the linear translation stage. The droplet of CS is constrained between the template and the glass coverslip. Particles are assembled on the surface of that template as it moves relative to the stationary coverslip. The motion of sample is controlled by using an LS-110 (PI Micos) translator with the velocity resolution of 100 nm/s.

The whole setup is mounted on stacked 7T167-100Q (Standa) translation stages providing XY sample positioning with respect to the upright microscope objective, which enables direct observation and recording of the particle deposition process. The microscope in use (Olympus BX51) can work in bright and dark field regimes and is equipped with two light sources. A mercury short-arc UV light source (Lumen Dynamics X-Cite Series 120Q) is used for illumination to observe fluorescence. A halogen light source (Schott KL 1500 HAL) is used for regular observations. The microscope has two cameras: a high resolution colored CCD camera (QImaging Micropublisher 3.3) and a fast response monochromatic camera (QImaging optiMOS) which are used for recording. A small form factor digital microscope is employed to observe the side-view shape of the droplet. In order to provide mechanical stability, the entire microscope and deposition setup arrangement is placed on a vibration-free optical table.

Particle assembly experiments were carried out at ambient temperature ranging from 18 to 25°C and at a relative humidity of 25 to 40%. The dew point for these

conditions was estimated to be in the range of 2 to 7°C. The template temperature during different depositions varied between 8°C and 18°C above the dew point respectively. A small amount (20–30 µl) of the prepared particle solution was used each time. The gap between the template and the coverslip restraining the CS droplet was set to be equal to 1 mm. The receding contact angle of the CS during deposition was measured to be 45±2°.

3.6.2 Template Fabrication

The templates were cast from silicon masters. *Electron beam lithography* (EBL) and *reactive ion etching* (RIE) were employed to produce silicon masters for *polydimethylsiloxane* (PDMS) replication. Master stamps of different geometries were fabricated by using an EBPG 5000Plus (Vistec) direct writing EBL tool. A PMMA positive e-beam resist was spin-coated on silicon substrates and exposed as described in Section 3.2. After the development for 60 s in *methyl-isobutyl ketone* (MIBK) mixed with *isopropyl alcohol* (IPA) at a ratio of 1:1 and the opening of exposed windows by etching with oxygen plasma seeking to remove any PMMA residues, the resist with the desired structures was used as a mask to transfer the patterns into silicon by using SF_6/C_4F_8 ICP RIE plasma. Prior to use, the Si masters were cleaned by oxygen plasma (Oxford RIE80) and then silanized by trichloro-(1H,1H,2H,2H-perfluorooctyl)-silane. The silanization was performed in a custom vacuum chamber at 10 mbar pressure for 10 min. The typical masters were 20×20 mm^2 in total surface area and had 18×18 mm^2 patterned areas.

Inverse geometry of the master stamps was replicated into PDMS by casting. PDMS replicas were used as the templates to assemble particles. A silicon elastomer mixture comprised of a base monomer and a curing agent (Sylgard 184, Dow-Corning) at 10:1 ratio was prepared and mixed in a centrifuge (Thinky Mixer ARE-250) at 1200 rpm for 5 min and later at 2000 rpm for 5 min. The mixture was then placed into a vacuum chamber (KNF Vacuum Pump System SC 920) and kept at 15 mbar pressure for 15 min to degas. A small droplet (about 20 µl) of PDMS mixture was constrained between the silicon master and a thin glass coverslip. The weight of the applied glass plate helped to distribute the polymer mixture evenly. The sandwiched structure was then annealed at 100°C for 35 min to cure PDMS. Afterwards, the templates with inverted surface patterns were cooled down to room temperature and peeled off from the mold. The glass slip was kept intact as a substrate providing stability and robustness for the PDMS template. All different template geometries that were used are listed in Table 3.2. Template No.1 which was made of Si covered with a monolayer of an antiadhesive material was not fabricated in the manner described above. It was acquired from dr. J. Henzie from NIMS in Japan.

Table 3.2. Different types of templates used for particle assembly.

No.	Material	Patterned area (mm^2)	Trapping sites	Trapping sites geometry
No. 1	Silicon	30×30	pits	Rectangular holes of varying sizes
No. 2	PDMS	18×18	pits	Rectangular holes of 2×2 μm
No. 3	PDMS	18×18	pits	Circular holes of ∅ 300 nm

3.6.3 Preparation of Colloidal Suspensions

Aqueous colloidal solutions of fluorescent *polystyrene* (PS) beads and silver particles of the regular octahedron shape were used in the deposition experiments. PS beads were acquired from commercial sources (Thermo Scientific) while silver nanocrystals were synthesized by dr. J. Henzie. Octahedral Ag NPs showcasing exceptional monodispersity in both size and shape were synthesized by the polyol method reducing a metal salt in a diol solvent at an elevated temperature and in the presence of a polymeric stabilizing agent. The procedure in more detail is described in [111, 162]. All different particle solutions (as acquired) which were used in this work are presented in Table 3.3. In order to tailor acquired colloidal particle solutions for CAPA experiments, they were further diluted 10-fold to a 0.1 wt.% concentration with deionized water. A small amount (5 vol.%) of surfactants (Sodium-lauryl-sulfate, Sigma Aldrich) ware also added into the mixture in order to enhance the wettability of the droplet. When not in use, prepared colloids were stored in a refrigerator at 4°C temperature. Before each deposition, CSs were sonicated for 15 minutes in an ultrasonic bath.

Table 3.3. Colloidal particle solutions used for the preparation of tailored solutions for CAPA.

No.	Particle Material	Particle size (nm)	Particle shape	Fluorescence	Particle concentration (wt.%)	Particle concentration (part/ml)
No.1	PS	270	Spherical	Green	1.0	9.33×10^{11}
No.2	PS	90	Spherical	Blue	1.0	2.52×10^{13}
No.3	Ag	300 (side)	Regular octahedral	–	~1.0	$\sim6.33\times10^{9}$

3.7 Analytical Equipment

Numerous analytical techniques were used to determine a variety of aspects (chemical composition, optical properties, etc.) of the fabricated DLC and DLC:Ag films and to evaluate the particle assembly. All the techniques and the instruments that were used are listed below:

1. *Atomic force microscopy (AFM)* was used to evaluate the topography of the regular structures fabricated by using Lloyd's mirror interference lithography setup. AFM is a type of scanning probe microscopy which is used to image the topography and to characterize the morphology of surfaces even at atomic resolution. It is also capable to produce valuable information on local material properties, such as elasticity, hardness, adhesion and surface charge densities [163]. AFM uses a cantilever with a sharp tip at the end to scan the surface of a sample. The local attractive or repulsive forces (e.g., van der Walls forces) between the cantilever tip and the sample surface impose bending or deflection of the cantilever which mimics the topographic features. The bending/deflection of the cantilever is detected by a laser beam that is reflected from the cantilever onto a photodetector. The photodetector is usually a photodiode with quadrupole-electrode geometry. The laser spot falls on a different part of the photodetector depending on the position of the cantilever. A piezo-scanner is used to move a sample along the horizontal plane under the probe tip from point to point in a manner of the raster pattern. A JPK Nanowizard 3 tool was used to perform topographic measurements and depth profiling. The contact mode was used in all measurements.

2. *Scanning electron microscopy (SEM)* was extensively used to investigate and evaluate the fabricated DLC structures as well as CAPA arrays. Scanning electron microscopes share similarity with optical microscopes where electromagnetic waves scattered from the specimen are detected by using a system of focusing lenses. However, in electron microscopes, electrons are used instead of electromagnetic radiation, and electrostatic or magnetic lenses are used instead of glass lenses [42]. The advantage of using electrons is that they can be focused to a very small spot size (up to ~0.4 nm in diameter) thus enabling very high resolution imaging capable of revealing details down to several nanometers [164]. Electrons with the energy ranging from 0.2 keV to ~40 keV are generated by a hot filament or field emitters. The latter can deliver superior image quality and therefore are solely used in modern SEMs. Interactions between electrons and solids are quite complicated. Due to electric charge, as incident electrons interact with electrons and ions in solids, even a parallel beam becomes defocused. Such interactions result in the backscattering of electrons, production of secondary electrons, visible light, UV light and even X-rays depending upon the energy of the incident electrons, the type and the thickness of the sample. Secondary electron imaging is the standard mode of operation in all SEMs (additionally back-scattered electrons can be imagined). The fine beam is scanned or rastered on the sample surface by using a scan generator, and secondary or backscattered electrons are collected by the appropriate detector. The signal from the scan generator along with the amplified signal from the electron collector generates the image of the sample surface. Samples can be observed in high and low vacuum conditions [42]. In the

SEM, specimens must be electrically conductive or at least electrically grounded so that to prevent the accumulation of an electrostatic charge at the surface. For proper SEM imaging of non-conducting samples, a very thin conductive film is usually deposited by using PVD methods. FEI Quanta FEG200 and Zeiss Supra VP55 field emission SEMs were used in this work.

3. *Energy dispersive X-ray spectroscopy (EDS)* was employed to determine the elemental composition of DLC:Ag films. Besides imaging, SEM can be employed to determine the composition of the sample when it has an energy dispersive X-ray spectrometer attached. The high energy electrons striking the sample produce characteristic X-rays of the atoms they are interacting with. The X-ray generation is initiated by the ejection of an inner shell electron to form a vacancy. When an upper shell electron drops into the inner shell vacancy, the X-ray photon is generated with the energy equal to the difference between the energies of the electron shells, and this energy is unique for different elements [165]. The produced X-rays are collected by the detector. A standard EDS detector contains a crystal that absorbs the energy of the incoming X-rays by ionization thus yielding free electrons in the crystal which becomes conductive and produces an electrical charge bias. The X-ray absorption thus converts the energy of individual X-rays into an electrical signal of the proportional size, which corresponds to the characteristic X-rays of the element. The signal intensity at different energy levels is proportional to atomic concentration. EDS can detect elements from *Boron* (No. 5) to *Americium* (No. 95). The information can be acquired from the depth of up to several micrometers. The composition of the DLC:Ag films was obtained by employing an EDS spectrometer Bruker Quantax with an XFlash 4030 detector**.**

4. *X-ray photoelectron spectroscopy (XPS)* was employed in order to evaluate the surface chemical composition of DLC:Ag films. The technique is based on the photoelectric effect. It is essentially the opposite of the EDS technique. High energy photons (X-rays) incident on the sample surface are used to initiate ejection of the photoelectrons. Upon knowing the photon energy and by measuring the kinetic energy of the fotoelectron (with an energy analyzer), binding energy of an electron in an atom can be determined. In solids, however, the additional energy (the work function) is required for an electron to get emitted. The work function of solids changes from material to material and also depends on their cleanliness and purity. Fortunately, when kinetic energies of the emitted electrons are measured with reference to the Fermi level, the work function of the sample can be replaced by the work function of the spectrometer which is known. The measured binding energies are characteristic to a given element and are used to identify the elemental composition of the sample. Moreover, photoelectrons have energies which are quite sensitive to their local

environment. Thus, the measurement of binding energies yields useful information on what kind of chemical bonds are present. Electrons have a much shorter mean free path in solids than X-rays. Therefore, even if photoelectrons can be generated deep within a solid, few of them can escape out of it. This renders XPS essentially into a surface analysis method with typical analysis depths of up to several dozen nanometers [42]. A VersaProbe III XPS spectrometer from Physical Electronics with a micro-focused scanning X-ray source was used to perform the analysis.

5. *Ultraviolet–visible–near infrared (UV-VIS-NIR) spectroscopy* was used to evaluate optical properties of the deposited and plasma processed DLC:Ag films. UV-VIS-NIR spectroscopy can help to understand the electronic structure and transitions between the valence and the conduction band of materials. In case of metal thin films or particles like gold or silver being dispersed or suspended in a matrix, absorption due to the surface plasmon resonance can be observed. The peak width and the position depend upon the size as well as upon the size distribution of the particles. The UV-VIS-NIR spectrometer's setup in principle is quite simple. A high intensity lamp emitting radiation from UV to NIR region is used as a light source. Usually, hydrogen discharge lamps, deuterium lamps or tungsten lamps are used. A monochromator selects different wavelengths which fall onto the sample. Depending upon its properties, the sample reflects or absorbs certain wavelengths and transmits remaining ones. The transmitted (or reflected) intensity at different wavelengths is detected by a photodetector. Common monochromators are gratings or prisms. Photodetectors can be photodiodes or CCD arrays. The absorbed (or reflected) intensity is depicted as a function of the wavelength [164]. The optical properties of the nanocomposite DLC:Ag films were investigated by using the optical spectrometer system Avantes which is composed of a deuterium halogen light source (AvaLight DHc) and a spectrometer (Avaspec-2048). The absorbance of the films was analyzed in the wavelength region from 250 nm to 800 nm.

6. *Fourier transform infrared spectroscopy (FTIR*) was used in order to determine the ratio of different types of bonding between carbon atoms in DLC:Ag films, namely, the ratio between the sp^3 type bonds typical for diamond and the sp^2 type bonds associated with graphite. Infrared spectroscopy exploits the fact that molecules have characteristic vibration energy levels and therefore they absorb frequencies that are characteristic of their structure. Characteristic absorption bands for molecules occur as molecules undergo transition from one characteristic energy level to another. This transition occurs by the absorption of a photon typically at the energy levels of the IR region [164]. Each IR active molecule has a unique absorption spectrum which can be used to determine the composition and the functional groups. An FTIR spectrometer makes use of the Michelson

interferometer for recording the spectra. A parallel beam of infrared light rays from the source falls onto the beam splitter. The beam is splited so that a part of the beam falls on a movable mirror and a fixed mirror. The rays are reflected from both mirrors along the same path so that a part of this combined beam falls back on the sample and the detector. The beam containing a broad continuous spectrum of wavelengths produces a constructive and destructive interference pattern, in which, certain characteristic frequencies are absorbed by the molecules present in the sample. The FTIR spectrometer collects simultaneously the data at various frequencies by varying the retardation (the difference in the optical path length between the two arms to the interferometer) and is much superior to the conventional way of sequentially scanning different wavelengths. Fourier transformation is then employed to decouple the complex spectrum into various frequencies [42]. A Vertex 70 FTIR spectrometer from Bruker Optics Inc. equipped with a 30Spec (Pike Technologies) specular reflectance accessory having a fixed 30^{o} degree angle of incidence was used in this study. For each spectrum, the average of 100 successive scans over the range of 400–4000 cm^{-1} at a resolution of 4 cm^{-1} was recorded. Obtained data was processed using OPUS 6.0 (Bruker Optics Inc.) software.

7. *Refractometry* was used in order to determine the refractive indexes of the analyte solutions which were used to calibrate sensitivity of the produced DLC gratings based sensor chips. Refractometry is based on the total internal reflection phenomenon. When the light wave travels from an optically denser medium into a less dense medium at a certain angle (the critical angle), total internal reflection occurs where no light passes through the boundary and is entirely reflected. When the refractive index of one medium is known, the other can be determined from Snell's law by varying the angle of incidence until the total internal reflection condition has been met. The measurements were conducted by using an Abbe Refractometer Type G (Carl Zeiss). The main components of the tool are as follows: the measurement and illumination prism body, the focusing telescope, and the graduated scale with the reading microscope. During the measurement, the liquid specimen is sandwiched between the illumination and the measurement prisms. The focusing telescope located on the back side of the measurement prism is used to observe the boundary line. The prism body is turned until a sharp line between the bright field and the dark field indicating the total reflection is seen through the telescope's eyepiece. At that point, the value of the refractive index can be read from the graduated scale. With this setup, the refractive index can be determined within the range from 1.300 to 1.700 with the accuracy of $0.001 \pm 2 \cdot 10^{-4}$ [166].

8. *Raman spectroscopy* was used in order to assess the scattering enhancement which metallic NP orderly assemblies have on the intensity of the signature Raman signal. This technique is based on inelastic scattering of monochromatic light. During such interaction, a photon and a target molecule exchange energy thus causing the scattered photon's frequency to shift away from the initial wavelength, which produces signature Stokes or anti-Stokes (depending on whether energy was gained or lost during the interaction) lines in the spectrum. Since these wavelength shifts arise from the change in the vibrational, rotational or electronic energy of the excited molecule, they provide feasible means for 'fingerprint-like' molecular identification. However, spontaneous Raman scattering is prominently rare. Typically, only one or fewer than one out of 10^{12} incident photons undergoes inelastic scattering; therefore, the scattering signal is weak, particularly in situations when the concentration of analyte is very low [167]. Substrates which can produce intense local electromagnetic fields when excited by the probing light are shown to greatly improve the scattering probability and the signal intensity. In this work, SERS measurements were carried out by using an inVia Raman spectrometer (Renishaw) equipped with a confocal microscope (Leica). This setup uses a 532nm, 45mW solid state laser as the radiation source. The laser beam is focused onto the sample by using an objective lens. The scattered light from the sample is directed to the spectrometer through the collection lens where the Raman signature is recorded by a CCD detector. Appropriate filters and automated aperture selectors are used for Rayleigh signal elimination and spectral resolution control.

3.7.1 Optical Characterization of DLC Gratings

Optical measurements of the GMR response in DLC linear gratings were carried out by using a custom optical setup consisting of a polychromatic light source (a halogen lamp), collimating optics and a Glan–Taylor polarizing prism, a thermostated fluidic cell with a sensor chip (DLC grating on a borofloat glass substrate 20×20mm), fiber optics and a spectrometer. The schematic depiction of the setup is presented in Figure 3.6a. The fluidic cell together with the diffraction grating is mounted on a goniometric stage having resolution 1′. The fluidic cell is fabricated from a *polytetrafluorethylene* (PTFE)-based compound. On the front side of the cell, the mounting site is positioned, where the chip with the diffraction grating is fixed (see Fig. 3.6b), and on the back side, a thermoelectric Peltier element is placed. This thermoelectric element is water-cooled and driven by a TEC-1090 (Meerstetter Engineering GmbH) temperature controller allowing precise temperature setting and stability up to 0.01°C during the measurements. The temperature in the fluidic cell is monitored with PT100 temperature sensors. During the measurements, the cavity in between the thermoelectric element and the DLC sensor chip is filled with liquid analyte through several inlets and outlets. The polarized white light spectra reflected from the grating are coupled to an optical fiber connected to an AvaSpec-2048 (Avantes) spectrometer using a quartz lens fixed on a motorized platform that can be

rotated independently around the same axis as the cell with the grating. The spectrometer collects the data within the spectral range between 350 and 850 nm and features a resolution of 1.2 nm. The whole setup is automated and controlled through custom LabVIEW (National Instruments) software-based interface [168].

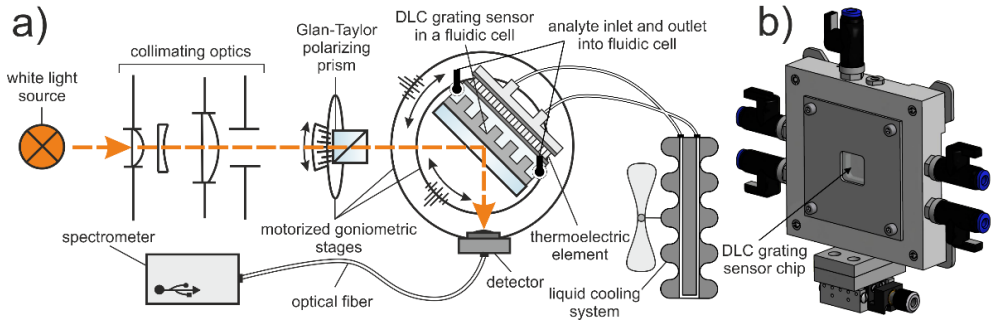

Figure 3.6. a) Schematics of the optical setup used to evaluate the optical response of the DLC gratings; b) A realistic technical drawing of the measurement cell.

3.7.2 Analytical Software

Numerical simulations of the polarized white light reflection spectrum from DLC and DLC:Ag gratings were done by employing GSolver v5.2 (Grating Solver Development Co.) software package. The simulations were performed in order to validate and indirectly evaluate the quality of the fabricated structures. GSolver employs a class of algorithms known as *Rigorous Coupled Wave Analysis* (RCWA) to give the numerical solution of Maxwell's equations for periodic dielectric structures or thin film stacks. As such, it is particularly suitable for the task. GSolver is a handy tool which allows to obtain reflection and diffraction efficiencies by visually defining the geometry of the structure and providing complex refractive index values (both real and imaginary parts) for the materials involved. Spatially-continuous grating structures can be approximated by a series of thin layers, each of which consists of rectangular regions of constant indices of refraction. Staircase approximation has to be used for the realization of curved geometries where scaling allows to achieve desired level of accuracy [169]. This software, however, is unable to represent multi-dimensional data, e.g., diffraction efficiency at different wavelengths or angles of incidence. Therefore, in order to cover the broad-band spectrum, many simulations had to be executed. The obtained data was stored in a database built in Matlab (Mathworks) and explored as well as extracted by using locally available visualization tools.

ImageJ 1.48v (NIH), the open source image processing software, was used to analyze SEM micrographs of plasma etched DLC:Ag films in order to identify and extract the data on the count and size of the particles exposed to the surface. This data was processed by using Matlab and Excel (Microsoft) with the objective to sort-out and approximate their size distribution.

4. RESULTS

4.1 Patterning of Diamond Like Carbon Films

4.1.1 Development of Patterning Method

The patterning of diamond like carbon (DLC) and DLC nanocomposites is of interest for an increasing number of applications. DLC as well as other carbon based materials, e.g., diamond or polymeric resists, can be etched by reactive ion etching (RIE) using pure oxygen plasma [170]. As masking layers, it is possible to use polymer resists of the suitable height for 'competitive' etching, or hard masks, such as thin Cr or SiO_2 films, for enhanced etch resistance. Frequently, multilayer-resist strategies are pursued, e.g., for patterning a thin hard mask with a polymer resist or for patterning a thick polymeric transfer layer with a thin hard mask. When choosing the suitable masking layers, the aim was to use a T-NIL compatible process which would require the minimum number of processing steps and at the same time would offer good selectivity towards DLC thus enabling direct pattern transfer.

Due to etching with oxygen plasma, the use of standard resists (i.e. PMMA, photoresist, etc.) is hampered since the selectivity between typical organic resists and DLC is extremely low [20]. The use of Cr in a bilayer system would add unnecessary complexity. Additionally, the inclusion of metallic particles (in the case of DLC:Ag nanocomposites) prohibits the use of metallic hard masks for enhancing selectivity since it may result in the removal or modification of the nanoparticles on the DLC surface. Therefore, a SiPol (Micro Resist Technology GmbH) thermoplastic resist (glass transition temperature T_g=63°C) with a 10% content of covalently bonded silicon was chosen. The presence of silicon makes it highly resistant to oxygen plasma. This enables to use it as spin-coatable and imprintable hard mask combined with good etching selectivity towards DLC. Initially, SiPol was developed to be used in a bilayer system with an organic transfer layer UL1 (Fig. 4.1 a–b) [171]. In the standard process, the patterned SiPol layer is thinned down by fluorine based etching chemistry thus etching both the organic and inorganic content of SiPol, which results in the removal of the residual layer. After opening the SiPol mask windows, oxygen plasma is used to pattern the purely polymeric transfer layer UL1 and at the same time to convert the SiPol masking layer into almost pure silicon oxide. This transfer layer at the same time has the function of improving the adhesion to both the substrate and the SiPol layer. However, for the etching of DLC materials in pure O_2 plasma, anisotropy is too high for UL1 even when inductively coupled plasma (ICP) systems are used enabling to obtain only very shallow DLC structures (Fig. 4.1b). In order to prevent this issue, the T-NIL process was optimized as described in more detail in the following chapters to replicate the SiPol directly on the DLC coatings, without UL1 as an intermediate layer, which results in much deeper structures (Fig. 4.1c). Furthermore, in order to simplify the process and reduce the number of steps, we intended to eliminate the fluorine chemistry step and sought to use directly the oxygen plasma for the conversion of SiPol into a SiO_2 hard mask. For this purpose, the residual layer had to be as thin as possible and ideally close to 0 nm.

The optimized processing scheme used to pattern DLC (as well as DLC:Ag) films in the step-by-step fashion is graphically depicted in Figure 4.2. In step (1), DLC films were deposited on silicon and Borofloat glass substrates by direct ion beam deposition by employing a closed drift ion beam source and using acetylene gas as a precursor. The process is described in Section 3.1. No investigation regarding the chemical composition, mechanical or other properties of DLC films was pursued in this work because extensive investigation regarding this matter in terms of the same films can be found elsewhere [172]. This work is solely interested in the patterning of the explored material. Contrary, for the DLC:Ag films, chemical and optical analysis is provided. DLC:Ag films were fabricated by direct current reactive magnetron sputtering using a mixture of argon and acetylene gas and a silver cathode. Before the deposition, substrates were cleaned in acetone (VLSI quality) in an ultrasound bath for 1 minute and rinsed in isopropanol. Additionally, oxygen RIE plasma cleaning was used to remove the remaining solvents and activate the surface prior to DLC deposition. Substrates with DLC films were directly spin-coated with SiPol thermoplastic resist (step 2). Nanoimprint lithography with incomplete stamp filling was used to replicate the reverse patterns of the silicon stamp into the resist layer (step 3). Reactive ion etching by oxygen plasma was employed to transfer the patterns into DLC (step 4). Reactive ion etching by fluorine plasma was employed to remove the remaining resist layer of the DLC surface (step 5). Crucial processes of the pattern transfer by nanoimprint lithography and reactive ion etching of the DLC coatings are discussed in greater detail in the following chapters [168].

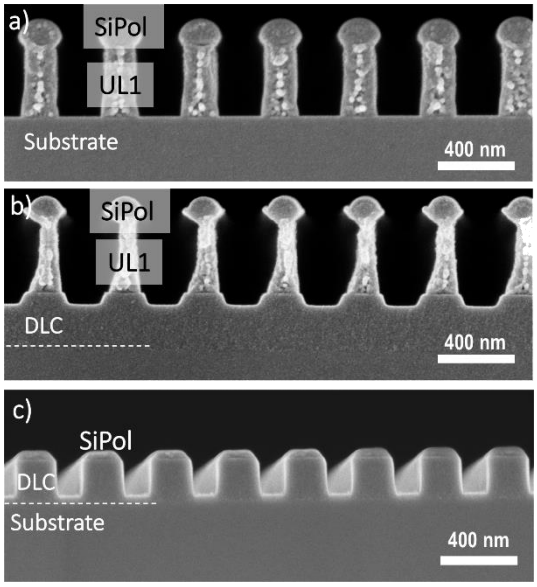

Figure 4.1. Cross-sections of etched grating structures: a) Structures etched in a bi-layer SiPol-UL1 resist mask; b) Bilayer SiPol-UL1 resist mask used to etch into DLC showing high under etching of the UL1 layer; c) DLC etched by using only SiPol resist mask.

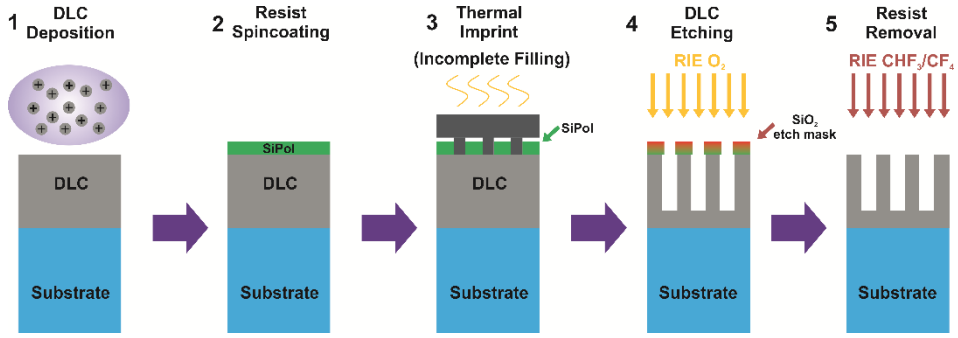

Figure 4.2. A schematic depiction of the processing steps of DLC patterning when using SiPol resist as a hard mask:1) Plasma deposition process was used to grow thin DLC films; 2) A thin layer of silicon containing resist was spin-coated directly on DLC; 3) Nanoimprint lithography with incomplete stamp filling was used to replicate the reverse patterns of the silicon stamp into the resist layer; 4) Reactive ion etching by oxygen plasma was employed to transfer patterns into DLC; 5) Reactive ion etching by fluorine plasma was employed to remove the remaining resist layer of the DLC surface.

4.1.2 Patterning by Thermal Nanoimprint Lithography

T-NIL was chosen as a method of patterning due to its large area, high throughput patterning capabilities with nanoscale resolution. Silicon masters fabricated with a direct writing EBL tool were used as stamps to transfer the reverse patterns into SiPol. A HEX03 (Jenoptik) hot embossing tool was used for the imprint. In order to prevent isotropic etching effects in the UL1 transfer layer, substrates with the DLC films were directly spin-coated with the SiPol thermoplastic resist. However, due to poor adhesion between DLC and SiPol, the conventional imprint routine when the resist completely fills stamp cavities was found to be unsuitable for densely packed patterns. Lack of adhesion between DLC and SiPol always resulted in complete or partial resist peel-off from the substrate (Silicon or DLC) during the stamp separation (Fig. 4.3). None of the conventional measures, e.g., surface pre-treatment (plasma, baking), variation of the imprint conditions or a low demolding temperature could provide a significant positive effect. Therefore, the standard imprint process had to be modified to avoid resist peel-off during demolding.

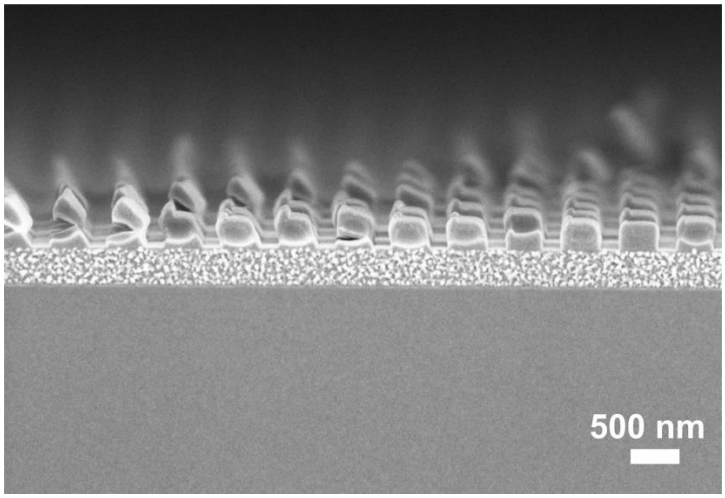

Figure 4.3. Partial SiPol resist peel-off from DLC after demolding when the patterning is done with complete filling of the stamp cavities.

The strategy of incomplete filling of the stamp cavities was pursued in order to minimize the contact area of the resist with the stamp and achieve no residual layer. Stamps with 250 nm deep linear grating patterns were used with an intended filling height of 120–200 nm for a 60–100 nm thick initial resist (calculation with a grating of 400 nm period and 200 nm structure width). SiPol resist was diluted with *propylene-glycol-methyl-ether acetate* (PGMEA) in order to achieve the desired resist thickness ranging from 60 nm to 100 nm depending on the stamp pattern. Other structures, such as hexagonal pillar and hole structures with a 300 nm diameter, were used as well. The process with the T-NIL was optimized at a low temperature (83°C) so that to avoid other issues, such as lack of adhesion, capillary effects or dewetting, since DLC and SiPol alone are only exhibiting moderate adhesion. The low imprint temperature is an additional advantage of SiPol because the extended heating of hydrogenated DLC films may cause changes in the dimensions and properties of the material. Additionally, the lower imprint temperature of SiPol (83 ºC) instead of PMMA (180 ºC) is beneficial as it significantly reduces the tendency of the material to develop capillary bridges.

Imprints with 2–5 min long thermocycles with an applied pressure of 1.5×10^6 Pa were found to be sufficient enough for the resist to homogeneously fill the stamp cavities for the proper and effective pattern transfer. After cooling down to a temperature of 20°C below the T_g of the polymeric resist material, the stamp is separated from the substrate with the patterned resist layer. The low-temperature incomplete filling approach not only allowed a virtually zero residual layer imprint but also facilitated the original SiPol process involving an organic transfer layer by removing the intermediate etchings and thus enabling pattern transfer with a single etching step.

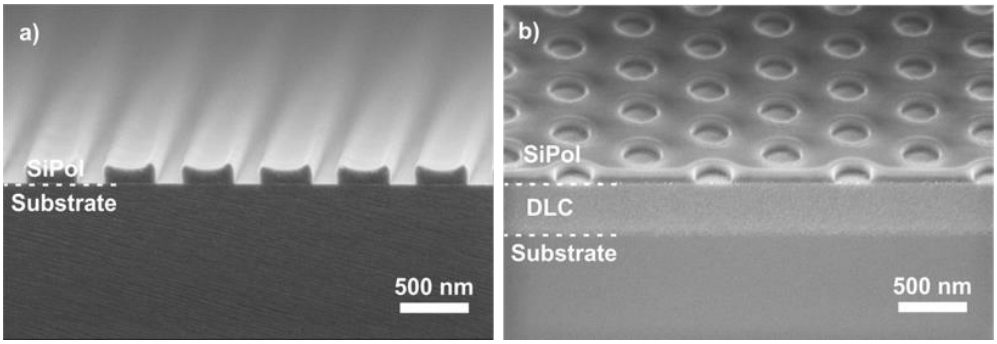

Figure 4.4. Patterning of SiPol with incomplete filling strategy: a) imprinted 580 nm period grating; b) imprinted 300nm diameter holes ordered in a hexagonal array.

Structures imprinted into SiPol are presented in Figure 4.4. For the linear gratings, the 70 nm high resist was equally distributed within the cavities and showed only a low tendency to form capillary bridges (due to the prominent cavity height, the small lateral dimension and the low imprint temperature versus the T_g). The small rims at the sides of up to ~20 nm are caused by the wetting of the sidewalls; they do not interfere with the pronounced anisotropic etching (this might even reduce the rounding of the resist edge during etching). At the same time, almost zero residual layer thickness was achieved due to the high capacity of the SiPol material to flow (Fig. 4.4a). Although complete dewetting down to 0 nm seems possible, the actual remaining thickness is difficult to determine. However, even if a few nanometers remain, the following etching step (in O_2-plasma) will serve as an effective descum (window opening) step before the DLC is etched. In this case, the remaining residual layer can be considered as effectively equal to zero. The same imprint quality with the dewetting effect is also observed in other type patterns, e.g., circular holes with a diameter of 300 nm ordered in a hexagonal array (Fig. 4.4b). Small rims around the holes due to the wetting of the sidewalls are also visible. The maximum fill rate of the stamp cavities for the linear grating patterns until delamination of SiPol from the underlying DLC substrate starts to occur was found to be at an aspect ratio of ~0.7. For patterns of lower density, e.g., holes where a much larger area of the resist is in contact with the substrate than with the stamp, this is less of an issue, and the ratio could be higher [168].

4.1.3 Pure DLC Etching with Different Patterns

The imprinted SiPol resist exhibiting a negligible residual layer was directly used as a mask for the pattern transfer into DLC thus avoiding the usual window opening with fluorine-based plasma. Hence, the direct etching of DLC with pure oxygen plasma can be performed immediately after imprint.

The etching of SiPol itself is a complex process which has two goals: the thinning down of the organic-inorganic polymer until the windows are opened and the conversion of the remaining polymer into almost pure SiO_2 by removing the organic content. In the ideal case, this results in a thin homogeneous layer of SiO_2 which would not be susceptible to heat in the extended etching process. Since a virtually zero residual layer has been achieved during the patterning step, a pure oxygen etching step was found to be sufficient to achieve the removal of any resist residues, but this process would not convert SiPol into SiO_2 completely as for the standard SiPol thinning process. Once the upper few nanometers of SiPol are converted, it would not further etch and develop into a thin skin on the still intact SiPol. The thermoplastic properties of this core would then be susceptible to any heat treatment, which in case of oxygen plasma was found sufficient to develop the resist lines into thermally reflowed cylinder structures (as seen in Fig. 4.1a). The reflow would be enhanced if undercuts developed, which would further pull the skin into a rounded shape (see Fig. 4.1b). This effect is greatly pronounced when SiPol is used in a bilayer system with a purely organic material, e.g., UL1. The possibility to create such undercuts may be advantageous for certain applications. However, this behavior is greatly diminished when SiPol is used directly on DLC. High etch rates prevent SiO_2 skin formation by the constant formation–erosion cycle during the etching, and the mask thins down rather gradually. When etched by pure oxygen, the organic content is removed at the surface, and SiPol converts into silicon oxide which possesses a high etch resistance.

As for the etching of DLC, the process is fairly straightforward. The exposed DLC surface is chemically etched by reactive oxygen species creating volatile products in combination with the physical etching caused by ion bombardment. In order to achieve high etch rates and smoothly etched surfaces, a high plasma density, a reasonably high bias and a low pressure for strongly directional ion bombardment of the sample are required. For these reasons, the etchings were done with the ICP (RIE100 from Oxford Instruments) system. The optimal etching parameters were determined to result in highly directional sidewalls and a smooth surface of the etched DLC structures. The slightly modified method was also applied for the DLC:Ag nanocomposite containing 8 at.% of Ag patterning. It is described in more detail in Chapter 4.2.2. The etch rates of both DLC and DLC:Ag against SiPol are presented in Figure 4.5. Furthermore, these etch rates are compared to the rates of a commonly used resist, such as PMMA, to further validate them. After completing the etching, the remaining residues of SiPol were removed in CHF_3/CF_4 plasma followed by rinsing with acetone and isopropanol. The etching recipes for the different materials involved in the processing are presented in Table 4.1.

The etching parameters for DLC were optimized to achieve a highly directional

transfer. From the etching rates depicted in Figure 4.5, the selectivity between SiPol and DLC was determined to be at least 1:4. When compared with purely polymeric resists, e.g., PMMA, it is up to 20 times higher. The linear gratings and hexagonal structures (both holes and pillars) were successfully transferred into DLC. Figure 4.6 a–b shows a 400 nm period of 140 nm depth and a 380 nm period of 300 nm depth gratings etched into DLC. In Fig. 4.6c, the 380 nm depth holes in DLC are not yet deep enough to etch through the entire 450 nm thick film. At the same time, SiPol has not yet been completely removed (an estimated thickness 10–20 nm). It shows (in the area between the holes) a visible undulation which develops, as in the case of the linear gratings, due to the fact that SiPol wets the stamp pillars. This is due to the capillary effects (the electro-hydrodynamic effect) and therefore shows some shallow voids and lateral displacement of the material. The achieved thickness contrast shows that, even in this special case, no capillary bridges could form and that the surface undulations presenting the onset of the capillary action were far from causing problems in etching.

Table 4.1. Optimal etch parameters.

Etch step	DLC	DLC:Ag	SiPol removal
Gas (sccm)	10 O_2	10 O_2, 10 Ar	10 CHF_3, 10 CF_4
Power ICP (W)	1000	1000	900
Power bias (W)	80	80	30
Presure (mTorr)	11	11	11

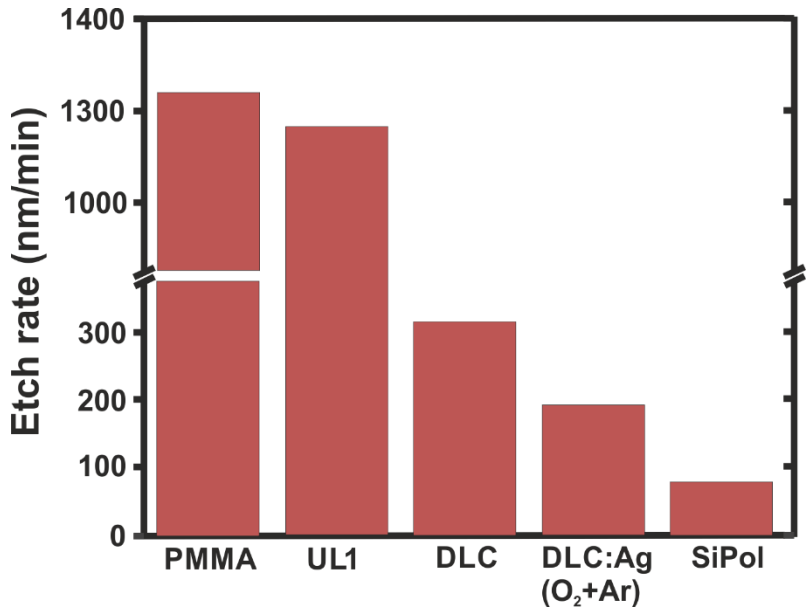

Figure 4.5. Etching rates in the oxygen plasma at the optimized parameters for DLC etching.

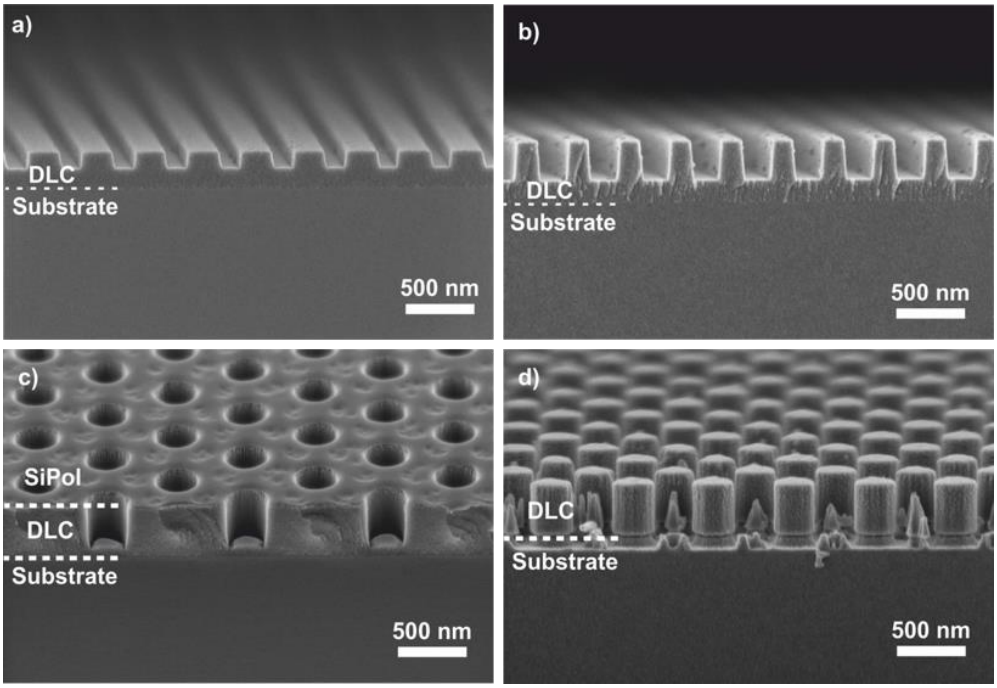

Figure 4.6. Patterning DLC: a) 400 nm period 140 nm depth grating etched into DLC; b) 380 nm period 300 nm depth grating etched into DLC; c) a hexagonal hole pattern (300 nm diameter, 380 nm depth) etched into DLC; d) a hexagonal pillars pattern (300 nm diameter, 400 nm depth) etched into DLC and the substrate.

The pillars in the DLC shown in Figure 4.6d are completely etched, i.e., the 400 nm thick film was etched down to the silicon substrate, and SiPol was removed by the additional CHF_3/CF_4 step [168]. In this case, the silicon substrate was also etched by the fluorine species proving the use of DLC as an etching mask with a high selectivity towards silicon and silicon oxide [173]. In fact, the developed process could be utilized to pattern silicon in a very efficient way by using T-NIL together with bilayer SiPol-DLC as the etching mask.

4.2 Processing of DLC:Ag Nanocomposite Films

4.2.1 Analysis of the Deposited DLC:Ag Films

DLC:Ag films were deposited by employing unbalanced reactive magnetron sputtering of a silver target with Ar^+ ions in C_2H_2 gas atmosphere (see Chapter 3.1). By varying the deposition conditions, films with a different silver content (0.6–12.9 at.%) were fabricated and analyzed. A summary of the sample dependent deposition conditions is presented in Table 4.2. The resulting thickness of the deposited films was calculated according to the microbalance indications and by taking into account the chemical composition of the deposited film which was determined by employing EDS analysis. The thickness of the films varied in 181–266 nm range.

Table 4.2. Deposition conditions of DLC:Ag films.

Sample	Ar gas flux (sccm)	C_2H_2 gas flux (sccm)	Ar/C_2H_2 flux ratio (%)	Magnetron target current (A)	Voltage (V)	Deposition time (mm:ss)
No. 1	70	21.1	30	0.07–0.12	553–625	8:40
No. 2	70	21.1	30	0.08–0.17	553–625	4:40
No. 3	70	21.1	30	0.07–0.22	568–741	3:55
No. 4	80	7.8	10	0.10–0.11	625–656	3:20

The chemical composition of the deposited films on silicon was determined from the EDS measurements. By taking into account the small thicknesses of the films and the relatively low fluorescence energies of the carbon Kα (0.277 keV) and silver Lα Lβ (2.984–3.519 keV) lines, low accelerating voltages (5 kV) were employed in the measurements in order to suppress the Bremstrahlung background and the interaction volume reaching the substrate, i.e., silicon Kα and Kβ (1.740–1.840 keV) lines. The obtained chemical composition and EDS spectra are depicted in Table 4.3 and Figure 4.7.

Table 4.3. Normalized chemical composition of the films (samples No. 1–4) excluding the influence of the silicon substrate obtained from the EDS measurements.

Sample	Concentration (at.%)			Ag/C ratio	Calculated thickness (nm)
	C	Ag	O		
No. 1	92.4	0.6	6.9	0.0065	266
No. 2	88.6	2.1	9.3	0.0237	253
No. 3	84.3	5.8	9.9	0.0688	222
No. 4	75.2	12.9	11.9	0.1715	181

The results of the EDS measurements indicate that the chemical composition of the films is in good agreement with the previous results [174]. This fact demonstrates that the employed deposition system and the selected mode of deposition (the constant mass rate) assure reproducible coating composition, and DLC:Ag nanocomposite thin films with a variable content of silver can be produced. From the EDS spectra (Fig. 4.7), one can see that the intensity of X-ray fluorescence *L* line of silver increases with the increase of the filler concentration, whereas the intensity of carbon *K* line decreases with the decrease of the carbon content, i.e., the matrix of the nanocomposite film.

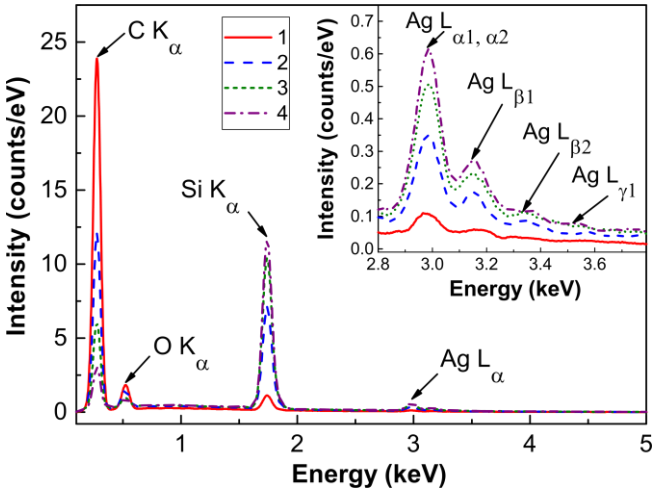

Figure 4.7. EDS spectra of the samples No. 1–4 (see Table 4.3) obtained with the accelerating voltage of 5 keV. The arrows indicate X-Ray emission lines. The inset depicts a 1 keV interval (2.8–3.8 keV) representing Ag *L* lines.

The structure of the carbon matrix was also determined with FTIR spectroscopy. The variation of the characteristic C–H stretching region is presented in Figure 4.8. Analysis of the films with FTIR spectroscopy revealed that with the increase of the silver concentration in the films, the intensity of the characteristic C–H stretching region decreases dramatically. This result is consistent with the chemical composition data (Table 4.3) showing the decrease of the carbon-related peak with the increase of the silver concentration. The C–H stretching region was deconvoluted into separate bands corresponding to sp^3 and sp^2 carbon hybridizations.

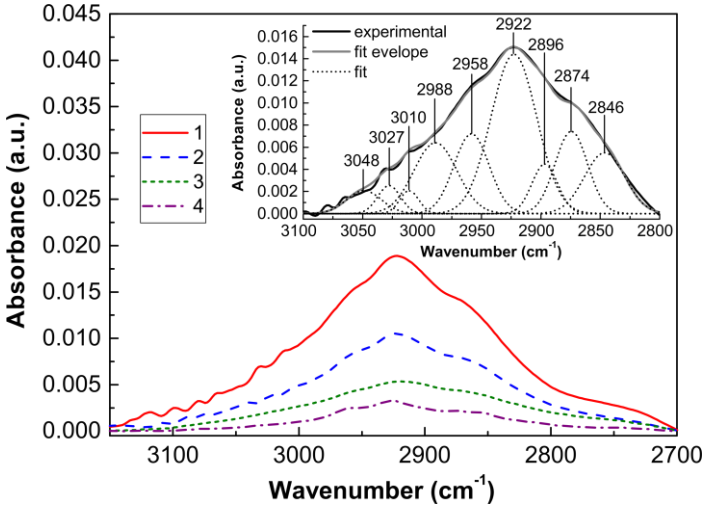

Figure 4.8. FTIR spectra of the C–H stretching region corresponding to the amorphous carbon matrix of DLC:Ag films with a different Ag concentration (samples No. 1–4). The inset depicts the deconvolution of the IR spectrum in the C–H stretching region for the film with 0.6 at.% of Ag (No. 1) showing the peaks corresponding to sp^3 and sp^2 related bonding.

Bands from 2800 cm^{-1} up to 2960 cm^{-1} correspond to sp^3 bonded carbon and bands at higher wavenumbers stand for carbon atoms bonded in sp^2 configuration [76]. The inset shows that a higher fraction of carbon atoms in films are bonded in the sp^3 configuration. By taking in mind the areas of the approximating peaks, the sp^3/sp^2 ratio was determined. A decrease of the sp^3/sp^2 ratio from 3 to 2.3 with an increase of silver concentration was observed. The importance of the matrix on the final properties of the nanocomposite thin film was already demonstrated in [174] by considering the piezoresistive properties of DLC:Ag thin films. The results of the present research are in line with earlier observations, i.e., an increase in the silver content in DLC results in favor of sp^2 bonding against sp^3 [175].

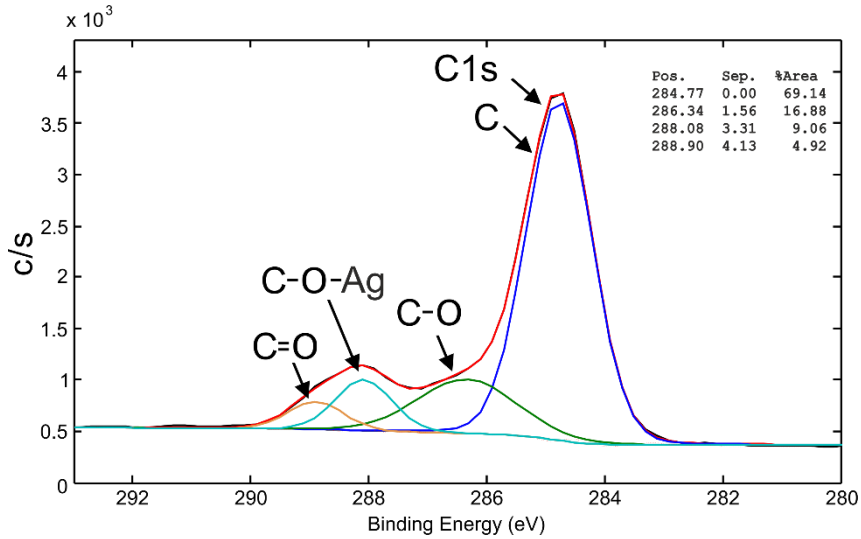

Figure. 4.9. XPS spectra of Sample No. 3 showing fitted carbon C1s spectra with the separate peaks corresponding to different type bondings of carbon atoms in the fabricated films.

The surface chemical composition and bonding of DLC:Ag films was determined by XPS analysis. XPS survey was able to detect the characteristic peaks associated with carbon, silver and oxygen. All the samples featured a similar composition with a slight variation of the silver concentration, which correlates to the elemental composition results provided by EDS analysis. The oxygen presence is due to the exposure to the air atmosphere after film deposition. In order to determine the chemical state of the fabricated films, the characteristic peaks for the elements of interest, namely, carbon and silver, were investigated in more detail. High resolution carbon C1s transition spectra of No. 3 film is presented in Figure 4.9 together with the corresponding peak fits. The major peak at 284.77 eV energy corresponds to C–C type bonds. It represents approx. 70% of all the carbon atomic bonds suggesting that the carbon atoms in the fabricated films are mostly bonded together. The value of C1s spectra lies in between the peaks associated with sp^3 (285.2 eV) and sp^2 (284.4 eV) bonded carbon [176]. The full width at half maximum of this peak was measured to be within the range of 1.3–1.6 eV. It is a bit broader than those typical for diamond

and graphite (1.4 and 1.3 eV, respectively) [177]. This supports the notion that a mixture of sp^3 and sp^2 type carbon bonding is present in the films. The other two distinguished peaks are observed at 286.34 eV and 288.90 eV energies. They are associated with C–O and C=O type bonds and correspond to approx. 17% and 5% of the carbon bonds. One more peak is observed at 288.08 eV energy level and is hard to identify. No matches were found in the available XPS databases. However, it also shows up in the peaks corresponding to silver and oxygen. For that reason, an assumption can be made that it is due to C–Ag or C–Ag–O type bonding. This type of bonds constitutes approx. 9% of all the carbon chemical connections. Figure 4.10 shows the spectra of two silver (Ag3d3 and Ag3d5) peaks of the same sample. For each of them, three distinguished peaks can be recognized. The peaks at 368.30 eV and 374.30 eV energies represent Ag–Ag type atomic bonding. It corresponds to approx. 70% of all the silver atomic bonds. This means that the silver in the produced films is mostly in the metallic form. The peaks at 367.81 eV and 373.81 eV energies represent the AgO_2 type bonds. The peaks at 368.76 eV and 374.76 eV energies can be associated with the C–Ag–O type bonds by analogy observed in C1s spectra.

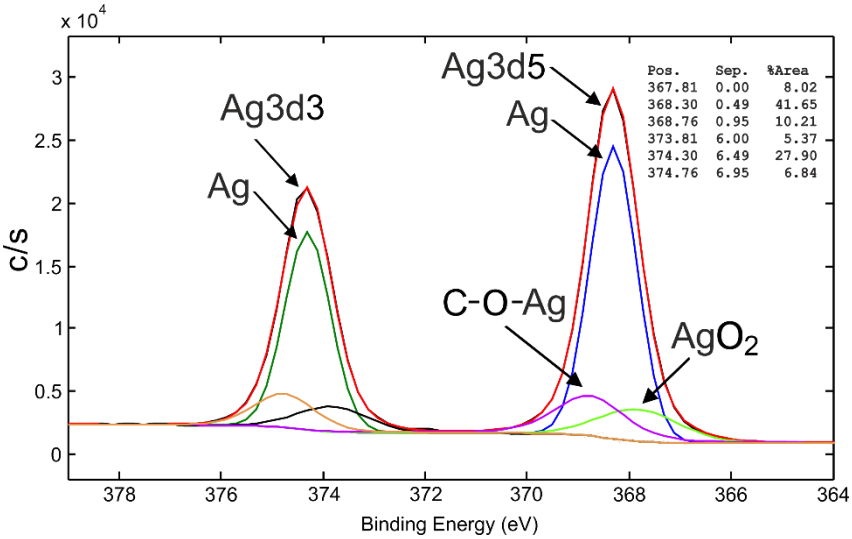

Figure 4.10. XPS spectra of Sample No. 3 showing fitted silver C1s spectra with the separate peaks corresponding to different type bonding of carbon atoms in the fabricated films

4.2.2 Analysis of Plasma Structured DLC:Ag Films

DLC:Ag nanocomposite thin films of a different Ag concentration (see Table 4.2) were structured by CF_4/O_2 plasma chemical etching (PCE). The impact that such processing exerts on the film surface morphology was analyzed by using SEM, and its effects on optical properties were assessed by using UV-VIS-NIR spectroscopy. SEM micrographs of the film surface after deposition (noted ‘As deposited’) and a different PCE processing duration (noted as ‘2 min’, ‘4 min’ and ‘6 min’) are presented in Figure 4.11. The deposited films had a rather smooth surface with no

visible silver filler exposure. PCE processing by CF_4/O_2 plasma during which only carbon is selectively removed was pursued. After the initial 2 minutes' duration etching cycle silver NPs which were embedded in the carbon matrix during the deposition process became visible in all cases. Particle distribution across the large surface area was even, and the average particle size increased according to the silver filler content.

After extended PCE processing, the samples demonstrated different behavior depending on the silver content in the film. The films with the lowest silver content (samples No. 1–2) demonstrated only minimal changes of the silver cluster size after different processing durations. The samples containing more than 5 at.% of silver (No. 3–4) demonstrated well-expressed sintering. Extended PCE processing induced silver particle coarsening, whereby particles increased in size and reduced in number. Coalescence and Ostwald ripening are the two main mechanisms which can cause such a behavior. Coalescence occurs when two or more particles touch and merge to form one bigger particle, while Ostwald ripening occurs via redeposition of dissolved species. The latter process is the usual form of sintering for metal clusters on a supported surface which are well-spaced apart, although coalescence can occur in case of the high density of particles [178].

Nanocomposites under thermal treatment tend to exhibit Ostwald ripening where dissolution of small crystal particles and the redeposition of dissolved species on the surfaces of the larger crystal particles is observed. As a result, with the progress of time, larger particles grow in size at the expense of the finer ones. The process occurs because smaller particles have a higher surface energy; hence, they possess a higher total Gibbs energy than the larger particles, giving rise to an apparent higher solubility [179]. In general, the presence of the surface results in a surface-mediated Ostwald ripening, in which the material is transferred from one particle to another by diffusion across the surface and not through the gas phase [178]. As it can be seen from Fig. 4.11., Ostwald ripening can be induced by plasma treatment as well, and it is mostly expressed for Sample No. 4, i.e. for the sample with the highest silver content (12.9 at.%). After long (6 min) PCE processing, all the silver particles agglomerated into large 190 nm average diameter spherical clusters forming silver rich and silver depleted zones on the surface. A similar behavior of noble metal films on crystalline substrates, on thin DLC films, or in a glass matrix, has already been observed after Xe lamp irradiation [180], annealing at 200–400ºC in vacuum or in muffle furnace [181–184], femtosecond irradiation and afterwards annealing at 350–650 ºC [185], after processing in O_2:Ar plasma [186, 187], cold plasma [188], or after etching in hydrogen plasma [189]. Ostwald ripening, which can be used to control the size distribution of nanoparticles [179, 180, 184, 190, 191], seems to be a process responsible for the plasma induced changes of the nanocomposite surface [175].

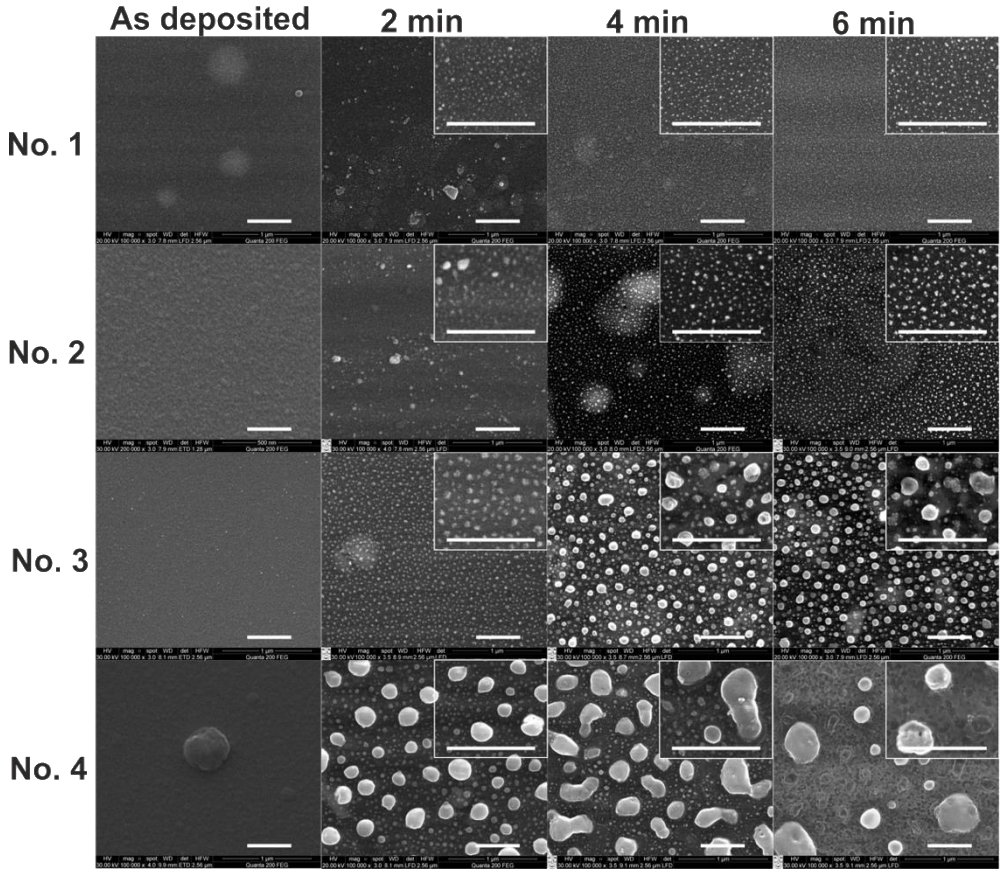

Figure 4.11. An array of SEM micrographs of different silver content films (samples No. 1–4, with the concentration of Ag ranging from 0.6 to 12.9 at.%) after different processing durations. The PCE processing duration increases from left to right, and the silver content increases from top to bottom. The insets represent cropped micrographs of 200×k magnification. The length of the scale bar in all pictures is 500 nm.

In order to closer investigate the filler coarsening process in nanocomposites, SEM micrographs presented in Figure 4.11 were used for the determination of the Ag NP size distributions in DLC:Ag thin films processed with plasma over different time spans. ImageJ software was used to distinguish particles in the micrographs and to estimate their size. The projected area diameter (dA) which is defined as the diameter of the sphere having the same projected area as the particle was used to describe the particle size distribution. The projected area diameter (dA) can be related to the projected area (A) by $dA=(4A/\pi)^{1/2}$.

Particle size variations resulting from growth processes can often be assumed to be log-normally distributed [190]. Log-normal distribution represents the statistical realization of the maximum entropy state of the variable whose values can only be positive, and the variability is based on the multiplicative effect (rather than on the additive effect, which is the case in the Gaussian distribution) of many factors acting independently [192].

Since the particle size cannot be negative and as most physical (chemical) interactions governing nucleation and growth are denoted by multiplicative relationship between process parameters, and also by considering the fact that many physical systems tend to move towards the maximal entropy configuration over time, altogether leads to skewed size variation which closely resembles log-normal distribution and is often encountered in NP synthesis [190, 193, 194].

The log-normal distributions probability density function has the following expression:

$$p(x,u,\sigma) = \frac{1}{x\sigma\sqrt{2\pi}} e^{-\frac{(\ln x-\mu)^2}{2\sigma^2}} \quad (4.1)$$

where x is the variable, μ represents the shape parameter, and σ stands for the scale parameters defined as the mean and standard deviation of the variable $y=ln(x)$.

Such statistical parameters as the mean and standard deviation of the NPs diameter were calculated from the obtained experimental particle size distributions. These parameters were used to calculate the log-normal distributions density function parameters used to fit the experimental data. The obtained experimental particle size distributions together with the log-normal fit depending on the PCE processing duration of all samples (No.1–4) are depicted in Figure 4.12. The mean particle sizes with the standard deviation for all analyzed samples together with log-normal distribution parameters and the particle count in the investigated 5.5 μm^2 area after different PCE processing durations are summarized in Table 4.4.

As it can be seen from the obtained particle size distributions, low silver volume fraction samples (No. 1 and No. 2) showed narrow particle size dispersity, and the log-normal distribution fitted the data well in all different duration processing cases. In these samples, the average size of the particles showed tendency to slightly increase with the widening of the distribution in all the following cycles except for the first 2 minutes PCE processing cycle, when the average particle size was larger than it was supposed to be considering the dynamics of Ostwald ripening. The deviation from the expected particle distribution values after the first 2 min of PCE processing in the samples (No. 1 and No. 2) can be explained by the limited capacity of the SEM to identify the smallest particles. The silver content in these nanocomposite films is small; therefore, after the first processing cycle, only the coarsest particles are exposed to the surface thus giving the false view on the overall size distribution. Micrographs and the amount of particles identified on the surface support this assumption as sparse and uneven dispersion is observed with a prominently lower number of exposed particles than in following cycles, e.g., sample No. 2 after 2 minutes of PCE processing only had 178 identifiable particles. After 4 minutes of PCE processing, much finer particles were exposed in both samples. Further processing promotes implicit coarsening which is hard to observe visually but can be derived from the slightly increasing average particle size and the standard deviation values with the reduced number of particles (see Table 4.4). Thus Ostwald ripening in these samples is only mildly pronounced since narrow particle size distributions are less susceptible to coarsening.

Particles in Sample No. 3 throughout all different duration processing cycles showed the tendency to increase the size with the widening of the distribution and the decreasing amount of particles. The amount of particles decreased with the gradual disappearance at the finer end of the particle size distribution and the gain at the coarse end. This is exactly the type of behavior which would be expected in an act of Ostwald ripening. Log-normal distribution still fitted data well although a slight excess after 4 min and 6 min processing in a larger (60–100nm) particle area started to appear.

The sample with the highest silver volume fraction (No. 4) after the initial 2 minutes of PCE processing already showed a large amount of widely dispersed particles with the particle distribution closely resembling log-normal distribution. After 4 minutes of processing, a noticeable size increase of the coarsest particles was observed. Micrographs revealed that, in this case, coalescence was the driving process, since particles demonstrated elongated shapes which would be expected in the contact-based nature of merger. The mean particle diameter in this case decreased. However, this yields a false picture. As coarse particles coalesce, their number decreases while a large fraction of the small particles still remains. This results in extremely dispersed (as it can be seen from the large standard deviation value) particle size distribution which deviates from log-normal distribution with excess in the large (150–300 nm) particle area. Similar binomial distributions were also observed during Ostwald ripening-induced particle coarsening in destabilized colloidal solutions [195] or in nanocomposite thin films [196]. Eventually, after 6 min processing, fine particles totally evaporated due to Ostwald ripening, and only a few large particles of random sizes were observed on the surface.

Table 4.4. Mean particle size of samples No. 1–4 with standard deviation (s.d.) and log-normal distribution parameters after different PCE processing durations (2–6 min).

Sample	Parameter	Parameter value after different duration of PCE treatment		
		2 min	4 min	6 min
No. 1	diameter ±s.d. (nm)	12.2±7.4	10.4±1.8	11.1±2.2
	μ	2.419	2.331	2.389
	σ	0.359	0.305	0.187
	number of particles	1402	3616	3384
No. 2	diameter ±s.d. (nm)	26.2±12.7	13.4±4.1	14.5±4.7
	μ	3.189	2.551	2.628
	σ	0.355	0.287	0.314
	number of particles	178	2826	2418
No. 3	diameter ±s.d. (nm)	14.2±4.6	25.6±19.1	30.5±24
	μ	2.600	3.036	3.154
	σ	0.315	0.619	0.710
	number of particles	1824	1646	938
No. 4	diameter±s.d. (nm)	29.6±33.4	27.4±52.0	189.8±113.0
	μ	3.010	2.751	-
	σ	0.682	0.785	-
	number of particles	800	346	13

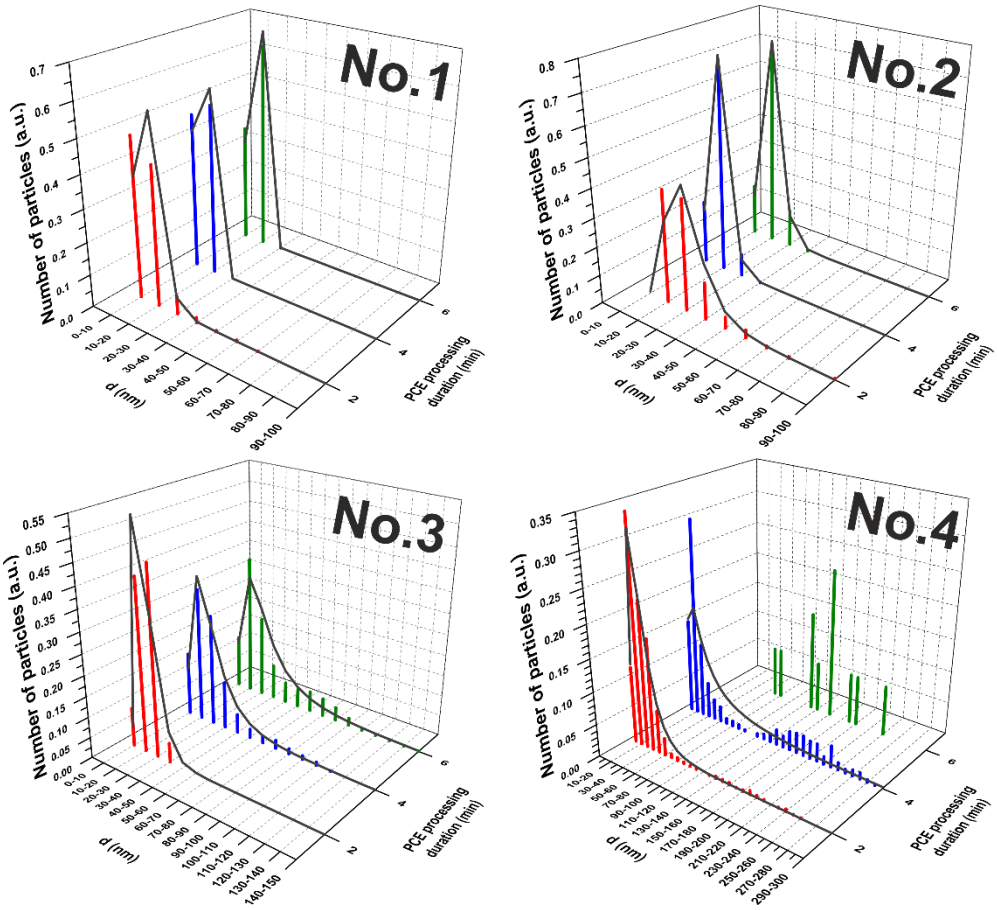

Fig. 4.12. Normalized particle size distribution histogram together with approximating log-normal distribution fit after different PCE processing durations (2–6 min) of samples No. 1–4 obtained from 100× k magnification of SEM micrographs.

The absorption coefficient of the deposited thin films and the absorbance of the etched films (as a typical example, Sample No. 2 after different time durations of PCE) in the visible region is presented in Figure 4.13. The absorption coefficient of the films in the visible range depends on the amount and size of the incorporated silver particles. The amplitude of the peak in the optical absorbance spectra of the as-deposited samples follows the silver content and is well expressed only for Samples No. 3 and No. 4 (silver concentration 5.8 at.% and 12.9 at.%, respectively). In the case of the lowest silver concentration (0.6 at.%), the characteristic surface plasmon resonance peak is not pronounced. It could be explained by the small particle size and the sparse distribution in the film (as it is shown in Fig. 4.11) [197]. The decrease in the plasmonic absorption amplitude with the increased processing duration is the consequence of the exposed particle oxidation which induces the damping of the plasmonic response. The increasing processing duration also increases the fraction of the exposed particles which are prone to oxidation. According to the obtained results,

a combination of tailored film deposition together with a selective PCE of the DLC matrix at room temperature enables to produce surfaces with controllable composition and tunable optical properties. The employment of etching through the mask may allow to produce periodic structures [175].

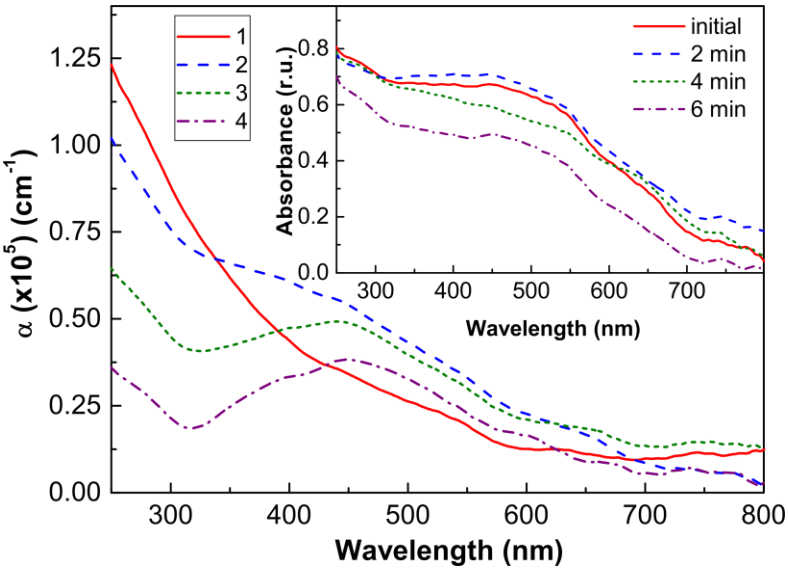

Figure 4.13. Absorption coefficient of the DLC films with different Ag concentration (samples No. 1–4). The inset shows the variation of absorbance of Sample No. 2 after the application of PCE processing (2–6 min).

The T-NIL patterning method employing an imprintable hard mask used to structure DLC films was also applied for the DLC:Ag nanocomposite containing 8 at.% of Ag. However, etching with pure oxygen plasma was not sufficient due to the presence of silver nanoparticles scattered all over the surface and in the bulk. In this case, during O_2 RIE, the carbon matrix was effectively etched, yet the exposed Ag particles started acting as a hard mask preventing the etching of the underlying film. In order to overcome this issue, combined O_2 and Ar plasma was used, which resulted in more efficient etching of the nanocomposite material. Argon also contributed to the faster erosion of the SiPol mask resulting in a lower selectivity of 1:2.5 towards DLC:Ag. Although the selectivity of the mask with respect to the composite material was slightly reduced, it was still sufficiently large to allow the patterning. The residues of SiPol on the surface were removed as in the case of pure DLC. This process was employed in order to structure DLC:Ag films with a 400 nm period and approximately 150 nm depth (the precise depth is hard to determine due to the roughness of the etched profile) grating patterns (see Fig. 4.14a) leaving a high concentration of silver nanoparticles on the surface (see Fig. 4.14b) [168]. Such patterning allows to impose some artificial patterns on the nanocomposite surface simultaneously exposing embedded Ag particles. However, the resulting structures showcase high roughness and irregularities since excessive particles are not effectively ‘descumed’. Ar ion-milling-based process in this case may yield better results.

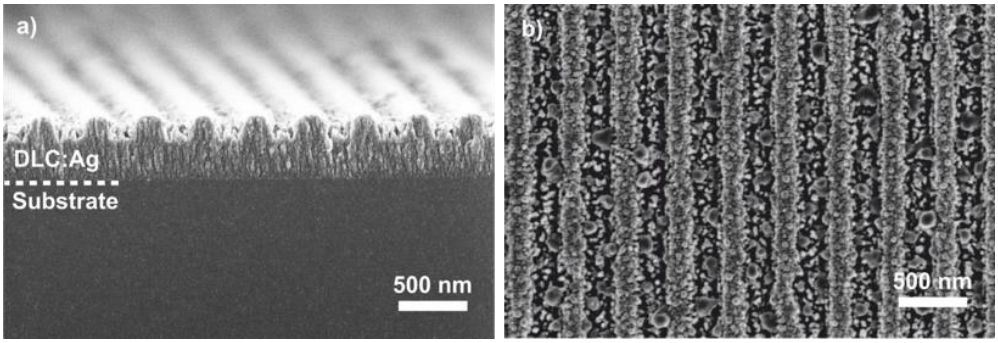

Figure 4.14. SEM micrographs depicting 400nm period and ~150nm depth gratings fabricated in DLC:Ag nanocomposite as seen a) from the side; b) from the top.

4.3 Optical Characterization of DLC Based Optical Sensors

While using the fabrication method described above, 380–400 nm period grating type structures were fabricated in DLC, and their optical response was characterized. The gratings were fabricated on 20x20 mm^2 Borofloat glass chips with the patterned area of 180 mm^2. This size was selected in order to fit the sensor chip in the measurement cell so that the reflectance spectra could be obtained with the custom setup. Borofloat glass was chosen as a substrate because, as a transparent material, it is suitable for optical measurements of the GMR signal from DLC gratings in the reflectance mode from the back (substrate) side of the chip. An additional advantage of the Borofloat glass is that its thermal expansion coefficient is similar to that of silicon, which helps to minimize the pattern displacement and distortion effects which may arise due to different expansions between the template and the substrate during embossing. The optical response of such chips in the reflectance mode was observed and characterized by using the custom setup which is described in more detail in Section 3.7.1. Numerical simulations of the polarized white light reflection spectrum from the DLC and DLC:Ag gratings were done by using the GSolver software package (see Section 3.7.2). For simulations, grating geometry and material optical properties (refractive index and extinction coefficient dispersity) had to be defined. The obtained dispersity curves for both DLC and DLC:Ag are presented in Figure 4.15a. The exact relief geometry (the period, the height, the waveguide thickness and the filling factor) of the fabricated structures was determined from high resolution SEM micrographs of the test samples processed under the same conditions, only being made on silicon substrates (as seen in Fig. 4.15b for DLC grating and in Fig 4.14 for DLC:Ag). In simulations, the gratings were approximated by a finite number of slabs to the closest ideally rectangular profile which would resemble the fabricated one.

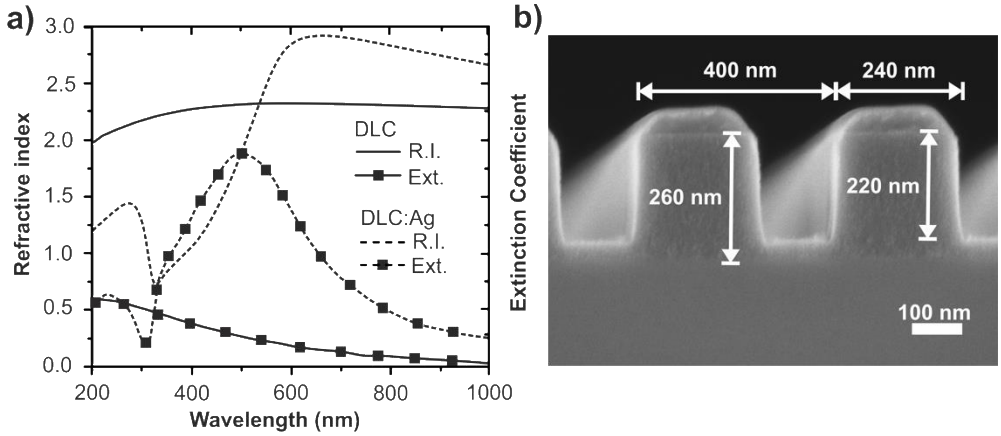

Figure 4.15. a) Refractive index (R.I.) and extinction coefficient (Ext.) dispersion curves of DLC and DLC:Ag films (the scale is equal for both variables). b) A high resolution SEM micrograph depicting the structural dimensions of the DLC grating.

The reflectance spectra recorded at the different angles of incidence (AOI) in the *transverse–electric* (TM) mode together with the numerical simulations of the DLC grating are presented in Figure 4.16. Two peaks can be observed in the spectrum which, as the angle of the incident light increases, shift away from each other. The first peak shifts towards the shorter wavelengths, whereas the second one shifts towards the longer wavelengths. Such a behavior is common in GMR structures [198]; it indicates that the resonance is actually obtained in the produced DLC gratings. The simulations and the observed response are in reasonably good agreement. However, slight deviations can be spotted. The lesser than in simulations signal intensity is most likely caused by scattering from the grating surface which has some roughness as well as reflections as light passes through several optical elements during the measurements. Deviations in the shape of the spectral response are presumably caused by the grating geometry variation. The best qualitative match between the simulated and the observed response was found to be for the grating with the 400 nm period, 210 nm height, 60 nm waveguide thickness and 0.6 filling factor (see Fig. 4.17a). This only slightly differs from the geometry obtained from SEM micrographs (see Fig. 4.15b). The test sample as well as the sample investigated with SEM were fabricated in the same batch; however, due to ion flux variations at different sample holder locations during the film deposition process, small differences in the grown film thickness can be expected. The 10 nm difference in the depth of the grating is also reasonable for the etching process. It is worth pointing out that the GSolver based simulations demonstrated a much better correlation with the experimental results; they enable a prediction of not only the position of the peaks but also the overall shape of the spectral response more accurately than the recent attempts to numerically investigate similar DLC GMR structures while employing other methods [99, 198].

Simulations also suggest that the sharpest peaks in the reflectance spectrum for a given period (400 nm) grating in the air surrounding (n =1) would be achieved if the grating's height were 100 nm, the waveguide thickness equaled 40 nm, and filling

factor stood at 0.55 (see Fig. 4.17b). However, this is not the case when the refractive index of the surrounding medium is in the 1.3–1.4 range. Then, the geometry pictured in Fig. 4.15b yields sharper peaks.

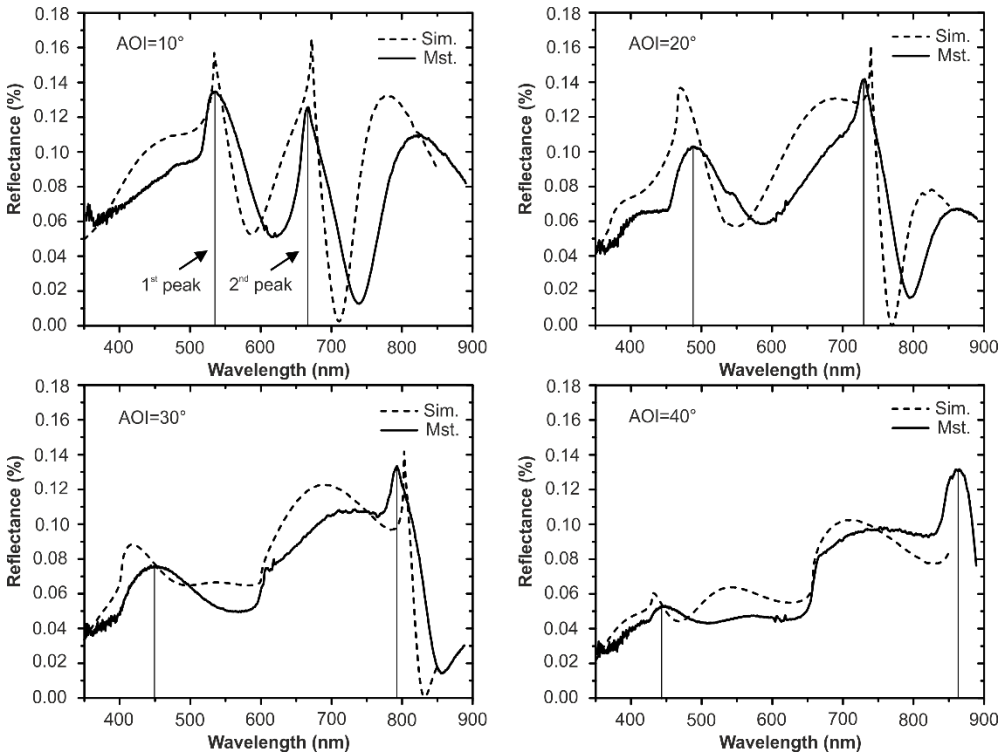

Figure 4.16. Simulated (Sim.) and measured (Mst.) reflectance spectra of 400 nm period and 220 nm depth with 40 nm waveguide layer grating fabricated in DLC. Recorded for TM polarization at the different angles of incidence (AOI) in air surrounding to show the GMR peak shift.

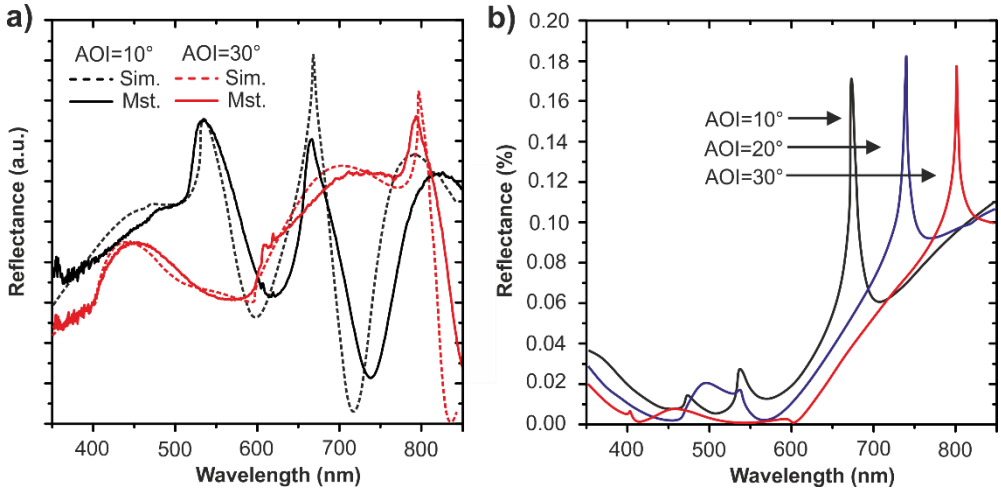

Figure 4.17. a) Spectra showing the best qualitative match between the observed (Mst.) and the simulated (Sim.) response which is observed for grating with a 400 nm period and a 210 nm depth with a 60 nm waveguide layer. b) A simulated spectral response of the grating geometry providing the sharpest GMR peaks at different angles of incidence (AOI) in the air surrounding.

The grating fabricated in a DLC:Ag composite film was also evaluated in the same way. Due to the exposed silver nanoparticles on the surface, such gratings have the potential to be utilized as sensing devices enabling simultaneous guided-mode and plasmonic resonances as proposed in [199]. The simulated and measured optical response of the DLC:Ag grating is presented in Figure 4.18. In this case, the mismatch between simulations and observations is severe. In the measured spectra, GMR peaks are heavily distorted and barely distinguishable. For the longer wavelengths (>700nm), there is some qualitative similarity between the two; however, at the shorter wavelengths (<700nm), the signal is totally cut off with the observed reflectance intensity almost reaching zero. The cause of this might be a combination of scattering effects by a very high surface roughness as well as broadband plasmonic absorption (see Fig. 4.13) in the given part of the spectrum by exposed Ag NPs, for which, the software in use does not account (it is designed to be used for dielectric materials), and therefore cannot be used to reliably predict the spectral response.

This study implies that, although plasma post-processing enables to produce surfaces with a controllable amount and size distribution of Ag NPs, imposing a reliable patterning remains a challenging task due to the complexity of the nanocomposite material. Thus continued development efforts are required in order to achieve the utilization of DLC:Ag based structures in functional devices.

In order to evaluate the sensitivity to the changes in the refractive index in the vicinity of the fabricated DLC grating, different concentration (according to mass) *isopropanol* (IPA) solutions in DI water (0–100%) were used as the analyte. The refractive index of the different solutions (ranging from 1.330 for pure DI water to 1.375 for pure IPA) was determined by using an Abbe refractometer (Carl Zeiss). The analyte was filled into the measurement cell with the DLC sensor chip in order to

determine the optical response. All the experiments were carried out at 23°C temperature and 20% relative humidity. The measured spectra were normalized to the lamp spectrum by taking into account different polarizations and integration times. The spectrum was collected at an angle of incidence of 20°. As it can be seen in the reflectance spectra presented in Figure 4.19, there is a clear resonant peak at 669 nm which red shifts towards the longer wavelengths; as the IPA concentration in the analyte increases and so does the refractive index as well. The simulated response (Fig. 4.19a) is in good agreement with the experimental one (Fig. 4.19b). Small differences, such as the broadening of the peaks, arise due to the limitations of the measurement system and from small imperfections in the fabricated structures. A total of 100 reflectance spectra measurements for each concentration were carried out, and the automatically defined average value of the peak position was chosen for the refractometry calibration plot. In Figure 4.20, the peak shift is depicted as a function of the refractive index which was obtained from the Abbe refractometer; it followed the linear behavior as expected. From this graph, the sensor sensitivity of 319 nm/RIU was determined.

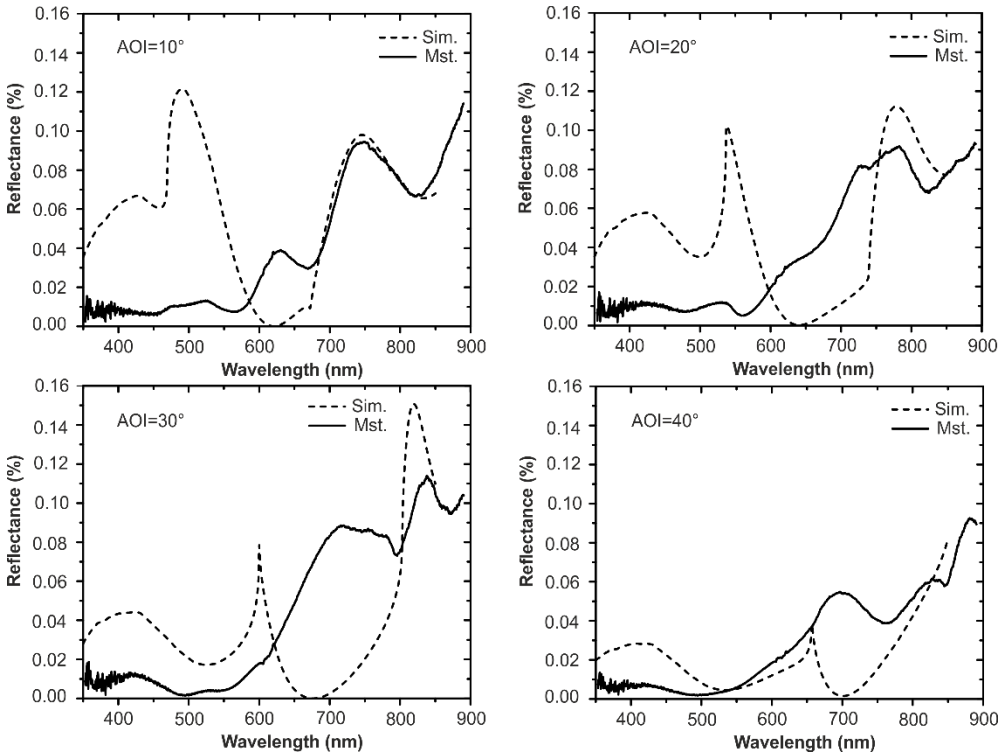

Figure 4.18. Simulated (Sim.) and measured (Mst.) reflectance spectra of a 400 nm period and ~150 nm depth grating fabricated in DLC:Ag. Recorded for TM polarization at different angles of incidence (AOI) in the air surrounding.

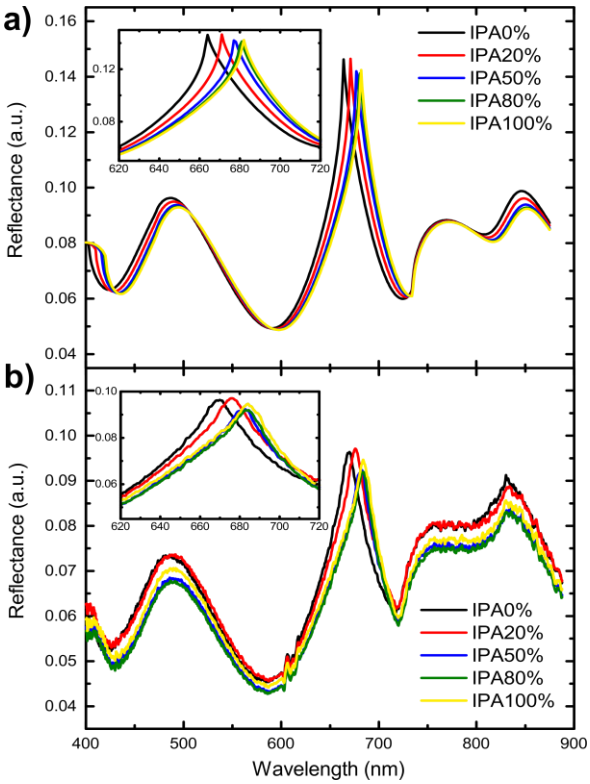

Figure 4.19. Simulated (a) and measured (b) reflectance spectra of different concentrations of isopropanol solution in DI water showing the GMR peak shift due to the changing refractive index. Measured and simulated with TM polarization at 20º angle of incidence of 400 nm period and 220 nm depth with 40 nm waveguide layer grating fabricated in DLC. The insets show the enlarged area of the resonance peaks.

This result represents an improvement close to 450% if compared with the previously reported sensors based on similar DLC films doped with silicon oxide and patterned by using interference lithography [8, 87, 99]. Such improvements are mostly due to the precise geometry control (the thickness of the waveguide layer in particular) enabled by the fabrication method and the improved optical properties (a higher refractive index) of the structural material. Furthermore, such sensitivity is much higher than that reported recently for conventional grating sensors [93, 96, 200]; it compares to the sensitivity which can be theoretically achieved in high complexity resonators [201]. The detection limit of this sensor, which quantifies the smallest refractive index change that the sensing platform can measure, was calculated according to the methodology presented in [202] and was determined to stand at 7.5 $\times 10^{-5}$ RIU. However, this is mostly limited by the spectrometer resolution and not by the developed arrays. A broad resonant peak linewidth would also impose limitations on the sensor performance when attempting to monitor very small changes close to the detection limit. However, the high sensitivity of DLC based sensors enables the utilization in areas where extreme sensitivity is not necessary but, instead, the cost and robustness are the key factors providing a higher accuracy with less sophisticated

peripherals, i.e., spectrometers, etc. The use of T-NIL combined with the SiPol resist allowed to straightforwardly pattern complex materials, which would usually require challenging and costly processes. This enables manufacturing of novel DLC-based systems with enhanced capabilities in a cost-efficient and reproducible mass-manufacturing method [168].

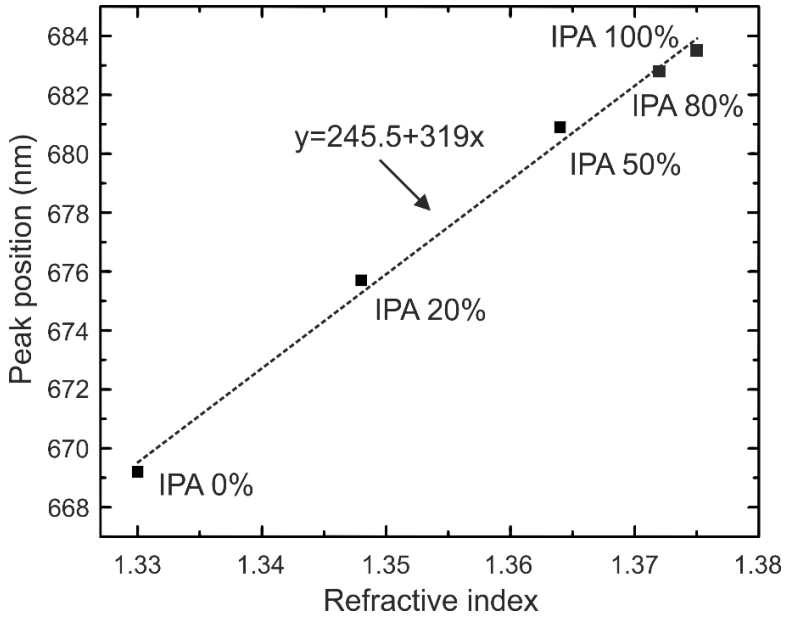

Figure 4.20. The experimentally obtained resonance peak position shift as a function of the analyte refractive index.

4.4 Fabrication of Regular Structures by Interference Lithography

The custom design automated laser interference lithography (LIL) setup based on Lloyd's mirror interferometer geometry was employed to produce sub-wavelength 1D and 2D regular structures. A positive tone photoresist maP-1205 (Microresist GmbH) was used as the recording medium for interference patterns. A thin photoresist layer was spin-coated at 3000 rpm for 30 s on 2×2 cm crystalline silicon substrates. Prior to spin coating, chemical cleaning of the substrates (dimethylformamide and acetone) and in O_2 plasma was performed in order to clean the surface and to enhance the adhesion. Photoresist-covered samples were placed in the lithography setup (described in more detail in Section 3.4) and exposed to radiation. 1D and 2D patterns with a periodicity of 288 nm were recorded. For the positive tone photoresist samples, the radiation dose of a single exposure was 40 mJ/cm^2. The exposed samples were developed in liquid developer MF-26A (Microresist GmbH) and blow-dried with compressed air. The produced structures were investigated with atomic force (NanoWizard 3, JPK) and scanning electron (Quanta 200 FEG, FEI) microscopes. SEM micrographs and AFM data presented in Figure 4.21 reveal that high resolution uniform periodic patterns over large areas were achieved. The line patterns were recorded by using one exposure, whereas the hole pattern was recorded by using double exposure with a sample rotation of 90º in between the recordings. From the

AFM data, one can see that the periodicity of both 1D and 2D patterns is around 288 nm, and the average height is about 20 nm for the line pattern and 25 nm for the hole pattern. The custom build interference lithography setup based on Lloyd's mirror interferometer geometry demonstrated the capability to produce not only linear but also more complex periodic patterns with a varying periodicity and point lattice symmetries over areas as large as 3×3 cm. [203] The LIL tool was initially developed to be used for the production of regular structures. These structures were intended to be employed in the production of refractive index sensors based on GMR as well as templates for capillary assisted particle deposition. However, due to lack of supporting techniques needed for a pattern transfer, at the time, further development was suspended, and the patterning route based on combination of an electron beam and the nanoimprint lithography was pursued instead. Nevertheless, the capabilities of the constructed LIL tool in terms of the achievable resolution and the patterning area are promising and will be utilized in other areas.

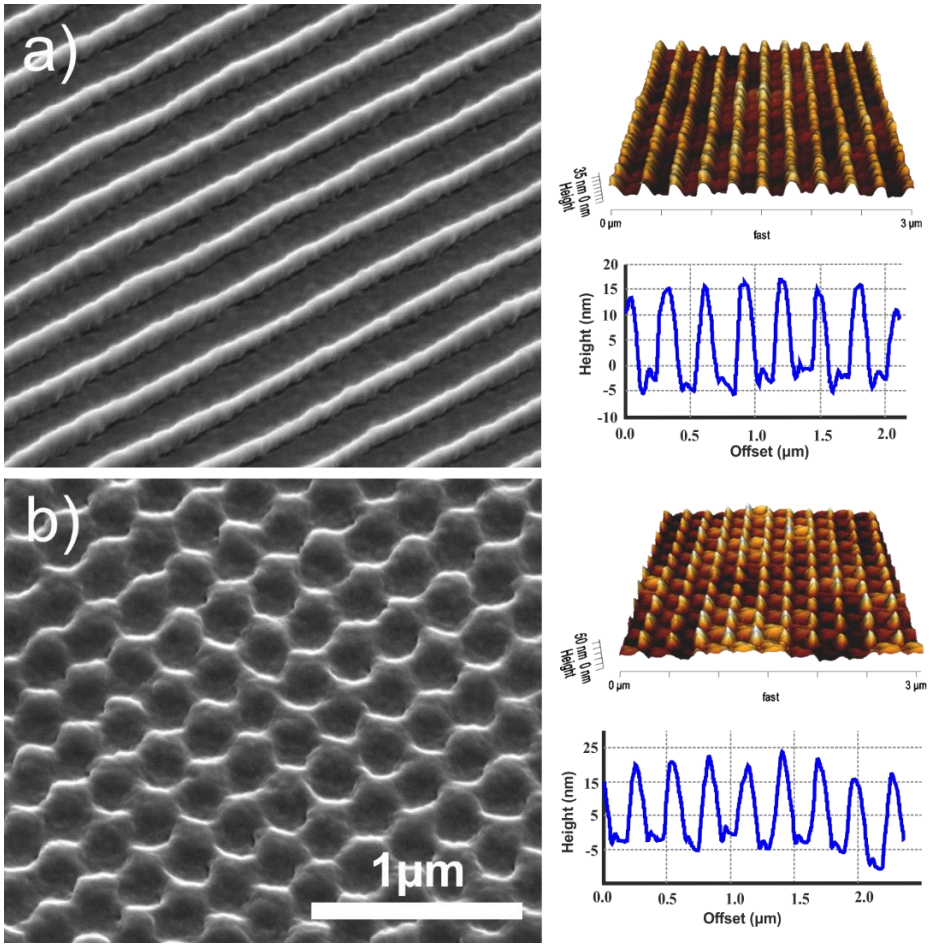

Figure 4.21. Periodic patterns fabricated by employing the custom interference lithography setup: a) line pattern with the period of 288 nm; b) regular hole pattern with the period of 288 nm.

4.5 Particle Deposition into Ordered Arrays by Capillary Forces

4.5.1 Template Influence on Particle Assembly

Custom built capillary assisted particle deposition setup (described in more detail in Section 3.6) was used to deposit particles ranging from 90 nm to 300 nm in an orderly fashion on patterned templates. The deposition is performed by controlled evaporation of a small droplet of colloidal suspension of particles confined on a topographically patterned surface. Evaporation induces convective flow of a solvent which overcomes the random Brownian motion of particles and drags them towards the contact line (the liquid-solid-vapor interface). When such a droplet is moved onto patterned surfaces, the combined effects of capillary forces stemming from the local distortion of the meniscus when the contact line is dragged over the structures and from the geometrical confinement induced by the structures lead to a selective immobilization of the particles in the recessed areas of the substrate, whereas no particles are deposited in the surrounding areas [109]. The template plays a key role when defining the particle localization and deposition efficiency. The assembly process is highly sensitive to the wetting properties of the surface and to the dimensions as well as the shape of the trapping sites. Successful deposition only occurs at certain angles of the receding meniscus. When the surface is hydrophilic, the droplet drag force is too weak to prevent particle sedimentation at the contact line, and thus the deposition becomes convective. Particles deposit into layers or if the droplet breaks into disordered agglomerations. On the other hand, when the surface wets too little (when it is hydrophobic), the vertical component of the in-act capillary force becomes too small to trap the particles. In this case, no deposition occurs, and the particles get dragged together with the droplet. The optimal ranges of the contact angle value as determined by other authors [109] were found to be in the range between 30º and 60º. These values may slightly vary depending on the particles in use and on the topography of the template. For that matter, two polymeric materials, PMMA and PDMS, were compared in order to determine their suitability for template fabrication. In this case, PMMA and PDMS were chosen because the patterns from the master stamp can be easily replicated into them either by casting or by imprint. Also, the large presence of $–CH_3$, $–CH_2–$ functional groups should be denoted by favorable wetting.

Figure 4.22 shows the contact angle measurements of both PMMA and PDMS with two liquids: water (H_2O) and a colloidal solution of nanoparticles (CS) having the solid content of 0.1 wt%. The preparation of the solution is described in Section 3.6.3. The wetting properties of the surface depend on its chemistry as well as on its structure. The testing was performed on a structured area of the surface. The surface was structured with the 2×2 μm^2 square hole with 2 µm spacing in between pattern which was intended to be used for the actual assembly. The template preparation is described in detail in Section 3.6.2. Droplets of 5 µL volume were used in all the cases. As it can be seen in Fig. 4.22a, both PMMA and PDMS are denoted by hydrophobic behavior when a water droplet is in contact. The contact angle for PMMA was determined to stand at 85.7º, whereas for PDMS it was found to be equal to 114.5º. The behavior completely changes when a CS droplet is in contact. For

PMMA, the contact angle drops to ~17º, and the surface becomes highly hydrophilic. For PDMS, the contact angle also decreases, albeit to a lesser extent, specifically, to 67º. These results might indicate that neither material is suitable because one wets too much whereas the other wets too little. However, during deposition, the droplet is constrained between the template and a stationary cover slide. The cover slide made of glass helps to reduce the surface tension. This makes the contact angle decrease on the template surface to ~45º (Fig. 4.22b) in the case of PDMS.

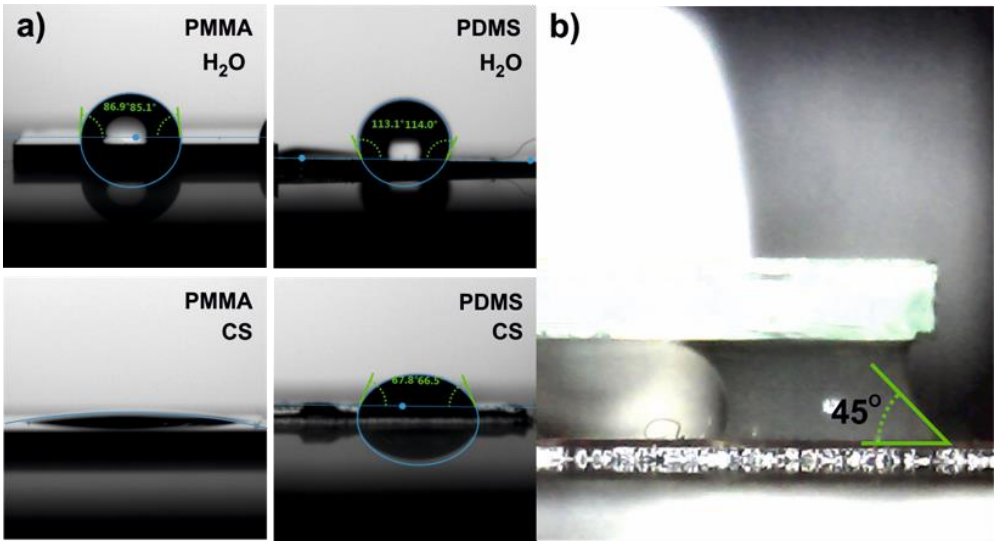

Figure 4.22. Contact angle measurements: a) contact angles of water and CS droplets on patterned PMMA and PDMS templates; b) contact angle of CS constrained between the cover slide and the patterned PDMS template during deposition.

It should be noted that it is also possible to control the contact angle by adjusting the surfactant concentration in CS. However, for PMMA. it was discovered that even with no additional surfactants, the contact angle of a constrained CS droplet in the deposition setup is still less than 30º. For these reasons, PDMS was selected for the fabrication of assembly templates.

The positional information on the particle arrangement is encoded in the template. In capillary assisted particle assembly, only topographical templates are used. During the assembly, the template geometry is translated into particle arrangement. The localization is imposed by the geometrical constraints of the trapping sites and the modulation of the capillary force caused by the pining of the droplet meniscus. The lateral dimensions of the trapping sites play a key role in defining the particle arrangement. The trapping sites may be larger than the particle's footprint or differ from its shape; a trapping site might also accommodate just a single particle or a large number of them. Figure 4.23 depicts silver particles having a shape of a regular octahedron with the edge length of 300 nm assembled on a template featuring differently-sized and shaped trapping sites. In all the cases, the dimensions of the traps are larger than the particle's footprint, and the geometries are simple, the holes are of a uniform depth in an otherwise continuous layer.

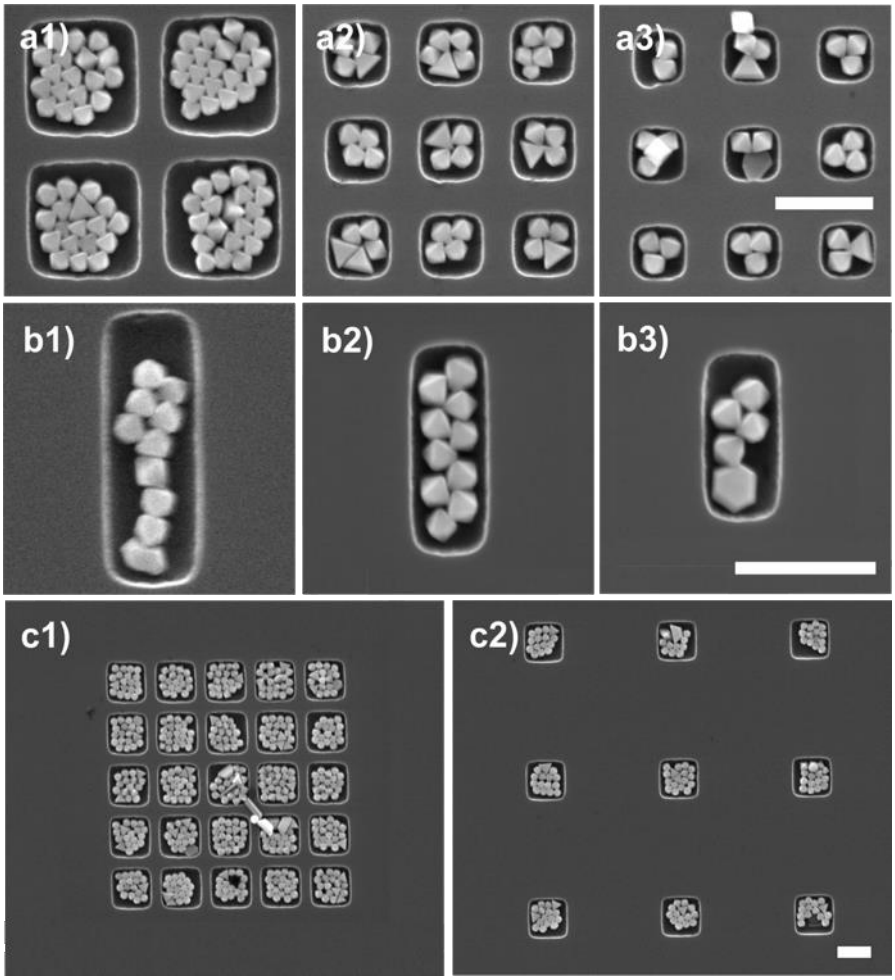

Figure 4.23. Octahedral silver particles assembled on a template of differently-sized trapping sites: a) Particles assembled in differently-sized square trapping sites; b) Particles assembled in differently-sized rectangular trapping sites; c) Particles assembled in square trapping sites of the same size but in a different density lattice. The scale bar is equal to 1 μm in all cases.

The particles mimic the geometry of the trapping sites and assemble accordingly. Figure 4.23a depicts such particles assembled in squares with the sides of 1.2 μm (a1), 660 nm (a2) and 570 nm (a3), respectively. Larger squares can accommodate a large number of particles, whereas in smaller ones only 4 and 3 can fit. Since particles are not symmetrical in all directions, the exact number depends greatly on their alignment, especially in the larger traps. As it can be observed, the particles are not uniform in size and shape, either. In Figure 4.23b, particles are assembled in elongated rectangles of 2.0×0.67 μm (b1), 1.5×0.55 μm (b2) and 1.0×0.55 μm (b3), respectively. Again, the same behavior is observed, as the particles assemble according to the geometric constraints imposed by trapping sites. In the cases when the orientation of particles is aligned, e.g., (b2), the filling rate is high;

whereas if there is no alignment, (b1) the filling is poor. Figures 4.23 c1 and c2 depict same-sized square trapping sites as in (a1) case laid out in a lattice of different densities. The density difference between cases c1 and c2 is 4:1. As it can evidently be seen, the density of the trapping sites has no effect on the deposition outcome as long as the high yield deposition mode is maintained by providing a sufficient flow of particles from the bulk of the droplet to the three-phase contact line.

If the template has trapping sites of a similar size compared to that of the particle, the deposition with a single particle resolution is possible. Figure 4.24 depicts such a case. The same octahedral silver NPs are assembled on a PDMS template with a pattern of 300 nm circular holes separated by a 300 nm pitch and ordered in the hexagonal arrangement. The SEM micrographs reveal that each individual particle occupies a single trapping site. Figure 4.24a depicts a large area of the assembled particles in order to demonstrate that pattern uniformity and high yield filling is maintained over a large scale. The bigger dark and bright spots seen in some parts are caused by the flaws of the template where no particles (dark) or several particles (bright) are deposited. Figure 4.24b presents a close-up view of the arrangement.

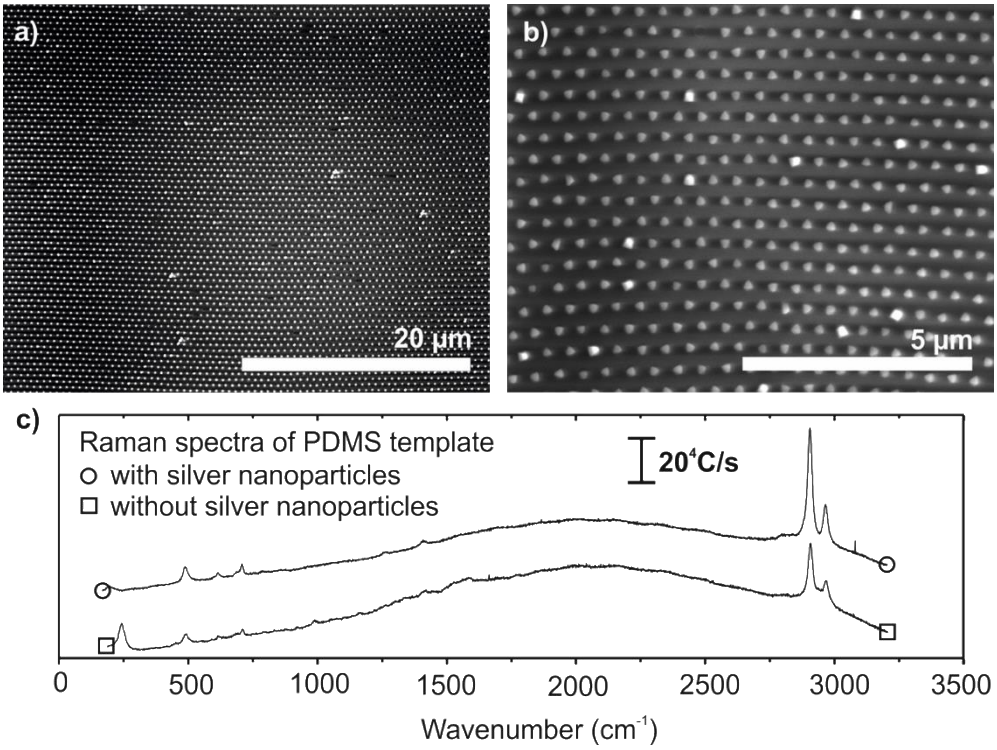

Figure 4.24. Octahedral silver particles assembled in a hexagonal arrangement of individual particles: a) a large area view of the arrangement; b) a close-up view of the arrangement; c) signature Raman signal of the PDMS template.

Signature Raman spectra of such a PDMS template were obtained by using an inVia Raman spectrometer (Renishaw); they are presented in Figure 4.24c. As it can be seen in the case with Ag NPs deposited on the surface, moderate signal intensity

improvement (up to 2x when comparing the intensities of the most pronounced peak at 2907 cm^{-1}) is observed. This showcases that such particle assemblies can be utilized in the fabrication of SERS substrates where Raman scattering of the target molecules is enhanced due to their proximity to intense local electromagnetic fields generated by the plasmonic interaction between the metallic NPs and the probing light. For flexible SERS sensing, NPs have to be assembled or transferred onto a different substrate (e.g., silicon) since PDMS background will interfere with the Raman signal of the target molecule. In the demonstrated case, only moderate signal intensity improvement is observed since the enhancement around individual NPs is comparatively weak and short-ranged. However, in the more complex assemblies featuring particle clusters with small interparticle gaps which provide very intense hotspots and overlapping of the excitation wavelength with strong resonance, much higher signal enhancements can be realized [111].

Not only the lateral dimensions of the trap geometry affect the outcome of the assembly process but the trap depth as well. The impact of the depth becomes particularly important when the capillary assembly is used to assemble particle clusters. This is clearly demonstrated in Figure 4.25 where a template containing trapping sites in the shape of square pits (2×2 μm) with the depth of 130 nm ordered in a regular fashion with 2 μm spacing in between the individual sites is used to deposit particles of different sizes. Fluorescent PS beads of a 90 nm diameter and fluorescent emittance in the blue part of the spectrum (Fig. 4.25 a, b) and PS beads of a 270 nm diameter and the green fluorescence (Fig. 4.25 c,d) were assembled respectively. The investigation of the assembled arrays with an optical microscope in both cases showed a fluorescence picture of the assembled particles that correlated accordingly to the lateral geometrical constraints of the template traps. However, fluorescence by itself cannot provide the full picture. In order to get information on how the particles are aranged in individual traps, SEM analysis was performed. The smaller particles occupy the whole space available in the trapping sites. In some cases, even a second layer with only partial filling starts forming. Figure 4.25b depicts the SEM micrograph of such particles (90 nm diameter) deposited in the traps. The poor contrast is due to the high surface charging effects of the insulating template and the particles. Nevertheless, the traps fully filled with particles can be evidently identified. The SEM analysis of the assembly of the bigger (270 nm diameter) particles with the green fluorescence reveals a different picture (see Fig. 4.25d). In this case, only partial filling of the trapping sites is observed. The average number of the assembled particles (over a larger area) per trap is only ~17 whereas the trap capacity in this case is ~60 particles. Observations imply that the trapping efficiency depends upon the depth of the traps and the size of the particle.

According to the recent study by Ni *et al*. [112], such a behavior can be explained by the delayed act of the capillary force upon particle resting in the different areas of the trap. As discussed above, in the capillary assembly, evaporation-induced viscous drag causes the particles to flow and concentrate at the front of the droplet meniscus thus creating an enriched area, the so-called particle accumulation zone. The particles in the accumulation zone tend to pack closely and to take up the entire locally available volume due to the buildup of osmotic pressure. This also includes the

volume of the traps in the template meaning that the particles preassemble into the traps even before the capillary force starts acting upon them. However, the capillary force is the one responsible for the permanent particle trapping in the assembly sites. During deposition, as a droplet moves over the template, its meniscus is pinned – and thus deformed – by the topographical traps. This meniscus deformation creates an elastic restoring force (the capillary force) which can act upon particles protruding from the traps and thus hold them in the trap. This force relates to the amount of protrusion and the tension of the elastic meniscus and therefore depends on the trap depth relative to the particle size and on the surface tension of the moving droplet. The trap depth plays an even greater role when larger traps hosting multiple particles are used. The capillary force generated by the meniscus acts perpendicularly to the meniscus; thus if there are more particles in the trap, they will not experience this force equally. In particular, the particles closest to the contact line will deform the meniscus and will experience an act of the capillary force first. As a result, the particles at the back of the trap (which are not yet interacting directly with the meniscus) may be pushed out of the trap by the front ones. Whether this happens or not depends on the strength and the direction of the capillary force relative to the trap orientation and the opposing action of the suspension's osmotic pressure as well as on other factors. The depth of the traps determines to what extent a particle will protrude from the trap and thus affects the strenght of the capillary force. The effect of the trap depth (d) for two particle asemblies is quantitatively described in [112]. It is shown that the driving force acting upon particles decreases with the increasing depth. Our experiments with a larger number of particles agrees with these observations. Therefore, a good rule of thumb for the successful deposition is to choose the ratio between the trap depth (d) and the particle radius (r) in the range $r<d<2r$.

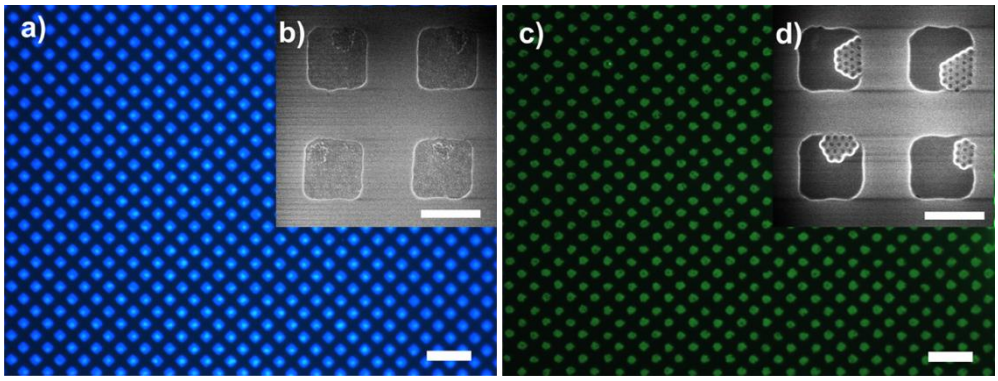

Figure 4.25. Florescent PS beads deposited on a template with square pits of 2×2 μm: a) Fluorescence of assembled 90 nm diameter PS beads. b) SEM micrograph showing how 90 nm particles are arranged in individual traps. c) Fluorescence of assembled 270 nm diameter PS beads. d) SEM micrograph showing the arrangement of 270 nm particles in individual traps. The scale bar of 2 μm applies for both SEMs; the scale bar of 10 μm applies for the fluorescence images.

4.5.2 Influence of the Ambient Conditions on the Particle Assembly

Deposition conditions, namely, the deposition velocity and the temperature of CS [109], as well as the particle concentration and the wetting properties (the surface tension) of the CS droplet meniscus [112] are the main factors influencing the assembly process. These aspects have been described and are already well-understood. Some external factors, such as relative humidity in the vicinity of the droplet, also exert influence; however, their effects are contradictory.

Very little attention so far has been paid to the description of the switching behavior in the transition from the low yield to the high yield deposition modes. The investigation of such switching dynamics and how its influenced by the variations of the deposition velocity and the temperature of the substrate is discused in the present chapter. Hereby, particle deposition experiments of 270 nm green fluorescent PS beads on patterned PDMS substrates with two patterns having a similar area fill factor were performed. One of the patterns consisted of closely packed 300 nm holes with a 300 nm pitch ordered in a hexagonal arrangement (the area fill factor equaling 19%), whereas the other pattern contained 2×2 μm^2 square holes ordered orthogonally with a 2 µm spacing (the area fill factor equaling 25%). As it has already been mentioned, the temperature of the colloidal suspension and the velocity at which the droplet is dragged over the patterned template surface are the key parameters defining the outcome of the CAPA process, i.e., the assembly yield. Therefore, multiple depositions were carried out at different temperatures and template velocities in order to assess the spatial evolution of the assembly yield in the transition zone from low to high yield regimes and the role of the parameters mentioned above on the deposition efficiency. The particle assembly was carried out by using the custom setup at ambient temperature ranging from 21 to 22°C and under relative humidity of 36–40%, accordingly. The dew point for these conditions was estimated to be in the range of 6–7°C. The template was placed onto the top of the sample holder and held in place by using a vacuum chuck. A small amount (30 µl) of prepared PS bead solution was restrained in between the template and the stationary glass cover slide. Temperatures starting at 8°C above the dew point were preset after the introduction of the solution, and the depositions were carried out by the movement of the translator at different velocities once the temperature had settled. All other conditions were kept constant or within a close range, including the concentration of particles in the suspension, the ambient humidity, etc. The deposition of particles was carried out over distances ranging from 50 to 300 µm. The distance was set to be higher proportionally to the increase of the deposition velocity due to the observation that the width of the transition zone increased accordingly. High yield assembly can only occur when the particle-enriched area (the accumulation zone) which feeds the assembly is formed at the front of the droplet meniscus. In order to reinitialize the particle accumulation zone under the new temperature and velocity conditions, it had to be completely dissipated before each new deposition. For that reason, a relatively high template translation speed of 50 µm/s was set between the two deposition areas separated with a gap of approximately 1 mm. At such a high translation speed, no particle accumulation zone could form, but a few particles were still trapped in the template's pits, and therefore the achieved deposition yield did not reach zero.

Fig. 4.26 depicts a collage of micrographs taken with a fluorescence microscope using a 20× objective. The micrographs display macroscopic areas of fluorescent PS beads assembled into dense hexagonally ordered trapping sites. Each micrograph depicts an area of assembly deposited at different conditions. The deposition direction is along the *x* axis. As it can be seen, an increase in the deposition velocity at which the template moves with respect to the stationary cover slide results in less efficient deposition. At temperature of 15ºC and velocity higher than 0.5 μm/s, the assembly is no longer able to reach ~100% efficiency. The assembly yield, once the transition period is over, varies between 70 and 90% (with the deposition velocity equaling 0.7 μm/s). This is due to the fact that the particle accumulation zone under these conditions becomes unstable, and the inflow and outflow of the particles takes place at similar rates. This causes the occurrence of irregularities in the assembly yield. Such irregularities in micrographs are seen as fluctuations in the fluorescence output. A further increase of the deposition velocity accelerates the particle outflow from the accumulation zone thus making it even more unstable and further degrading the deposition yield.

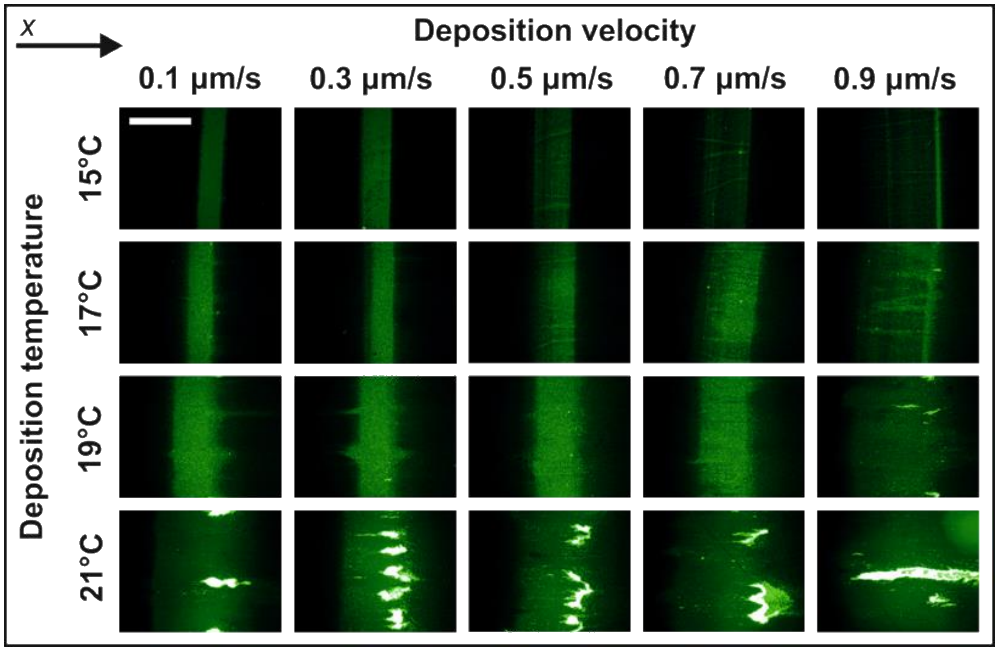

Figure 4.26. A stack of micrographs taken through a 20× objective depicting macroscopic view of the particle deposition area at different deposition conditions. 270 nm particles are assembled into dense hexagonally ordered traps. The deposition direction is along the *x* axis. The scale bar is 200 μm and applies for all cases.

On the other hand, an increase in temperature increases the flux of PS beads from the bulk of the droplet into the accumulation zone. This enables high yield deposition at higher velocities. At the deposition temperature of 17ºC, the yield no longer reaches ~100% at velocity higher than 0.7 μm/s. At temperatures of 19ºC and higher, the assembly was always able to reach ~100% yield within the investigated

velocity range. However, as the temperature reached higher values (21ºC in our case), the particles started to agglomerate and deposit in large aggregates. Such behavior is most likely caused by the elevated solvent evaporation, which limits particle mobility in the accumulation zone. Graphs in Fig. 4.26 depict the typical region of interest (ROI) showcasing the transition zone from low yield (the area of the low intensity green fluorescence) to the high yield (the area of the high intensity green fluorescence) deposition.

Figure 4.27 depicts similar areas with deposited fluorescent particles as in the previously presented experiment, only in this case, the particles were assembled into a sparse orthogonal array of square (2×2 μm^2) pits. The process dynamics is similar; however, due to a lower particle density (1.1 part/μm^2) as compared with the previous case of the hexagonally ordered holes (3.5 part/μm^2), the applied deposition velocities are higher. The increase of velocity at which successful deposition can be performed and maintained is pretty much proportional to the decrease in the deposited particle density on the surface. As in the previous case, the deposition errors caused by the particle agglomeration start to occur at around the same temperature of 21ºC but are manifested to a lesser extent.

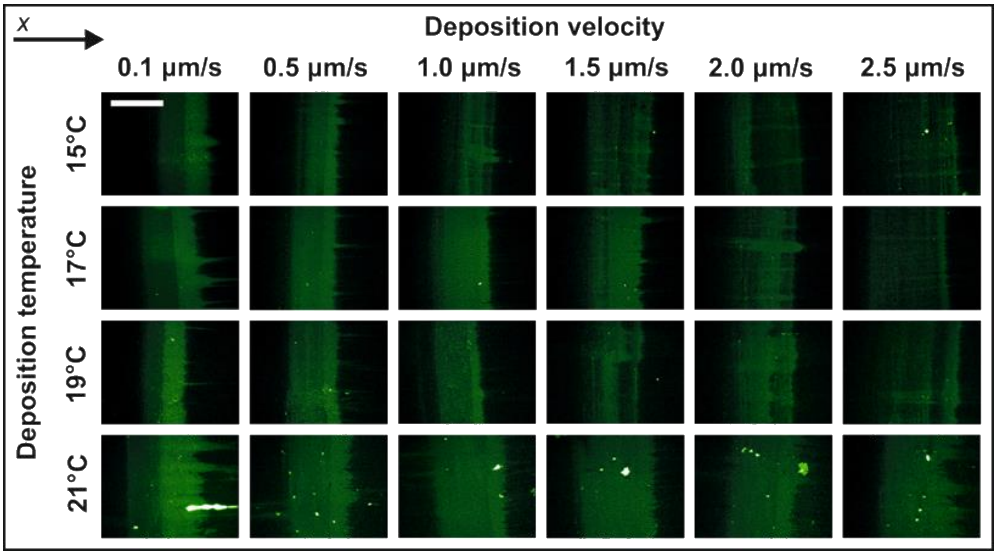

Figure 4.27. A stack of micrographs taken through a 20× objective depicting macroscopic view of the particle deposition area at different deposition conditions. 270 nm particles are assembled into a square array of 2×2 μm^2 pits separated by 2 μm gaps. The deposition direction is along the *x* axis. The scale bar is 200 μm and applies for all cases.

Fig. 4.28a depicts SEM micrographs of both patterns after the deposition process. Two characteristic areas for both patterns of a low deposition yield (a1, a4 images) and a high deposition yield (a2, a5 images) as viewed from a close distance, as well as a lower magnification image representing wider areas showcasing the change of the deposition yield (a3, a6 images) are presented. One can see that the square pits are not completely filled with the particles. It was found that the average

number of particles trapped in a single square pit during a high deposition yield regime is 17 on average instead of the theoretically possible value of up to 60 particles.

The same particle filling level is observed under all investigated deposition conditions and could be attributed to the insufficient depth (130 nm) of the trapping sites due to the effects explained in the previous chapter. Even though the area fill factors (19% and 25%) are very similar for both templates and should result in a similar density of particles, the achieved densities were estimated to be roughly 3.5 part/μm^2 for the hexagonal array, and only 1.1 part/μm^2 for the orthogonal array due to the incomplete filling of the latter. In further assessments, this value was considered to be the full capacity of the square array of 2×2 μm^2 pits in terms of their capacity to contain particles, i.e., it was treated as the relative filling efficiency of 100%. The pattern irregularities and wobbles that can be seen in the SEM pictures are not replication errors but are actually caused by the chromium layer (deposited on top of the assembled arrays for a better imaging contrast) which imposes mechanical strain upon PDMS. Fig. 4.28 (b1–b3) presents analogous areas as seen through a fluorescence microscope for a dense pattern, and Fig. 4.28 (b4–b6) demonstrates analogous areas for a scarce pattern.

Experimental implementation enabled to investigate the dynamics of the deposition transition from a depletion (the deposition velocity of 50 μm/s) area to a high yield (low velocity) area reflecting the spatial evolution of the particle deposition efficiency. The custom MatLab algorithm was used to analyze fluorescence micrographs. Images of the assembly area were converted to an 8-bit gray scale matrix of pixel intensities. Since the images were taken so that the assembly direction were horizontal, each column vector of such a matrix represented an intensity profile at some template translation coordinate (or the time of assembly). Templates of different trap sizes could theoretically accommodate a different number of particles per trap, i.e., a single particle per hexagonal array of 300 nm pits and up to 60 particles per 2 × 2 μm^2 square pits in the orthogonal array. Thus, every peak in such a profile meant an increase in the fluorescence intensity and indicated the presence of a particle or a stack of particles in the trapping site. The following equation was used to calculate the assembly yield at every template translation coordinate:

$$Y = N_{PR}\frac{N_P}{N_T} \tag{4.2}$$

where Y is the assembly yield; N_{RP} represents the relative number of particles per trap; N_P stands for the number of traps containing particles; N_T is the total number of traps.

For a template with 300 nm diameter pits where only a single particle can fit in (N_{RP}=1), a MatLab code counting only the number of peaks (N_P) was employed. The assembly yield indicating the ratio of the filled traps (N_P) to the total number of traps (N_T) was plotted against the coordinate x of the template. The x axis is along the direction of deposition, which coincides with the movement of the droplet on the template surface.

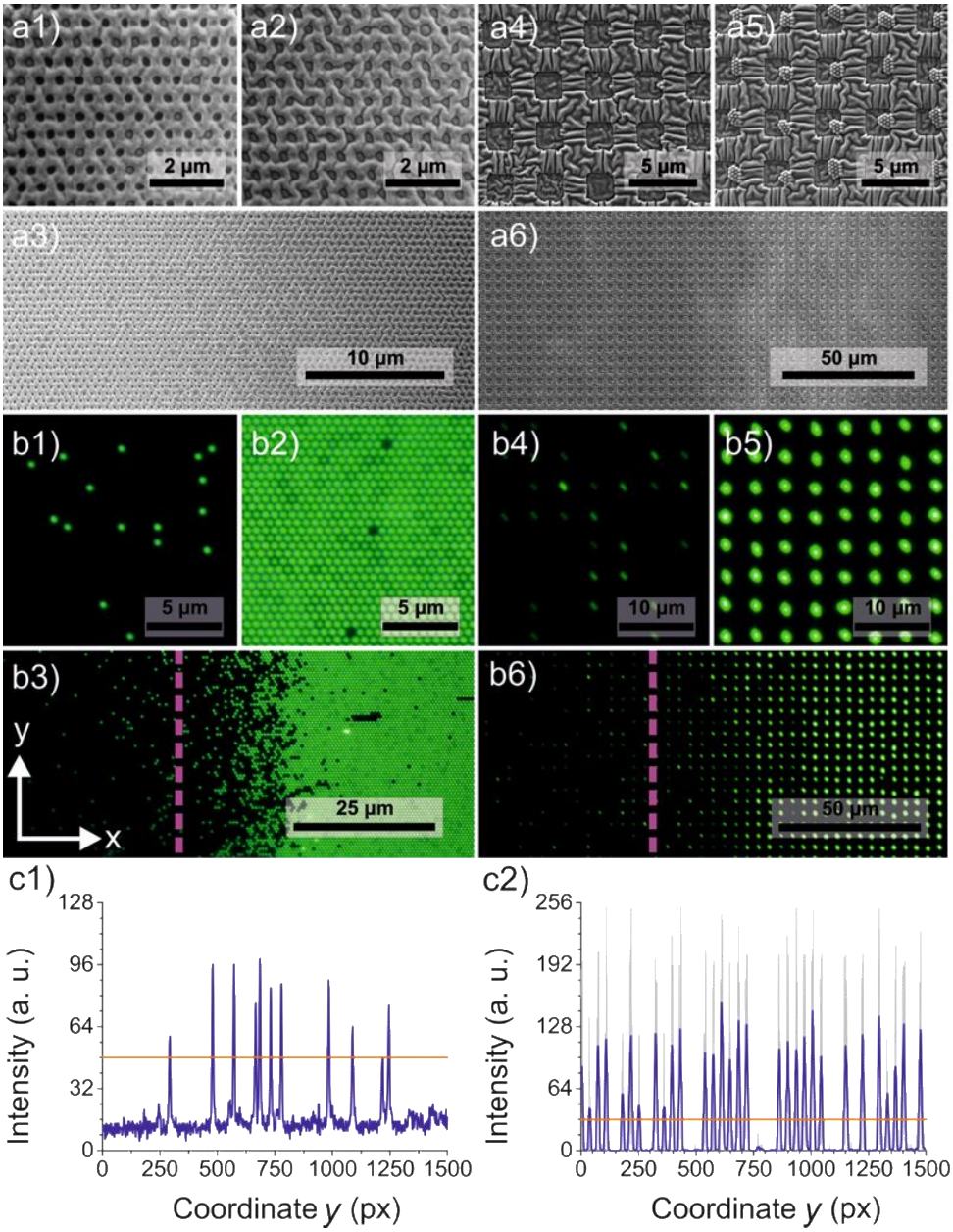

Figure 4.28. a) SEM micrographs of 270 nm diameter green fluorescent PS beads assembly in the transition areas (a3, a6) on two different geometry patterns showcasing: the areas of low (a1, a4) and high (a2, a5) deposition yields; 0.1 µm/s velocity and 15°C temperature was used. b) Fluorescence images of analogous low (b1, b4) and high (b2, b5) assembly yield areas as seen through the optical microscope; (b3, b6) show the same areas at a lower magnification. c) Typical line scan applied upon dense (c1) and scarce (c2) fluorescence images showcasing the algorithm employed to identify and count the yield of the assembled particles at the corresponding position across the direction of deposition (*x* axis).

As for the template with 2×2 μm^2 pits, the number of particles assembled per single trap (N_{RP}) had to be additionally weighed to correctly estimate the assembly yield. Therefore, after performing the counting of the peaks (NP), an additional step was applied to calculate the average *Full Width at Half Maximum* (FWHM) of these peaks in both horizontal (x) and vertical (y) directions thus providing the average fluorescent spot size in a single column, which directly correlates to the number of particles per filled trap (N_{RP}).

The dashed vertical lines in the b3, b6 (Fig. 4.28) pictures represent the scan profile positions pictured in c1 – a dense hexagonal pattern, c2 – a sparse orthogonal pattern which were obtained by analyzing micrographs while using the custom algorithm. The peaks represent the particles in the trap, whereas the red line represents the threshold level of the background noise for each case, respectively.

All the experimental assembly yield graphs were approximated by using a logistic function:

$$Y(x) = Y_{min} + \frac{Y_{max} - Y_{min}}{1 + e^{-k(x-x_0)}} \tag{4.3}$$

where x is the coordinate along the template translation direction, Y_{min}, Y_{max} are the critical values of the assembly yield; x_0 is the template coordinate at $(Y_{max} - Y_{min})/2$, and k is the slope of the function.

A typical example of such analysis for an assembly on a hexagonal pattern is depicted in Fig. 4.29 where the transition of the deposition yield versus the x coordinate is presented. Fig. 4.29a depicts such a transition taking place at velocity of 0.1 μm/s and under temperatures of 15ºC and 21ºC. Fig. 4.29b depicts such a transition at a constant temperature of 19ºC and at 0.1 μm/s and 0.7 μm/s template translation velocities respectively. As it can be seen, the transition at a lower velocity results in the faster (in terms of the distance traveled) rise of the assembly yield than in the case of a higher velocity. On the other hand, for this particular pattern, the temperature weighs in to a much lesser extent.

Fig. 4.30 depicts a transient zone registered at translation speed of 1.5 μm/s and at 19ºC temperature when the template having array of square pits was used. In this case, even at high translation velocity (50 μm/s) a large number of traps was still filled with at least 1 particle. The filling was usually in the range of 1–3 particles per trap. This fact was considered when calculating the true deposition yield by normalizing the fluorescence emittance (Fig. 4.30b). This graph, combined with the one showing the number of traps with at least one particle in it (Fig. 4.30a), gives the true assembly yield (Fig. 4.30c) for the template featuring square pit trapping sites. The transient zone can be approximated with the logistic function in a same manner as in a hexagonal pattern case. It is worth noting that the transition zone which can be roughly estimated to be 100 μm wide takes approximately 67 s to fully develop in the depicted case.

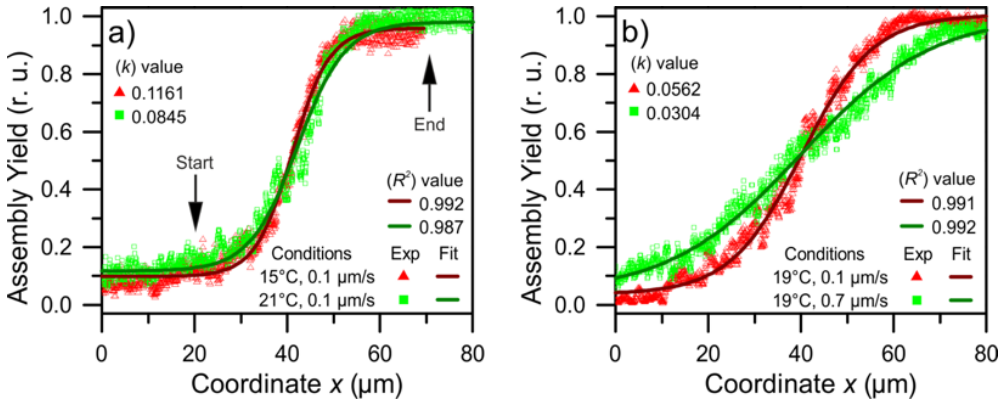

Figure 4.29. Particle yield dependence versus template coordinate illustrating the dynamics in the transition area from the low to the high yield at different assembly conditions. The particles were assembled into hexagonally ordered arrays with a distance of 300 nm in between the separate particles: a) the transition region at a constant velocity (0.1 μm/s) and different temperatures of 15ºC and 21ºC. b) the transition region at a constant temperature (19ºC) and different velocities of 0.1 μm/s and 0.7 μm/s.

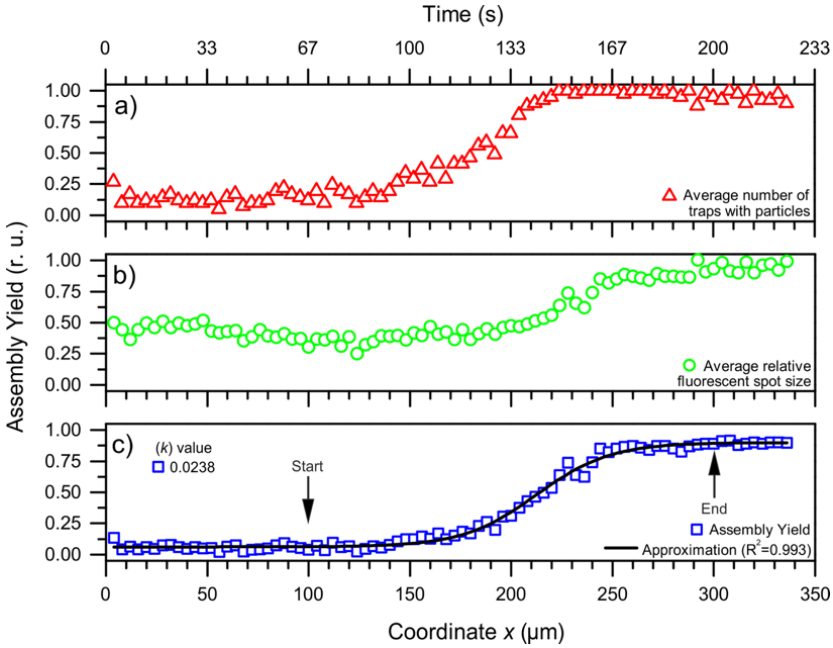

Figure 4.30. Particle yield dependence versus template coordinate illustrating the dynamics in the transition area from the low to the high yield for the particles assembled into a square array of 2×2 μm^2 pits separated by 2 μm gaps at 1.5 μm/s velocity and 19ºC temperature: a) the average number of traps with at least one particle; b) the average relative fluorescent spot; c) the assembly yield.

As one can see, in most cases, for both patterns, the transition from low to high yield deposition could be quite accurately approximated by a logistic function (R^2 not worse than 0.95). The steepness of the curve is defined by parameter *k* near the exponent in the logistic equation (Eq. 4.3). The slope (*k*) indicates the rate at which the assembly yield switches from low to high values thus enabling to evaluate deposition efficiency dynamics – the higher the slope is, the faster (in terms of distance) the switching from the low to the high yield assembly takes place. Fig. 4.31 depicts the *k* value which was calculated by fitting the logistic function to the experimental data distribution with respect to the deposition conditions (*T* and *v*) for both patterns. As it can be seen in the *k* distribution maps, the dense pattern of the 300 nm diameter hexagonally ordered pits (Fig.4.31a) features higher absolute *k* values than the scarce pattern with square 2×2 μm^2 trapping sites (Fig.4.31b). The transition steepness, i.e., the *k* values for a less dense pattern exhibits maximum values in the region of high temperatures (18–21°C) and is not so sensitive to the velocity. For a densely packed pattern, this relationship is quite opposite, i.e., the faster switching from the low yield to the high yield is observed in the region of lower temperatures and low velocities (0.1–0.5 μm/s). Although intuitively one could expect *k* values to be monotonous with relation to the deposition parameters, in this particular case they are not. These fluctuations are likely to be caused by the randomness of the imaging area selection as well as by the unpredictable nature of the technique itself – no deposition is ever the same. This could also be related to the statistical fluctuations of the assembly as well as to the unstable relative humidity in the vicinity of the process area. On average, however, the difference between the *k* values at low and high velocities for the dense pattern (Fig. 4.31a) and at low and high temperatures for the scarce pattern (Fig. 4.31b) is quite substantial, and therefore these directions should be given more attention. Bearing all that in mind, different temperature-velocity settings should be used for patterns of different density providing optimal transition zones [204].

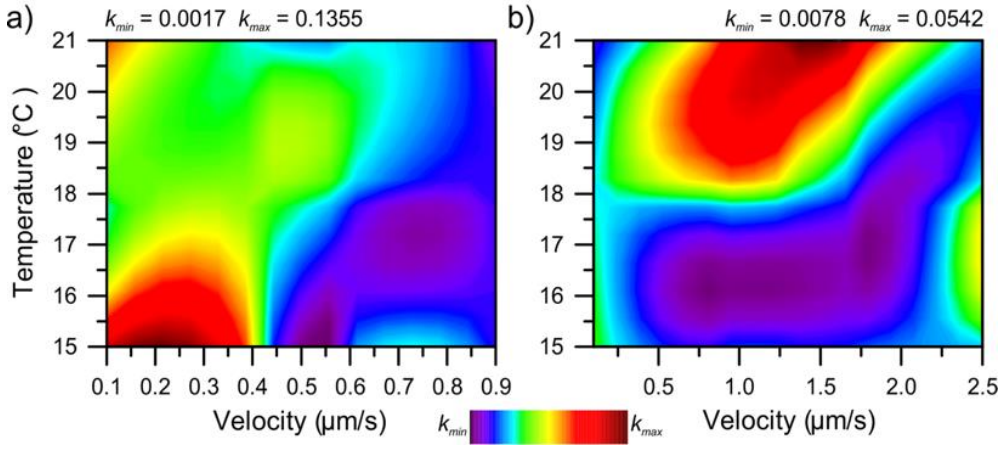

Figure 4.31. The dependence of parameter *k* on the temperature and the deposition velocity for two different templates: a) for an assembly of particles into hexagonally ordered arrays with a pitch of 300 nm in between separate particles; b) for an assembly of particles into square arrays of 2×2 μm^2 and separated by 2 μm gaps.

4.5.3 Complex Multi-Particle Assemblies

Insights into factors influencing the particle assembly yield and its special distribution in the transition zone can be exploited to produce some complex arrangements where a different type of particles is used. Such arrangements can be achieved by performing two or more consecutive depositions at regimes yielding different deposition efficiency. The first deposition performed at a low yield regime is used to define the pattern. Then, the second deposition on top of the already deposited particles performed at a high yield regime fills the empty trapping sites left after the first deposition. The already deposited particles are strongly bonded to the substrate and are not affected by the following depositions.

In such assemblies, the individual particle position on a template is random, but it is possible to control the yield of certain particles over a larger area as depicted in Fig.4.32, where two types of particles, 270 nm diameter green fluorescent polystyrene (PS) beads and 90 nm diameter blue fluorescent polystyrene beads, are assembled on the same template. The particles of the green fluorescence were assembled first under conditions when only partial filling was achieved. Fig. 4.32 a1 depicts the area of the first assembly where only ~13% yield was achieved (v: 10 μm/s, T=15ºC). Fig. 4.32 a2 depicts ~60% yield area (v: 3 μm/s, T=15ºC). Sequentially performed second deposition at high yield conditions (v: 0.1 μm/s, T=15ºC) fills the sites that were left empty after the first one (Fig. 4.32 b1, b2). A careful selection of the trapping sites' geometry enables to carry out a second deposition with particles of different sizes in such a way that only the empty sites left after the first deposition are filled. As depicted in Fig. 4.32c and d, a single circular 300 nm diameter and 300 nm depth pit can trap a single particle of the 270 nm diameter and 21 particles of the 90 nm diameter (3 layers with 7 particles in each layer since the depth of the pit is 300 nm). This approach enables to produce randomly ordered unique patterns of fluorescent particles that can be used as security elements that enhance the security level of, e.g., legal documents. The security originates from the random 'fingerprint-like' pattern created by the local distribution of blue and green particles on the patterned template. As shown in Fig. 4.32a, when the structure is illuminated with the blue light, only green fluorescence is visible. When illuminated with the UV light (Fig. 4.32b), both green and blue fluorescent particles become visible.

In the pictured area (~ 23×23 μm^2), there are up to 2^{1547} possible arrangements of the particles. Additional layer of security is added by the fact that particles can have not only different color fluorescence but also a different size or shape which can be identified through closer investigation, e.g., by SEM. Such complexity is impossible to achieve via the conventional route when a mixture of particles is used like in [120] because that would lead to differently sized particles occupying the same trapping sites. It can only be achieved by working with a template featuring differently shaped (sized) trapping sites; however, then particle localization is predefined by the template, and the random nature of the arrangement is lost. Also by working at a transient regime, it is also possible to produce gradient type particle arrangements where one particle population is gradually replaced by another.

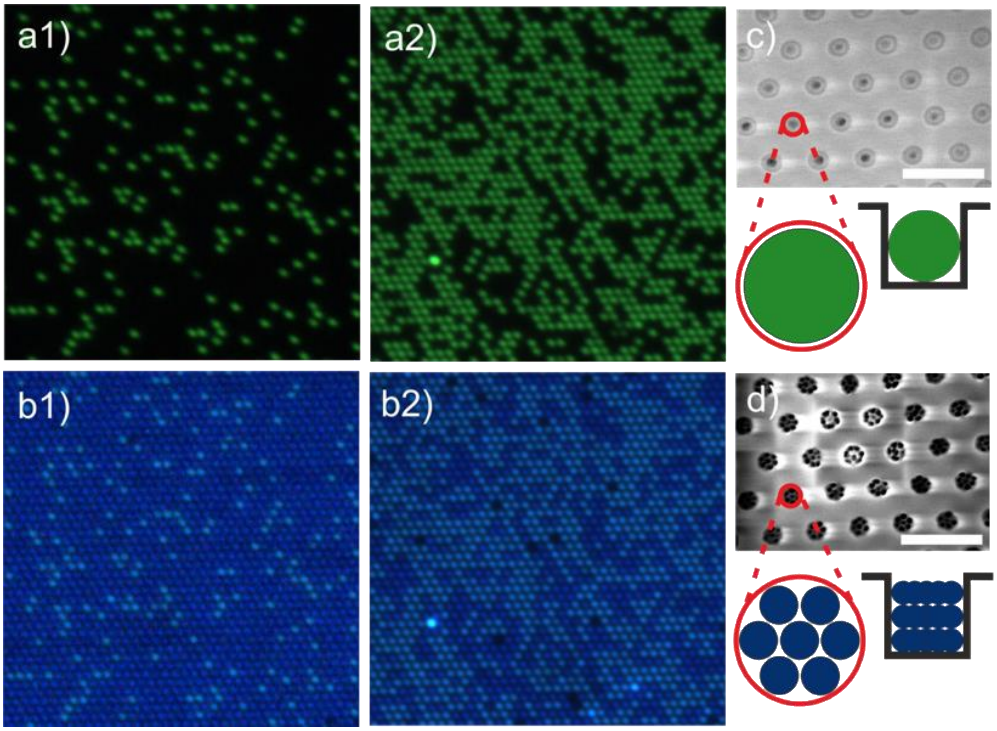

Figure 4.32. Fluorescence microscopy images showing a two-step deposition of 270 nm diameter (green fluorescence) and 90 nm diameter (blue fluorescence) particles on the same template. The bigger particles were assembled first under low yield conditions: a1) the assembly area of ~13% yield; a2) the assembly area of ~60% yield; b1) and b2) depicts an analogous area as it is seen in the UV light after the second high yield deposition of smaller particles filling the remaining traps. In c), a SEM image depicts 270 nm particles assembled in trapping sites; d) a SEM image of smaller particles assembled in trapping sites. The graphical insets depict the top and the side view of the assembled particles in the pits. The scale bars represent 1 µm distance.

Beside randomly ordered arrangements, it is also possible to create highly ordered composite particle arrays. Figure 4.33 shows a microscope image of the sequential assembly of green and blue PS beads. The inset in Fig. 4.33 illustrates the assembly procedure. First, green beads were assembled in one area at high deposition yield conditions (v: 0.3 µm/s, T=15ºC). Then, blue beads were assembled with an offset relative to the green bead assembly area. In this way, a composite array of green and blue beads with a sharp transition between the beads of different colors can be fabricated. In such a case, the already assembled green beads during the deposition of blue beads block the assembly sites in the blue-green overlap area.

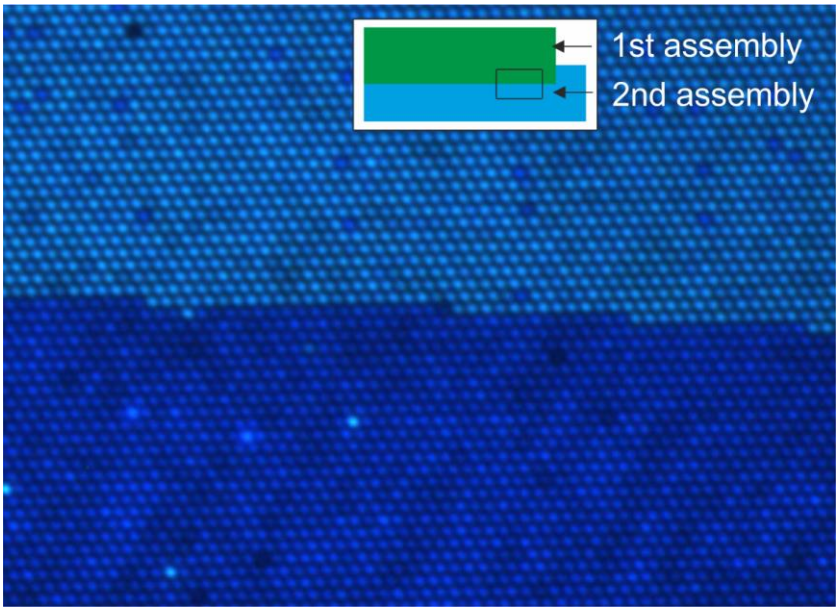

Figure 4.33. Fluorescence microscopy images showing a two-step deposition of 270 nm diameter (green fluorescence) and 90 nm diameter (blue fluorescence) particles on the same template. Shown in the inset is the principal assembly procedure. First, green beads were assembled, then, blue beads were assembled with a position offset relative to the already assembled green beads.

5. CONCLUSIONS

1. Successful use of the new thermoplastic resist SiPol as a hard mask to pattern DLC films by thermal NIL process was demonstrated. SiPol can serve as an efficient hard mask for etching DLC coatings ensuring 1:4 selectivity for non-doped and 1:2.5 for silver doped DLC coatings. Adhesion issues can be addressed by using a low temperature imprint in combination with the incomplete filling of stamp cavities. The low temperature imprint approach combined with the incomplete filling of stamp cavities not only allows a virtually zero residual layer imprint but also facilitates the original SiPol process involving an organic transfer layer by removing the intermediate etchings and resulting in the most efficient processing strategy.
2. DLC coatings and, to some extent, DLC coatings doped with silver can be effectively etched by oxygen with inductively coupled plasma systems. Such processing enables homogeneous, high precision transfer of the desired patterns with the depth measuring at least up to 500 nm into DLC over the areas of $20\times20mm^2$. Current applications have a moderate aspect ratio and resolutions down to several hundred nanometers, which does not seem to be the ultimate limit.
3. High quality DLC based subwavelength period gratings were fabricated by the developed T-NIL with the imprintable hard mask method. They have demonstrated guided-mode resonance spectral response and were characterized as refractive index sensors. The optical response showed a high agreement with the simulations of ideally rectangular gratings resulting in measured high sensitivity (319 nm/RIU) to the refractive index changes in the analyte and representing an improvement of almost 450% compared to previous works.
4. Oxygen based plasma etching of the DLC:Ag nanocomposite films by selectively removing carbon matrix reveals an embedded silver filler to the surface. Such processing enables to control the amount and the size of the silver nanoparticles on the surface of the film thus providing a possibility to tailor their properties. Films with the lower silver concentration demonstrated narrow particle size dispersion, which fitted well log-normal distribution, and over extended processing duration, showed only a slight tendency to coarsen. Films with the higher silver content demonstrated Ostwald ripening and coalescence inducted particle coarsening, which, under extended processing duration, resulted in the formation of large silver clusters producing silver enriched and depleted zones on the surface.
5. By using different yield sequential deposition regimes, it is possible to produce randomly ordered particle arrays where particles of different sizes and attributed with dissimilar functionalities (e.g., fluorescence color) can be assembled in a non-mixing fashion on a template with only one type of

trapping sites. This enables the creation of enchased security features where not only the color but also the size of the particles is different.

6. Custom capillary assisted particle assembly and laser interference lithography setups were designed, constructed and tested. These tools were shown to be capable to produce ordered arrangements of matter approaching nanoscale dimensions. They will continue to be used as part of the instrumental base in the future research.

LIST OF PUBLICATIONS

Publications Related to the Dissertation

Publications in journals with impact factor indexed by *Clarivate Analytics Web of Science* Database

1. **Virganavičius, D.**, Juodėnas, M., Tamulevičius, T., Tamulevičius, S., Schift, H. (2017). Investigation of Transient Dynamics of Capillary Assisted Particle Assembly Yield. *Applied Surface Science. 2017, Vol. 406, pp. 136–143*. [IF: 3.150].
2. **Virganavičius, D.**, Cadarso, V.J., Kirchner, R., Stankevičius, L., Tamulevičius, T., Tamulevičius, S., Schift, H. (2016). Patterning of Diamond Like Carbon Films for Sensor Applications Using Silicon Containing Thermoplastic Resist (SiPol) as a Hard Mask. *Applied Surface Science. 2016, Vol. 385, pp. 145–152.* [IF: 3.150].
3. Tamulevičius, T., Tamulevičienė, A., **Virganavičius, D.**, Vasiliauskas, A., Kopustinskas, V., Meškinis, Š., Tamulevičius, S. (2014). Structuring of DLC:Ag Nanocomposite Thin Films Employing Plasma Chemical Etching and Ion Sputtering. *Nuclear Instruments and Methods in Physics Research Section B. 2014, Vol. 341, pp. 1–6.* [IF: 1.389].

Publications in other journals listed in the *Web of Science* Database (proceedings, etc.)

1. **Virganavičius, D.**, Šimatonis, L., Jurkevičiūtė, A., Tamulevičius, T., Tamulevičius, S. (2014). Formation of Sub-Wavelength Pitch Regular Structures Employing a Motorized Multiple Exposure Lloyd's Mirror Holographic Lithography Setup. *Proc. SPIE 9170, Nanoengineering: Fabrication, Properties, Optics, and Devices XI, 91701I.*

Other Publications

1. Abakevičienė, B., Grigaliūnas, V., Sakaliūnienė, J., **Virganavičius, D.**, Šlapikas, K., Mikolajūnas, M., Tamulevičius, S. (2014). Modelling and Fabrication of Micro-SOFC Membrane Structure. *Materials Science.2014, Vol. 20, No. 2, pp. 223–227*. [IF: 0.428].

List of Conference Contributions Related to the Dissertation

1. Jurkevičiūtė, A., Armakavičius, N., Šimatonis, L., **Virganavičius, D.**, Tamulevičius, T., Tamulevičius, S. (2013). *Multiple Exposure Holographic Lithography for Two-Dimensional Sub-Micrometer Structures*. (2013). International Conference Open Readings / Laisvieji skaitymai 2013, March 20–23, 2013, Vilnius, Lithuania (poster presentation).
2. **Virganavičius, D.**, Jurkevičiūtė, A., Armakavičius, N., Tamulevičius, T., Tamulevičius, S. (2013). *1D and 2D Periodic Microstructures Formation Employing Holographic Lithography* // International Conference Developments in Optics and Communications, April 10–12, 2013, Riga, Latvia (oral presentation).
3. Jurkevičiūtė, A., **Virganavičius, D.**, Armakavičius, N., Šimatonis, L., Tamulevičius, T., Tamulevičius, S. (2013). *Dvimačių periodinių strukturų suformuotų holografinės litografijos metodu aprašymas taškinių gardelių tipais* // 40th Lithuanian National Conference of Physics, June 10–12, 2013, Vilnius, Lithuania (poster presentation).
4. **Virganavičius, D.**, Tamulevičius, T. Tamulevičius, S. (2013). *Surface Patterning of DLC Films Using Holographic Lithography Technique* // The 15th International Conference-School *Advanced Materials and Technologies*, August 27–31, 2013. Palanga, Lithuania (poster presentation).
5. **Virganavičius, D.**, Jurkevičiūtė A., Tamulevičius, T., Tamulevičius, S. (2014). *Formation of Regular Structures Employing Holographic Lithography Technique* // Preparatory School + Winter College on Optics: Fundamentals of Photonics – Theory, Devices and Applications, February 3–21, 2014. The Abdus Salam International Centre of Theoretical Physics, Trieste, Italy (poster presentation, awarded 2nd place prize in the best poster presentation competition).
6. **Virganavičius, D.**, Tamulevičius, T., Tamulevičius, S. (2014). *Capillary Assisted Particles Deposition on Topographic and Wetting Angle Contrast Templates for Plasmonic Sensing Applications* // XII Conference on Optical Chemical Sensors & Biosensors EUROPT(R)ODE April 13–16, 2014. Athens, Greece (poster presentation).
7. **Virganavičius, D.**, Šimatonis, L., Tamulevičius, T., Tamulevičienė, A., Tamulevičius, S. (2014). *Patterning of Regular Structures for Refractive Index Sensor Chips Employing Automated Lloyd's Mirror Holographic Lithography Setup* & Tamulevičienė, A., Tamulevičius, T., **Virganavičius, D.**, Kopustinskas, V., Tamulevičius, V. *Template Formation for Self-Assembly of Micro Particle Arrays* // 5th International conference Radiation Interaction with Materials: Fundamentals and Applications 2014, May 12–15, 2014. Kaunas, Lithuania (2 poster presentations).
8. **Virganavičius, D.**, Tamulevičius, T., Tamulevičienė, A. Tamulevičius, S. (2014). *Capillary Assisted Particles Deposition on Topographic Templates* //

International Conference Nanotechnology: Research and Development May 15–16, 2014. Vilnius, Lithuania (poster presentation).

9. **Virganavičius, D.**, Jurkevičiūtė, A., Armakavičius, N., Šimatonis, L., Čiučiulkaitė, A., Tamulevičius, T., Andrulevičius, M., Tamulevičius, S. (2014). *Formation and Characterization of Two-Dimensional Regular Patterns Fabricated Employing Multiple Exposure Holographic Lithography* // EMRS Spring Meeting 2014, May 26–30, 2014. Lille, France (poster presentation).
10. **Virganavičius, D.**, Tamulevičius, T., Tamulevičius, S. (2014). *Capillary Assisted Particles Deposition on Topographic and Wetting Angle Contrast Templates* // PolyNano Summer School 2014, August 18–29, 2014. DTU Nanotech, Lyngby, Denmark (poster presentation).
11. **Virganavičius, D.,** Tamulevičius, T., Šimatonis, L., Tamulevičienė, A., Tamulevičius, S. (2014). *Formation of Large Area Regular Nanostructures by Holographic Lithography Technique* // 2nd International Symposium on Optics & Its Applications (OPTICS–2014) September 2014, Yerevan and Ashtarak, Armenia (poster presentation)
12. **Virganavičius, D.**, Cadarso, V.J., Kirchner, R., Tamulevičius, T., Tamulevičius, S., Schift, H. (2015). *Patterning of Diamond Like Carbon Films Using Silicon Containing Thermoplastic Resist (SiPol) as Hard Mask* // 41st Micro and Nano Engineering Conference (MNE 2015), September 21–24, 2015. The Hague, the Netherlands (oral presentation).
13. **Virganavičius, D.**, Juodėnas, M., Tamulevičius, T., Grigaliūnas, V., Jahan, M., Henzie, J., Rubahn, H-G., Tamulevičius, S. (2016). *Template Assisted Ordering of Nanoparticle Arrays for Optical Applications* // EMRS Spring Meeting 2016, May 2–6, 2016. Lille, France (poster presentation).
14. **Virganavičius, D.**, Juodėnas, M., Tamulevičius, T., Tamulevičius, S. (2016). *Template Assisted Ordering of Nanoparticle Arrays* // The 18th International Conference-School on Advanced Materials and Technologies, August 27–31, 2016. Palanga, Lithuania (poster presentation).

LIST OF REFERENCES

1. FEYNMAN, R.P. (1960). There's Plenty of Room at the Bottom. In: *Engineering and Science, 1960, 23(5)*, 22–36.
2. WHATMORE, R.W. (2006). Nanotechnology – What Is It? Should We Be Worried? In: *Occupational Medicine, 2006, 56 (5)*, 295–299.
3. MOORE, G.E. (1965). Cramming More Components onto Integrated Circuits. In: *Electronics, 1965, 38(8)*, 114–117.
4. BALLER, S., DUTTA, S., LANVIN, B. (2016). *The Global Information Technology Report 2016*. World Economic Forum. ISBN 978-1-944835-03-3.
5. TANIGUCHI, J., TOKANO, Y., MIYAMOTO, I., KOMURO, M., HIROSHIMA, H. (2002). Diamond Nanoimprint Technology. In: *Nanotechnology, 2002, 13*, 592–596.
6. NÖHAMMER, B., HOSZOWSKA, J., FREUND, A.K., DAVID, C. (2003). Diamond Planar Refractive Lenses for Third- and Fourth-Generation X-Ray Sources. In: *Journal of Synchrotron Radiation, 2003, 10(2)*, 168–171.
7. FORSBERG, P., KARLSSON, M. (2013). High Aspect Ratio Optical Gratings in Diamond. In: *Diamond and Related* Materials, *2013, 34*, 19–24.
8. TAMULEVIČIUS, T., ŠEPERYS, R., ANDRULEVIČIUS, M., KOPUSTINSKAS, V., MEŠKINIS, Š., TAMULEVIČIUS, S., MIKALAYEVA, V., DAUGELAVIČIUS, R. (2012). Application of Holographic Sub-Wavelength Diffraction Gratings for Monitoring of Kinetics of Bioprocesses. In: *Applied Surface Science, 2012, 258 (23)*, 9292–9296.
9. HUSSAIN, S., ROY, R.K., PAL, A.K. (2006). Incorporation of Silver Nanoparticles in DLC Matrix and Surface Plasmon Resonance Effect. In: *Materials Chemistry and* Physics, *2006, 99*, 375–381.
10. MEŠKINIS, Š., GUDAITIS, R., KOPUSTINSKAS, V., TAMULEVIČIUS, S. (2008). Electrical and Piezoresistive Properties of Ion Beam Deposited DLC Films. In: *Applied Surface Science, 2008, 254*, 5252–5256.
11. NIE, X., JIANG, J.C., TUNG, L.D., SPINU, L., MELETIS, E.I. (2002). Multifunctional Co–C Nanocomposite Thin Films. In: *Thin Solid Films, 2002, 415*, 211–218.
12. JUKNIUS, T., RUŽAUSKAS, M., TAMULEVIČIUS, T., ŠIUGŽDINIENĖ, R., JUKNIENĖ, I., VASILIAUSKAS, A., JURKEVIČIŪTĖ, A., TAMULEVIČIUS, S. (2016). Antimicrobial Properties of Diamond-Like Carbon/Silver Nanocomposite Thin Films Deposited on Textiles: Towards Smart Bandages. In: *Materials, 2016, 9(5)*, 371.
13. WANG, Y.F., WANG, J., ZHANG, G.A., WANG, L.P., YAN, P.X. (2012). Microstructure and Tribology of TiC(Ag)/a-C:H Nanocomposite Coatings Deposited by Unbalanced Magnetron Sputtering. In: *Surface and Coatings Technology, 2012, 206*, 3299–3308.
14. SOARES, L.L., LIMA, C.R.A, CESCATO, L., ALVES, M.A.R., BRAGA, E.S. (1998). Recording of Relief Structures in Amorphous Hydrogenated

Carbon (a-C:H) Films for Infrared Diffractive Optics. In: *Journal of Modern Optics, 1998, 45(7)*, 1479–1486.
15. LEE, H.J., KWON, B.S., PARK, Y.R. *et al*. (2010). Inductively Coupled Plasma Etching of Chemical-Vapor-Deposited Amorphous Carbon in N_2/H_2/Ar Chemistries. In: *Journal of Korean Physical Society, 2010, 56*, 1441–1445.
16. KIM, J.K., CHO, S.I., KIM, N.G., JHON, M.S., MIN, K.S., KIM, C.K. *et al*. (2013). Study on the Etching Characteristics of Amorphous Carbon Layer in Oxygen Plasma with Carbonyl Sulfide. In: *Journal of Vacuum Science & Technology A: Vacuum, Surfaces, and Films, 2013, 31*, 021301.
17. PEARS, K.A. (2005). A New Etching Chemistry for Carbon Hard Mask Structures. In: *Microelectronic Engineering, 2005, 77*, 255–262.
18. PEARS, K.A., STOLZE, J. (2005). Carbon Etching with a High Density Plasma Etcher. In: *Microelectronic Engineering, 2005, 81*, 7–14.
19. KAKUCHI, M., HIKITA, M., TAMAMURA, T. (1986). Amorphous Carbon Films as Resist Masks with High Reactive Ion Etching Resistance for Nanometer Lithography. In: *Applied Physics Letters, 1986, 48*, 835–837.
20. RAMACHANDRAN, S., TAO, L., LEE, T.H., SANT, S., OVERZET, L.J., GOECKNER, M.J., KIM, M.J., LEE, G.S., HU, W. (2006). Deposition and Patterning of Diamond like Carbon as Antiwear Nanoimprint Templates. In: *Journal of Vacuum Science & Technology B, 2006, 24*, 2993–2997.
21. SAU, T.K., ROGACH, A.L. (2010). Nonspherical Noble Metal Nanoparticles: Colloid-Chemical Synthesis and Morphology Control. In: *Advanced Materials, 2010, 22(16)*, 1781–1804.
22. DONEGA, C.M. (2014). *Nanoparticles: Workhorses of Nanoscience*. Berlin, Heidelberg: Springer-Verlag. ISBN: 978-3-662-44822-9.
23. TANIGUCHI, N. (1974). On the Basic Concept of 'Nano-Technology'. In: *Proc. Intl. Conf. Prod. Eng. Tokyo, Part II, Japan Society of Precision Engineering, 1974*,18–23.
24. *ISO/TS 80004-2:2015 Nanotechnologies – Vocabulary – Part 2: Nano-Objects*. At: https://www.iso.org/obp/ui/#iso:std:iso:ts:80004:-2:ed-1:v1:en (accessed January 21, 2017).
25. VAJTAI, R. (2013). *Springer Handbook of Nanomaterials*. Berlin, Heidelberg: Springer-Verlag. ISBN 978-3-642-20594-1.
26. RODUNER, E. (2006). Size Matters: why Nanomaterials Are Different. In: *Chemical Society* Reviews, 2006, 35, 583–592.
27. HARUTA, M. (2014). Chance and Necessity: My Encounter with Gold Catalysts. In: *Angewandte Chemie International Edition, 2014, 53*, 52–56.
28. BURDA, C., CHEN, X., NARAYANAN, R., EL-SAYED, M.A. (2005). Chemistry and Properties of Nanocrystals of Different Shapes. In: *Chemical* Reviews, *2005, 105*, 1025–1102.
29. MURTY, B.S., SHANKAR, P., RAJ, B., RATH, B.B., MURDAY, J. (2013). *Textbook of Nanoscience and Nanotechnology*. Berlin, Heidelberg: Springer-Verlag. ISBN: 978-3-642-28029-0.

30. FREY, N.A., PENG, S., CHENG, K., SUN, S. (2009). Magnetic Nanoparticles: Synthesis, Functionalization, and Applications in Bioimaging and Magnetic Energy Storage. In: *Chemical Society Reviews, 2009, 38*, 2532–2542.
31. *http://www.sigmaaldrich.com/technical-documents/articles/materials-science/nanomaterials/ quantum-dots.html* (accessed November 25, 2016).
32. BIMBERG, D., POHL, U.W. (2011). Quantum Dots: Promises and Accomplishments. In: *Materials Today, 2011, 14*, 388–397.
33. SHIRASAKI, Y., SUPRAN, G.J., BAWENDI, M.G., BULOVIC, V. (2013). Emergence of Colloidal Quantum-Dot Light-Emitting Technologies. In: *Nature Photonics, 2013, 7*, 13–23.
34. DOANE, T.L., BURDA, C. (2012). The Unique Role of Nanoparticles in Nanomedicine: Imaging, Drug Delivery and Therapy. In: *Chemical Society Reviews, 2012, 41*, 2885–2911.
35. LUNT, R.R., OSEDACH, T.P., BROWN, P.R., ROWEHL, J.A., BULOVIC, V. (2011). Practical Roadmap and Limits to Nanostructured Photovoltaics. In: *Advanced Materials, 2011, 23*, 5712–5727.
36. HONG, Y, HUH, Y.M., YOON, D.S., YANG, J. (2012). Nanobiosensors Based on Localized Surface Plasmon Resonance for Biomarker Detection. In: *Journal of Nanomaterials, 2012*, 759830.
37. CAO, W., HUANG, T., XU, N.X-H., ELSAYED-ALI, H.E. (2011). Localized Surface Plasmon Resonance of Single Silver Nanoparticles Studied by Dark-Field Optical Microscopy and Spectroscopy. In: *Journal of Applied Physics, 2011, 109(3)*, 034310.
38. YANG, J., YOU, J., CHEN, C.C., HSU, W.C., TAN, H.R., ZHANG, X.W., HONG, Z., YANG, Y. (2011). Plasmonic Polymer Tandem Solar Cell. In: *ACS Nano, 2011, 5(8)*, 6210–6217.
39. TAN, J.M, RUAN, J., LEE, H.K., PHANGB, I.Y., LING, X.Y. (2014). A Large-Scale Superhydrophobic Surface-Enhanced Raman Scattering (SERS) Platform Fabricated via Capillary Force Lithography and Assembly of Ag Nanocubes for Ultratrace Molecular Sensing. In: *Physical Chemistry Chemical Physics, 2014, 16*, 26983.
40. WILLETS, K.A., VAN DUYNE, R.P. (2007). Localized Surface Plasmon Resonance Spectroscopy and Sensing. In: *Annual Review of Physical Chemistry, 2007, 58*, 267–297.
41. KELSALL, R.W., HAMLEY, I.W., GEOGHEGAN, M. (2005). *Nanoscale Science and Technology*. New Jersey: Wiley. ISBN: 978-0-470-85086-2.
42. KULKARNI, S.K. (2015). *Nanotechnology: Principles and Practices*. Heidelberg, New York, Dordrecht, London: Springer-Cham. ISBN 978-3-319-09170-9.
43. ZHOU, W. (2013). *Nanoimprint Lithography: An Enabling Process for Nanofabrication*. Heidelberg, New York, Dordrecht, London: Springer-Verlag. ISBN 978-3-642-34427-5.
44. STEPANOVA, M., DEW, S. (2012). *Nanofabrication Technique and Principles*. Vienna, New York: Springer. ISBN 978-3-7091-0423-1.

45. HOEFFLINGER, B. (2012). *Chips 2020: A Guide to the Future of Nanoelectronics*. Heidelberg: Springer-Verlag. ISBN 978-3-642-22399-0.
46. DONNELLY, V.M., KORNBLIT, A. (2013). Plasma etching: Yesterday, Today, and Tomorrow. In: *Journal of Vacuum Science & Technology A, 2013, 31(5),* 050825.
47. MEŠKINIS, Š., TAMULEVIČIUS, T., NIAURA, G., ŠLAPIKAS, K., VASILIAUSKAS, A., ULČINAS, O., TAMULEVIČIUS, S. (2016). Surface Enhanced Raman Scattering Effect in Diamond like Carbon Films Containing Ag Nanoparticles. In: *Journal of Nanoscience and Nanotechnology, 2016, 16(9), No. 9,* 10143–10151.
48. KUMAR, S.A., PETER, Y.A., NADEAU, J.L. (2008). Facile Biosynthesis, Separation and Conjugation of Gold Nanoparticles to Doxorubicin. In: *Nanotechnology, 2008, 19(49),* 495101.
49. HANRATH, T. (2012). Colloidal Nanocrystal Quantum Dot Assemblies as Artificial Solids. In: *Journal of Vacuum Science & Technology A, 2012, 30(3),* 030802.
50. DEMORTIERE, A., LAUNOIS, P., GOUBET, N., ALBOUY, P.A., PETIT, C. (2008). Shape-Controlled Platinum Nanocubes and Their Assembly into Two-Dimensional and Three-Dimensional Superlattices. In: *Journal of Physical Chemistry B, 2008, 112,* 14583.
51. GRZELCZAK, M., PEREZ-JUSTE, J., RODRIGUEZ-GONZALEZ, B., LIZ-MARZAN, L.M. (2006). Influence of Silver Ions on the Growth Mode of Platinum on Gold Nanorods. In: *Journal of Materials Chemistry, 2006, 16(40),* 3946–3951.
52. SEO, D., YOO, C.I, CHUNG, I.S., PARK S.M., RYU, S., SONG, H. (2008). Shape Adjustment between Multiply Twinned and Single-Crystalline Polyhedral Gold Nanocrystals: Decahedra, Icosahedra, and Truncated Tetrahedral. In: *Journal of Physical Chemistry C, 2008, 112(7),* 2469–2475.
53. KIM, F., CONNOR, S., SONG, H., KUYKENDALL, T., YANG, P. (2004). Platonic Gold Nanocrystals. In: *Angewandte Chemie International Edition, 2004, 43,* 3673.
54. CAO, C., PARK, S., SIM, S.J. (2008). Seedless Synthesis of Octahedral Gold Nanoparticles in Condensed Surfactant Phase. In: *Journal of Colloid and Interface Science, 2008, 322(1),* 152–157.
55. BURGIN, J., LIU, M., GUYOT-SIONNEST, P. (2008). Dielectric Sensing with Deposited Gold Bipyramids. In: *Journal of Physical Chemistry C, 2008, 112(49),* 19279–19282.
56. KUMAR, P.S., PASTORIZA-SANTOS, I., RODRIGUEZ-GONZALEZ, B., DE ABAJO, F.J.G, LIZ-MARZAN, L.M. (2008). High-Yield Synthesis and Optical Response of Gold Nanostars. In: *Nanotechnology, 2008, 19(1),* 015606.
57. MOCATTA, D., COHEN, G., SCHATTNER, J., MILLO, O., RABANI, E., BANIN, U. (2011). Heavily Doped Semiconductor Nanocrystal Quantum Dots. In: *Science, 2011, 332(6025),* 77–81.

58. BUONSANTI, R., MILLIRON, D.J. (2013). Chemistry of Doped Colloidal Nanocrystals. In: *Chemistry of Materials, 2013, 25*, 1305–1317.
59. TALAPIN, D.V., SHEVCHENKO, E.V., KORNOWSKI, A., GAPONIK, N., HAASE, M., ROGACH, A.L., WELLER, H. (2001). A New Approach to Crystallization of CdSe Nanoparticles into Ordered Three-Dimensional Superlattices. In: *Advanced Materials, 2001, 13(24)*, 1868–1871.
60. BOLES, M.A., ENGEL, M., TALAPIN, D.V. (2016). Self-Assembly of Colloidal Nanocrystals: From Intricate Structures to Functional Materials. In: *Chemical Reviews, 2016, 116*, 11220–11289.
61. CHOI, K.-S. (2008). Shape Control of Inorganic Materials via Electrodeposition. In: *Dalton Transactions, 2008, 40*, 5432–5438.
62. KÖPPL, S. (2011). *Seed-Mediated Synthesis of High Aspect Ratio Nanorods and Nanowires of Gold and Silver*. ETH ZURICH, DISS. ETH NO. 20021 2011.
63. SMITH, D.K., KORGEL, B.A. (2008). The Importance of the CTAB Surfactant on the Colloidal Seed-Mediated Synthesis of Gold Nanorods. In: *Langmuir, 2008, 24(3)*, 644–649.
64. BAKSHI, M.S., SHWETA, S.K., GURPREET, K., POONAM, B., GURINDER, K., MARK, C.B., FRED, P., NILS, O.P., Dependence of Crystal Growth of Gold Nanoparticles on the Capping Behavior of Surfactant at Ambient Conditions. In: *Crystal Growth and Design, 2008, 8(5)*, 1713–1719.
65. HURST, S.J., PAYNE, E.K., QIN, L., MIRKIN, C.A. (2006). Multisegmented One-Dimensional Nanorods Prepared by Hard-Template Synthetic Methods. In: *Angewandte Chemie International Edition, 2006, 45(17)*, 2672–2692.
66. MURRAY, C.B., KAGAN, C.R., BAWENDI, M.G. (1995). Self-Organization of CdSe Nanocrystallites into Three-Dimensional Quantum Dot Superlattices. In: *Science, 1995, 270 (5240)*, 1335–1338.
67. HENZIE, J., GRÜNWALD, M., WIDMER-COOPER, A., GEISSLER, P.L., YANG, P. (2011). Self-Assembly of Uniform Polyhedral Silver Nanocrystals into Densest Packings and Exotic Superlattices. In: *Nature Materials, 2011, 11(2)*, 131−137.
68. HALES, T.C., Historical Overview of the Kepler Conjecture. In: *Discrete and Computational Geometry, 2006, 36(1)*, 5−20.
69. TORQUATO, S., JIAO, Y. (2012). Organizing Principles for Dense Packings of Nonspherical Hard Particles: Not All Shapes Are Created Equal. *Physical Review E, 2012, 86 (1)*, 011102.
70. ZIHERL, P., KAMIEN, R.D. (2001). Maximizing Entropy by Minimizing Area: Towards a New Principle of Self-Organization. In: *Journal of Physical Chemistry B, 2001, 105(42)*, 10147–10158.
71. DE NIJS, B., DUSSI, S., SMALLENBURG, F., MEELDIJK, J.D., GROENENDIJK, D.J., FILION, L., IMHOF, A., VAN BLAADEREN, A., DIJKSTRA, M. (2014). Entropy-Driven Formation of Large Icosahedral

Colloidal Clusters by Spherical Confinement. In: *Nature Materials, 2014, 14(1),* 56–60.
72. HE, J., LIU, Y., BABU, T., WEI, Z., NIE, Z. (2012). Self-Assembly of Inorganic Nanoparticle Vesicles and Tubules Driven by Tethered Linear Block Copolymers. In: *Journal of the American Chemical Society, 2012, 134(28),* 11342–11345.
73. GRILL, A. (1999). Diamond-Like Carbon: State of the Art. In: *Diamond and Related Materials, 1999, 8,* 428–434.
74. ROBERTSON, J. (1986). Amorphous Carbon. In: *Advances in Physics, 1986, 35,* 317–374.
75. CASIRAGHI, C., ROBERTSON, J., FERRARI, A.C. (2007). Diamond-Like Carbon for Data and Beer Storage. In: *Materials Today, 2007, 10,* 44–53.
76. ROBERTSON, J. (2002). Diamond-Like Amorphous Carbon. In: *Materials Science and Engineering R, 2002, 37,* 129–281.
77. DIUDEA, M.V., NAGY, C.L. (2013). *Diamond and Related Nanostructures, Volume 6.* Netherlands: Springer, ISSN 1875-0745.
78. AISENBERG, S., CHABOT, R. (1972). Deposition of Carbon Films with Diamond Properties. In: *Carbon, 1972 vol.10,* 356.
79. FERRARI, A.C. (2004). Diamond-Like Carbon for Magnetic Storage Disks. In: *Surface and Coatings Technology, 2004, vol. 180–181,* 190–206.
80. GRILL, A. (1999). Electrical and Optical Properties of Diamond-Like Carbon. In: *Thin Solid Films, 1999, vol. 355–356,* 189–193.
81. YIN, Y., HANG, L., XU, J., MCKENZIE, D.R., BILEK, M.M.M. (2008). Surface Adsorption and Wetting Properties of Amorphous Diamond-Like Carbon Thin Films for Biomedical Applications. In: *Thin Solid Films, 2008, vol. 516,* 5157–5161
82. MORRISON, M.L., BUCHANAN, R.A., LIAW, P.K., BERRY, C.J., BRIGMON, R.L., RIESTER, L., ABERNATHY, H., JIN, C., NARAYAN, R.J. (2006). Electrochemical and Antimicrobial Properties of Diamond Like Carbon-Metal Composite Films. In: *Diamond and Related Materials, 2006, 15,* 138–146.
83. AZZI, M., AMIRAULT, P., PAQUETTE, M., KLEMBERG-SAPIEHA, J.E., MARTINU, L. (2010). Corrosion Performance and Mechanical Stability of 316L/DLC Coating System: Role of Interlayers. In: *Surface and Coatings Technology, 2010, 204,* 3986–3994.
84. DWIVEDI, N., KUMAR, S., MALIK, H., SREEKUMAR, C., DAYAL, S., RAUTHAN, C.M.S., PANWAR, O.S. (2012). Investigation of Properties of Cu Containing DLC Films Produced by PECVD Process. In: *Journal of Physics and Chemistry of Solids, 2012, 73,* 308–316.
85. MEŠKINIS, Š., PECKUS, D., VASILIAUSKAS, A., ČIEGIS, A., GUDAITIS, R., TAMULEVIČIUS, T., YAREMCHUK, I., TAMULEVIČIUS, S. (2017). Photovoltaic Properties and Ultrafast Plasmon Relaxation Dynamics of Diamond-Like Carbon Nanocomposite Films with

Embedded Ag Nanoparticles. In: *Nanoscale Research Letters, 2017, 12*, 288.
86. LUO, J.K., FU, Y.Q., WILLIAMS, J.A., SPEARING, S.M., MILNE, W.I. (2007). Diamond and Diamond-Like Carbon MEMS. In: *Journal of Micromechanics and Microengineering, 2007, 17*, 147–163.
87. JUKNIUS, T., TAMULEVIČIUS, T., GRAŽULEVIČIŪTĖ, I., KLIMIENĖ, I., MATUSEVIČIUS, A.P., TAMULEVIČIUS, S. (2014). In-Situ Measurements of Bacteria Resistance to Antimicrobial Agents Employing Leaky Mode Sub-Wavelength Diffraction Grating. In: *Sensors and Actuators B: Chemical, 2014, 204*, 799–806.
88. WANG, S.S., MAGNUSSON, R. (1993). Theory and Applications of Guided Mode Resonance Filters. In: *Applied Optics, 1993, 32*, 2606–2613.
89. WEI, X., WEISS, S.M. (2011). Guided Mode Biosensor Based on Grating Coupled Porous Silicon Waveguide. In: *Optics Express, 2011, 19(12)*, 11330–11339.
90. HERMANNSSON, P.G., KRISTENSEN, A., VANNAHME, C., SMITH, C. (2015). *Design and Use of Guided Mode Resonance Filters for Refractive Index Sensing*. DTU Nanotech.
91. UDDIN, M.J., MAGNUSSON, R. (2012). Efficient Guided-Mode-Resonant Tunable Color Filters. In: *IEEE Photonics Technology Letters, 2012, 24*, 1552–1554.
92. YANG, F., YEN, G., CUNNINGHAM, B.T. (2007). Voltage-Tuned Resonant Reflectance Optical Filter for Visible Wavelengths Fabricated by Nanoreplica Molding. In: *Applied Physics Letters, 2007, 90*, 261109.
93. HERMANNSSON, P.G, SØRENSEN, K.T., VANNAHME, C., SMITH, C.L.C., KLEIN, J.J., RUSSEW, M., GRÜTZNER, G., KRISTENSEN, A. (2015). All-Polymer Photonic Crystal Slab Sensor. In: *Optics Express, 2015, 23(13)*, 16529–16539.
94. FORSBERG, P., KARLSSON, M. (2013). Inclined Surfaces in Diamond: Broadband Antireflective Structures and Coupling Light Through Waveguides. In: *Optics Express, 2013, 21*, 2693–2700.
95. GE, C., LU, M., GEORGE, S., FLOOD, T.A., WAGNER, C., ZHENG, J., POKHRIYAL, A., EDEN, J.G., HERGENROTHER, P.J., CUNNINGHAM, B.T. (2013). External Cavity Laser Biosensor. In: *Lab on a Chip, 2013, 13*, 1247–1256.
96. SZEGHALMI, A., KLEY, E.B., KNEZ, M. (2010). Theoretical and Experimental Analysis of the Sensitivity of Guided Mode Resonance Sensors. In: *The Journal of Physical Chemistry C, 2010, 114(49)*, 21150–21157.
97. SALEEM, M.R., ALI, R., HONKANEN, S., TURUNEN, J. (2016). Bio-Molecular Sensors Based on Guided Mode Resonance Filters. 14th International Symposium on Advanced Materials IOP Publishing. In: *IOP Conf. Series: Materials Science and Engineering 2016, 146*, 012030.

98. FOLAND, S., SWEDLOVE, B., NGUYEN, H., LEE, J.B. (2012). One-Dimensional Nanograting-Based Guided-Mode Resonance Pressure Sensor. In: *Journal of Microelectromechanical Systems, 2012, 21(5),* 1117–1123.
99. TAMULEVIČIUS, T., GRAŽULEVIČIŪTĖ, I., URBONAS, D., GABALIS, M., PETRUŠKEVIČIUS, R., TAMULEVIČIUS, S. (2014). Numerical and Experimental Analysis of Optical Response of Sub-Wavelength Period Structure in Carbonaceous Film for Refractive Index Sensing. In: *Optics Express, 2014, 22,* 27462–27475.
100. YANG, J., REN, F., CHONG, X., FAN, D., CHAKRAVARTY, S., WANG, Z., CHEN, R.T., WANG, A.X., Guided-Mode Resonance Grating with Self-Assembled Silver Nanoparticles for Surface-Enhanced Raman Scattering Spectroscopy. In: *Photonics, 2014, 1,* 380–389.
101. JARAMILLO, J.M., MANSANO, R.D., ZAMBOM, L.S., MASSI, M., MACIEL, H.S. (2001). Wet Etching of Hydrogenated Amorphous Carbon Films. In: *Diamond and Related Materials, 2001, 10,* 976–979.
102. SASAKI, Y., TAKEDA, A., II, K., OHSHIO, S., AKASAKA, H., NAKANO, M., SAITOH, H. (2012). Evaluation of Etching on Amorphous Carbon Films in Nitric Acid. In: *Diamond and Related Materials, 2012, 24,* 104–106.
103. FAN, J.A., BAO, K., SUN, L., BAO, J., MANOHARAN, V.N., NORDLANDER, P., CAPASSO, F. (2012). Plasmonic Mode Engineering with Templated Self-Assembled Nanoclusters. In: *Nano Letters, 2012, 12,* 5318–5324.
104. MOTH-POULSEN, K., REY, A., BILLARDON, G., EMANUEL, L., STUHR-HANSEN, N., WOLF, H., BJØRNHOLM, T., STEMMER, A., RIEL, H. (2013). Deterministic Assembly of Linear Gold Nanorod Chains as a Platform for Nanoscale Applications. In: *Nanoscale, 2013, 5(18),* 8680–8688.
105. ZHANG, D., CUI, T. (2012). Tunable Mechanical Properties of Layer-by-Layer Self-Assembled Carbon Nanotube/ Polymer Nanocomposite Membranes for M/NEMS. In: *Sensors and Actuators A: Physical, 2012, 185,* 101–108.
106. FARCAU, C.N., SANGEETHA, N.M., MOREIRA, H., VIALLET, B., GRISOLIA, J., CIUCULESCU-PRADINES, D., RESSIER, L. (2011). High-Sensitivity Strain Gauge Based on a Single Wire of Gold Nanoparticles Fabricated by Stop-and-Go Convective Self-Assembly. In: *ACS Nano, 2011, 5(9),* 7137–7143.
107. GERSPACH, M.A., MOJARAD, N., PFOHL, T., EKINCI, Y. (2015). Glass-Based Geometry-Induced Electrostatic Trapping Devices for Improved Scattering Contrast Imaging of Nano-Objects. In: *Microelectronic Engineering, 2015, 145,* 43–48.
108. ASHKIN, A., DZIEDZIC, J.M., BJORKHOLM, J.E., CHU, S. (1986). Observation of a Single-Beam Gradient Force Optical Trap for Dielectric Particles. In: *Optics Letters, 1986, 11,* 288–290.

109. MALAQUIN, L., KRAUS, T., SCHMID, H., DELAMARCHE, E., WOLF, H. (2007). Controlled Particle Placement through Convective and Capillary Assembly. In: *Langmuir, 2007, 23*, 11513–11521.
110. PINEDO RIVERA, T., LECARME, O., HARTMANN, J., ROSSITTO, E., BERTON, K., PEYRADE, D. (2008). Assisted Convective-Capillary Force Assembly of Gold Colloids in a Microfluidic Cell: Plasmonic Properties of Deterministic Nanostructures. In: *Journal of Vacuum Science & Technology B, 2008, 26*, 2513–2519.
111. HENZIE, J., ANDREWS, S.C., YI, X., LI, Z., YANG, P. (2013). Oriented Assembly of Polyhedral Plasmonic Nanoparticle Clusters. In: *Proceedings of the National Academy of Sciences, 2013, 110(17)*, 6640–6645.
112. NI, S., LEEMANN, J., WOLF, H., ISA, L. (2015). Insights into Mechanisms of Capillary Assembly. In: *Faraday Discussions, 2015, 181*, 225–242.
113. FLAURAUD, V., MASTRANGELI, M., BERNASCONI, G.D., BUTET, J., ALEXANDER, D., SHAHRABI, E., MARTIN, O.J.F., BRUGGER, J. (2017). Nanoscale Topographical Control of Capillary Assembly of Nanoparticles. In: *Nature Nanotechnology, 2017, 12*, 73–80.
114. YUNKER, P.J., STILL, T., LOHR, M., YODH, A.G. (2011). Suppression of the Coffee-Ring Effect by Shape-Dependent Capillary Interactions. In: *Nature, 2011, 476*, 308–311.
115. BHUSHAN, B. (2010). *Springer Handbook of Nanotechnology*. Berlin, Heidelberg: Springer-Verlag. ISBN 978-3-642-02524-2
116. MAURY, P., ESCALANTE, M., REINHOUDT, D.N., HUSKENS, J. (2005). Directed Assembly of Nanoparticles onto Polymer Imprinted or Chemically Patterned Templates Fabricated by Nanoimprint Lithography. In: *Advanced Materials, 2005, 17(22)*, 2718–2723.
117. CORDEIRO, J., FUNFSCHILLING, F., LECARME, O., OSVALDO, G., PICARD, E., PEYRADE, D. (2015). On-Chip Polychromatic Visible Light Emitters Obtained by 3D Capillary Force Assembly. In: *Microelectronic Engineering, 2015, 110*, 414–417.
118. YIN, Y., LU, Y., GATES, B., XIA, Y. (2001). Template-Assisted Self-Assembly: A Practical Route to Complex Aggregates of Monodispersed Colloids with Well-Defined Sizes, Shapes, and Structures. In: *Journal of the American Chemical Society, 2001, 123*, 8718–8729.
119. KLEIN, M.J.K., KUEMIN, C., TAMULEVIČIUS, T., MANNING, M., WOLF, H. (2012). Note: A Microfluidic Chip Setup for Capillarity-Assisted Particle Assembly. In: *Review of Scientific Instruments, 2012, 83*, 086109.
120. NI, S., KLEIN, M.J.K., SPENCER, N.D., WOLF, H. (2015). Capillary Assembly of Cross-Gradient Particle Arrays Using a Microfluidic Chip. In: *Microelectronic Engineering, 2015, 141*, 12–16.
121. GREYBUSH, N.J., SABOKTAKIN, M., YE, X., DELLA GIOVAMPAOLA, C., OH, S.J., BERRY, N.E., ENGHETA, N., MURRAY, C.B, KAGAN, C.R. (2014). Plasmon-Enhanced Upconversion Luminescence in Single Nanophosphor-Nanorod Heterodimers Formed

through Template-Assisted Self-Assembly. In: *ACS Nano, 2014, 8*, 9482–9491.
122. CAYRON, H., BERTELOITE, B., VIEU, C., PAVEAU, V., CAU, J., CERF, A. (2015). Controlled Deposition and Multi-Layer Architecturing of Single Biomolecules Using Automated Directed Capillary Assembly and Nano-Contact Printing Processes. In: *Microelectronic Engineering, 2015, 135*, 1–6.
123. DAGUE, E., JAUVERT, E., LAPLATINE, L., VIALLET, B., THIBAULT, C., RESSIER, L. (2011). Assembly of Live Micro-Organisms on Microstructured PDMS Stamps by Convective/Capillary Deposition for AFM. In: *Nanotechnology, 2011, 22(39)*, 395102.
124. HU, H., LARSON, R. (2006). Marangoni Effect Reverses Coffee-Ring Depositions. In: *Journal of Physical Chemistry B, 2006, 110 (14)*, 7090–7094.
125. DEEGAN, R.D., BAKAJIN, O., DUPONT, T.F., HUBER, G., NAGEL, S.R., WITTEN, T.A. (1997). Capillary Flow as the Cause of Ring Stains from Dried Liquid Drops. In: *Nature, 1997, 389*, 827–829.
126. KIMOCK, F., FINKE, S., BROWN, D., THEAR, E. (1999). The Evolution of Ion-Beam Diamond-Like-Carbon Technology into Data Storage: Space Propulsion, Sunglasses, Slides and New Disks. In: *DataTech Magazine, 1999*, 69–77.
127. ZHURIN, V. (2012). *Industrial Ion Sources: Broad Beam Gridless Ion Source Technology*. Wiley-VCH Verlag, ISBN 9783527410293.
128. REDDY, K.V.S., SUBRAMANYAM, T., UTHANNA, S. (2007). Nitrogen Partial Pressure Influence on Physical Properties of DC Magnetron Sputtered Copper Nitride Films. In: *Optoelectronics and Advanced Materials. 2007, 1*, 31–35.
129. KELLY, P., ARNELL, R. (2000). Magnetron Sputtering: a Review of Recent Developments and Applications. In: *Vacuum, 2000, 56(3)*, 159–172.
130. ZHOU, W., WANG, Z.L., *Scanning Microscopy for Nanotechnology: Techniques and Applications*. New York: Springer-Verlag. ISBN 978-144-192-209-0.
131. LIDDLE, J.A., HARRIOTT, L.R., NOVEMBRE, A.E., WASKIEWICZ, W.K. (1999). *SCALPEL: A Projection Electron-Beam Approach to Sub-Optical Lithography*. Bell Laboratories, Lucent Technologies, Whitepaper. Available at: http://www.bell-labs.com/project/SCALPEL.
132. *MAPPER Lithography*. Delft. Available at: www.mapperlithography.com (accessed December 10, 2016).
133. SCHIFT, H. (2012). *NaPANIL Library of Processes*. NaPANIL Consortium. ISBN 978-3-00-038372-4.
134. SCHLEUNITZ, A., SCHIFT, H. (2010). Fabrication of 3-D Nanoimprint Stamps with Continuous Reliefs Using Dose-Modulated Electron Beam Lithography and Thermal Reflow. In: *Journal of Micromechanics and Microengineering, 2010, 20*, 095002.

135. SCHIFT, H. (2008). Nanoimprint Lithography: An Old Story in Modern Times? A Review. In: *Journal of Vacuum Science & Technology B, 2008, 26(2)*, 458–480.
136. CHOU, S.Y., KRAUSS, P.R., RENSTROM, P.J. (1995). Imprint of Sub-25 nm Vias and Trenches in Polymers. In: *Applied Physics Letters, 1995, 67*, 3114–3116.
137. HUA, T., ANDREW, G., CHOU, S.Y. (1998). Roller Nanoimprint Lithography. In: *Journal of Vacuum Science & Technology B, 1998, 16*, 3926–3939.
138. CHENG, X, GUO, L.J. (2004). A Combined-Nanoimprint-and-Photolithography Patterning Technique. In: *Microelectronic Engineering, 2004, 71*, 277–282.
139. BAO, L.R., CHENG, X., HUANG, X.D., GUO, L.J., PANG, S.W., YEE, A.F. (2002). Nanoimprinting over Topography and Multilayer Three-Dimensional Printing. In: *Journal of Vacuum Science & Technology B, 2002, 20*, 2881–2886.
140. AHN, S.H., KIM, J.S., GUO, L.J. (2007). Bilayer Metal Wire-Grid Polarizer Fabricated by Roll-to-Roll Nanoimprint Lithography on Flexible Plastic Substrate. In: *Journal of Vacuum Science & Technology B, 2007, 25*, 2388–2391.
141. CHOU, S., KEIMEL, C., GU, J. (2002). Ultrafast and Direct Imprint of Nanostructures in Silicon. In: *Nature, 2002, 417*, 835–837.
142. HUA, F., SUN, Y., GAUR, A., MEITL, M.A., BILHAUT, L., ROTKINA, L., WANG, J.F., GEIL, P., SHIM, M., ROGERS, J.A. (2004). Polymer Imprint Lithography with Molecular-Scale Resolution. In: *Nano Letters, 2004, 4*, 2467–2471.
143. PEREZ, N., TAVERA, T., RODRÍGUEZ, A., ELLMAN, M., AYERDI, I., OLAIZOLA, S.M. (2012). Fabrication of Sub-Micrometric Metallic Hollow-Core Structures by Laser Interference Lithography. In: *Applied Surface Science, 2012, 258(23)*, 9370–9373.
144. RODRIGUEZ, A., ECHEVERRIA, M., ELLMAN, M., PEREZ, N., VEREVKIN, Y.K., PENG, C.S., BERTHOUD, T., WANG, Z., AYERDIA, I., SAVALL, J., OLAIZOLA, S.M. (2009). Laser Interference Lithography for Nanoscale Structuring of Materials: from Laboratory to Industry. In: *Microelectronic Engineering, 2009, 86(4–6)*, 937–940.
145. BYUN, I., KIM, J. (2010). Cost-Effective Laser Interference Lithography Using a 405 Nm Alingan Semiconductor Laser. In: *Journal of Micromechanics and Microengineering, 2010, 20(5)*, 055024.
146. LEMME, M.C., MOORMANN, C., LERCH, H., MOLLER, M., VRATZOV, B., KURZ, H. (2004). Triple-Gate Metal–Oxide–Semiconductor Field Effect Transistors Fabricated with Interference Lithography. In: *Nanotechnology, 2004, 15*, 208–210.
147. CAMPBELL, M., SHARP, D.N., HARRISON, M.T., DENNING, R.G., TURBERFIELD, A.J. (2000). Fabrication of Photonic Crystals for the

Visible Spectrum by Holographic Lithography. In: *Nature, 2000, 404,* 53–56.
148. LEE, W., JI, R., ROSS, C.A., GOSELE, U., NIELSCH, K. (2006). Wafer-Scale Ni Imprint Stamps for Porous Alumina Membranes Based on Interference Lithography. In: *Small, 2006, 2(8–9),* 978–982.
149. MURILLO, R., VAN WOLFEREN, H.A., ABELMANN, L., LODDER, J.C. (2005). Fabrication of Patterned Magnetic Nanodots by Laser Interference Lithography. In: *Microelectronic Engineering, 2005, 78,* 260–265.
150. MAO, W., WATHUTHANTHRI, I., CHOI, C.H. (2011). Tunable Two-Mirror Interference Lithography System for Wafer–Scale Patterning. In: *Optics Letters, 2011, 36(16),* 3176–3178.
151. LANGNER, A., PAIVANRANTA, B., TERHALLE, B., EKINCI, Y. (2012). Fabrication of Quasiperiodic Nanostructures with EUV Interference Lithography. In: *Nanotechnology, 2012, 23,* 105303.
152. LU, C., LIPSON, R.H. (2010). Interference Lithography: a Powerful Tool for Fabricating Periodic Structures. In: *Laser & Photonics Reviews, 2010, 4(4),* 568–580.
153. *SPATIAL Filters*. Newport Corporation. Available at: https://www.newport.com/Spatial-Filters/144910/1033/content.aspx (accessed 30 June 2014).
154. ARRIOLA, A., RODRIGUEZ, A., PEREZ, N., TAVERA, T., WITHFORD, M.J., FUERBACH, A., OLAIZOLA, S.A. (2012). Fabrication of High Quality Sub-Micron Au Gratings over Large Areas with Pulsed Laser Interference Lithography for SPR Sensors. In: *Optical Materials Express, 2012, 2,* 1571–1579.
155. WATHUTHANTHRI, I., LIU, Y., DU, K., XU, W., CHOI, C. (2013). Simple Holographic Patterning for High-Aspect-Ratio Three-Dimensional Nanostructures with Large Coverage Area. In: *Advanced Functional Materials, 2013, 23(5),* 608–618.
156. GATZEN, H.H., SAILE, V., LEUTHOLD, J. (2015). *Micro and Nano Fabrication*. Berlin, Heidelberg: Springer-Verlag. ISBN 978-3-662-44394-1
157. REINBERG, A.R. (1973). *Radial Flow Reactor*. US patent 3,757,733 assigned to Texas Instruments.
158. OXFORD Instruments. *Reactive Ion Etching*. Available at: http://www.oxfordinstruments.com/products/etching-deposition-and-growth/plasma-etch-deposition/rie (accessed December 20, 2016)
159. https://www.crystec.com/trietche.htm (accessed December 20, 2016)
160. SAINIEMI, L. (2009). *Cryogenic Deep Reactive Ion Etching of Silicon Micro and Nanostructures*. Ph.D. Thesis, Helsinki University of Technology.
161. FORSBERG, P. (2013). *Diamond Microfabrication for Applications in Optics and Chemical Sensing*. Acta Universitatis Upsaliensis. Uppsala. ISBN 978-91-554-8587-0.

162. TAO, A., SINSERMSUKSAKUL, P., YANG, P. (2006). Polyhedral Silver Nanocrystals with Distinct Scattering Signatures. In: *Angewandte Chemie International Edition, 2006, 45(28)*, 4597–4601.
163. BUTT, H.J., CAPPELLA, B., KAPPL, M. (2005). Force Measurements with the Atomic Force Microscope: Technique, Interpretation and Applications. In: *Surface Science Reports, 2005, 59(1)*, 1–152.
164. TAMULEVIČIUS, S., ANDRULEVIČIUS, M. (2007). *Medžiagų analizės metodai*. Kaunas: Vitae Litera. ISBN: 978-9955-686-42-2.
165. NGO, P.D. (1999). Energy Dispersive Spectroscopy. In: *Failure Analysis of Integrated Circuits*. Heidelberg: Springer. 205–215. ISBN 978-1-4613-7231-8.
166. USER'S Manual – Abbe Refractometer Type G – Carl Zeiss Jena. Available at: http://www.microscopy-uk.org.uk/mag/artjun13/dg-refractometer.html (accessed September 18, 2017).
167. KUMAR, S.S.R.C. (2012). *Raman Spectroscopy for Nanomaterials Characterization*. Berlin, Heidelberg: Springer-Verlag. ISBN 978-3-642-20619-1.
168. VIRGANAVIČIUS, D., CADARSO, V.J., KIRCHNER, R., STANKEVIČIUS, L., TAMULEVIČIUS, T., TAMULEVIČIUS, S., SCHIFT, H. (2017). Patterning of Diamond like Carbon Films for Sensor Applications using Silicon Containing Thermoplastic Resist (SiPol) as a Hard Mask In: *Applied Surface Science.* 2016, 385, 145–152.
169. FLUCKIGER, D. (no year). *GSolver Version 5.2 User's Guide*. Available at: http://www.gsolver.com/UserManual.pdf (Accessed September 15, 2017).
170. FORSBERG, P., KARLSSON, M. (2013). High Aspect Ratio Optical Gratings in Diamond. *Diamond and Related Materials, 2013, 34*, 19–24.
171. MESSERSCHMIDT, M., SCHLEUNITZ, A., SPREU, C., WERNER, T., VOGLER, M., REUTHER, F. (2012). Thermal Nanoimprint Resist for the Fabrication of High-Aspect-Ratiopatterns. In: *Microelectronic Engineering, 2012, 98*, 107–111.
172. TAMULEVIČIENĖ, A., MEŠKINIS, S., KOPUSTINSKAS, V., TAMULEVIČIUS, S. (2011). Multilayer Amorphous Hydrogenated Carbon (a-C:H) and SiO(x) Doped a-C:H Films for Optical Applications. In: *Thin Solid Films, 2011, 519*, 4004–4007.
173. KWON, B.S., KIM, J.S, LEE, N.-E., SHON, J.W. (2010). Ultrahigh Selective Etching of SiO_2 Using an Amorphous Carbon Mask in Dual-Frequency Capacitively Coupled $C_4F_8/CH_2F_2/O_2$/Ar Plasmas. In: *Journal of Electrochemical Society, 2010, 157(3)*, D135–D141.
174. TAMULEVIČIUS, S., MEŠKINIS, Š., ŠLAPIKAS, K., VASILIAUSKAS, A., GUDAITIS, R., ANDRULEVIČIUS, M., TAMULEVIČIENĖ, A., NIAURA, G. (2013). Piezoresistive Properties of Amorphous Carbon Based Nanocomposite Thin Films Deposited by Plasma Assisted Methods. In: *Thin Solid Films, 2013, 538*, 78–84.

175. TAMULEVIČIUS, T., TAMULEVIČIENĖ, A., VIRGANAVIČIUS, D., VASILIAUSKAS, A., KOPUSTINSKAS, V., MEŠKINIS, Š., TAMULEVIČIUS, S. (2014). Structuring of DLC:Ag Nanocomposite Thin Films Employing Plasma Chemical Etching and Ion Sputtering. *Nuclear Instruments and Methods in Physics Research Section B*. 2014, 341, 1–6.
176. MEŠKINIS, Š., TAMULEVIČIENĖ, A. (2011). Structure, Properties and Applications of Diamond Like Nanocomposite (SiOx Containing DLC) Films: A Review. In: *Materials Science (Medžiagotyra), 2011, 17(4)*, 358–370.
177. YAN, X., XU, T., CHEN, G., YANG, S., LIU, H. (2004). Study of Structure, Tribological Properties and Growth Mechanism of DLC and Nitrogen-Doped DLC Films Deposited by Electrochemical Technique. In: *Applied Surface Science, 2004, 236(1)*, 328–335.
178. BOWKER, M. (2002). Surface Science: The Going Rate for Catalysis. In: *Nature Materials, 2002, 1*, 205–206.
179. ALEMAN, J., CHADWICK, A.V., HE, J., HESS, M., HORIE, K., JONES, R.G, KRATOCHVIL, P., MEISEL, I., MITA, I., MOAD, G., PENCZEK, S., STEPTO, R.F.T. (2007). Definitions of Terms Relating to the Structure and Processing of Sols, Gels, Networks, and Inorganic–Organic Hybrid Materials. In: *Pure and Applied Chemistry, 2007, 79*, 1801–1827.
180. THOGERSEN, A., MUNTINGH, G. (2013). Solar Induced Growth of Silver Nanocrystals. In: *Journal of Applied Physics, 2013, 113(14)*, 144301.
181. YAN, C.J., CHEN, Y.C., JIN, A.Z., WANG, M., KONG, X.D., ZHANG, X.F., JU, Y., HAN, L. (2011). Molecule Oxygen-Driven Shaping of Gold Islands under Thermal Annealing. In: *Applied Surface Science, 2011, 258*, 377–381.
182. PHOTOPOULOS, P., BOUKOS, N., PANAGOPOULOU, M., MEINTANIS, N., PANTISKOS, N., RAPTIS, Y., TSOUKALAS, D. (2011). Size Control of Ag Nanoparticles for SERS Sensing Applications. In: *Procedia Engineering, 2011, 25*, 280–283.
183. HEILMANN, A., QUINTEN, M., WERNER, J. (1998). Optical Response of Thin Plasma-Polymer Films with Non-Spherical Silver Nanoparticles. In: *The European Physical Journal B, 1998, 3(4)*, 455–461.
184. WORSCH, C., KRACKER, M., WISNIEWSKI, W., RUSSEL, C. (2012). Optical Properties of Self-Assembled Oriented Island Evolution of Ultra-Thin Gold Layers. In: *Thin Solid Films, 2012, 520(15)*, 4941–4946.
185. ZENG, H.D., QIU, J.R., JIANG, X.W., QU, S.L., ZHU, C.S., GAN, F.X. (2003). Influence of Femtosecond Laser Irradiation and Heat Treatment on Precipitation of Silver Nanoparticles in Glass. In: *Chinese Physics Letters, 2003, 20 (6)*, 932–934.
186. TANG, J., PHOTOPOULOS, P., TSEREPI, A., TSOUKALAS, D. (2011). Two-Dimensional Nanoparticle Self-Assembly Using Plasma-Induced Ostwald Ripening. In: *Nanotechnology, 2011, 22(23)*, 235306.

187. ANTAD, V., SIMONOT, L., BABONNEAU, D. (2013). Tuning the Surface Plasmon Resonance of Silver Nanoclusters by Oxygen Exposure and Low-Energy Plasma Annealing. In: *Nanotechnology, 2013, 24(4),* 045606.
188. SISKOVA, K., SAFAROVA, K., SEO, J.H, ZBORIL, R., MASHLAN, M. (2011). Non-Chemical Approach toward 2D Self-Assemblies of Ag Nanoparticles via Cold Plasma Treatment of Substrates. In: *Nanotechnology, 2011, 22(27),* 275601.
189. SIVARAMAN, S.K., SANTHANAM, V. (2012). Realization of Thermally Durable Close-Packed 2D Gold Nanoparticle Arrays Using Self-Assembly and Plasma Etching. In: *Nanotechnology, 2012, 23(25),* 255603.
190. THOGERSEN, A., BONSAK, J., FOSLI, C.H., MUNTINGH, G. (2011). Size Distributions of Chemically Synthesized Ag Nanocrystals. In: *Journal of Applied Physics, 2011, 110(4),* 044306.
191. TAN, M.L., ZHU, J.Q., HAN, J.C., NIU, L., LU, J., CHEN, W.S (2008). Relative Fraction of sp(3) Bonding in Boron Incorporated Amorphous Carbon Films Determined by X-Ray Photoelectron Spectroscopy. In: *Materials Research Bulletin, 2008, 43,* 1670–1678.
192. LIMPERT, E., STAHEL, A.W., ABBT, M. (2001). Log-Normal Distributions across the Sciences: Keys and Clues. In: *BioScience, 2001, 51(5),* 341–352.
193. ZIMNY, K., MASCARO, B., BRUNET, T., PONCELET, O., ARISTEGUI, C., LENG, J., SANDRE, O., MONDAIN-MONVAL, O. (2014). Design of a Fluorinated Magneto-Responsive Material with Tuneable Ultrasound Scattering Properties. In: *Journal of Materials Chemistry B, 2014, 2,* 1285–1297.
194. WANG, D., MARKUS, J., KIM, Y.J., WANG, C., JIMÉNEZ PÉREZ, Z.E., AHN, S.G., ACEITUNO, V.C., MATHIYALAGAN, R., YANG, D.C. (2016). Coalescence of Functional Gold and Monodisperse Silver Nanoparticles Mediated by Black Panax Ginseng Meyer Root Extract. In: *International Journal of Nanomedicine, 2016, 11,* 6621–6634.
195. LOPEZ-MIRANDA, A., LOPEZ-VALDIVIESO, A., VIRAMONTES-GAMBOA, G. (2012). Silver Nanoparticles Synthesis in Aqueous Solutions Using Sulfite as Reducing Agent and Sodium Dodecyl Sulfate as Stabilizer. In: *Journal of Nanoparticle Research, 2012, 14,* 1101.
196. CHAKRAVADHANULA, V., KUBEL, C., HRKAC, T., ZAPOROJTCHENKO, V., STRUNSKUS, T., FAUPEL, F., KIENLE, L. (2012). Surface Segregation in TiO_2-Based Nanocomposite Thin Films. In: *Nanotechnology, 2012, 23,* 495701.
197. SENDOVA, M., JIMENEZ, J.A. (2012). Plasmonic Coupling in Silver Nanocomposite Glasses. In: *The Journal of Physical Chemistry C, 2012, 116(33),* 17764–17772.
198. YAREMCHUK, I., TAMULEVIČIUS, T., FITIO, V., GRAŽULEVIČIŪTĖ, I., BOBITSKI, Y., TAMULEVIČIUS, S. (2013). Guide-Mode Resonance Characteristics of Periodic Structure on Base of Diamond-Like Carbon Film. In: *Optics Communications, 2013, 301,* 1–6.

199. YAREMCHUK, I., TAMULEVIČIENĖ, A., TAMULEVIČIUS, T., ŠLAPIKAS, K., BALEVIČIUS, Z., TAMULEVIČIUS, S. (2014). Modeling of the Plasmonic Properties of DLC-Ag Nanocomposite Films In: *Physica Status Solidi (a), 2014, 211,* 329–335.
200. KU, Y.-F., LI, H.-Y, HSIEH, W.-H., CHAU, L.-K., CHANG, G.-E. (2015). Enhanced Sensitivity in Injection-Molded Guided-Mode-Resonance Sensors via Low-Index Cavity Layers. In: *Optics Express, 2015, 23,* 14850–14859.
201. ABBAS, S., MOGHADDAS, J., SHAHABADI, M., MEMBER, S., MOHAMMAD-TAHERI, M. (2014). Surface Sensitivity Using Coupled Cross-Stacked Gratings. In: *IEEE Sensors Journal, 2014, 14,* 1216–1222.
202. WHITE, I.M., FAN, X. (2008). On the Performance Quantification of Resonant Refractive Index Sensors. In: *Optics Express, 2008, 16,* 1020–1028.
203. VIRGANAVIČIUS, D., ŠIMATONIS, L., JURKEVIČIŪTĖ, A., TAMULEVIČIUS, T., TAMULEVIČIUS, S. (2014). Formation of Sub-Wavelength Pitch Regular Structures Employing a Motorized Multiple Exposure Lloyd's Mirror Holographic Lithography Setup. In: *Proceedings SPIE 9170, Nanoengineering: Fabrication, Properties, Optics and Devices XI, 97101I.*
204. VIRGANAVIČIUS, D., JUODĖNAS, M., TAMULEVIČIUS, T., TAMULEVIČIUS, S., SCHIFT, H. (2017). Investigation of Transient Dynamics of Capillary Assisted Particle Assembly Yield. In: *Applied Surface Science.* 2017, 406, 136–143.

UDK 539.23-044.96(043.3)

SL344. 2017-11-28, 15 leidyb. apsk. l. Tiražas 12 egz. Užsakymas 369.
Išleido Kauno technologijos universitetas, K. Donelaičio g. 73, 44249 Kaunas
Spausdino leidyklos „Technologija" spaustuvė, Studentų g. 54, 51424 Kaunas